Université de Lille

Doctoral School **ED SMRE**

University Department **Laboratoire de Physique des Lasers, Atomes et Molécules (PhLAM)**

Thesis defended by **Guillaume Vanderhaegen**

Defended on **November 9, 2022**

In order to become Doctor from Université de Lille

Academic Field **Physics**

Speciality **Diluted media and fundamental optics**

Intensity and phase measurements along optical fibers to reveal the complex nonlinear dynamic of Fermi-Pasta-Ulam-Tsingou recurrences

Thesis supervised by	Arnaud Mussot	Supervisor
	Pascal Szriftgiser	Co-Supervisor

Committee members

Referees	Bertrand Kibler	Senior Researcher at Université Bourgogne-Franche-Comté	
	Victor Torres-Company	Professor at Chalmers University of Technology	
Examiners	Nicolas Cherroret	Junior Researcher at Université Paris Sorbonne	
	Claire Michel	Associate Professor at Université Côte d'Azur	
	Alexandre Kudlinski	Professor at Université de Lille	Committee President
	Matteo Conforti	Junior Researcher at Université de Lille	
Supervisors	Arnaud Mussot	Professor at Université de Lille	
	Pascal Szriftgiser	Senior Researcher at Université de Lille	

Université de Lille

Doctoral School **ED SMRE**

University Department **Laboratoire de Physique des Lasers, Atomes et Molécules (PhLAM)**

Thesis defended by **Guillaume Vanderhaegen**

Defended on **November 9, 2022**

In order to become Doctor from Université de Lille

Academic Field **Physics**

Speciality **Diluted media and fundamental optics**

Intensity and phase measurements along optical fibers to reveal the complex nonlinear dynamic of Fermi-Pasta-Ulam-Tsingou recurrences

Thesis supervised by	Arnaud Mussot	Supervisor
	Pascal Szriftgiser	Co-Supervisor

Committee members

Referees	Bertrand Kibler	Senior Researcher at Université Bourgogne-Franche-Comté	
	Victor Torres-Company	Professor at Chalmers University of Technology	
Examiners	Nicolas Cherroret	Junior Researcher at Université Paris Sorbonne	
	Claire Michel	Associate Professor at Université Côte d'Azur	
	Alexandre Kudlinski	Professor at Université de Lille	Committee President
	Matteo Conforti	Junior Researcher at Université de Lille	
Supervisors	Arnaud Mussot	Professor at Université de Lille	
	Pascal Szriftgiser	Senior Researcher at Université de Lille	

Université de Lille

École doctorale **ED SMRE**

Unité de recherche **Laboratoire de Physique des Lasers, Atomes et Molécules (PhLAM)**

Thèse présentée par **Guillaume Vanderhaegen**

Soutenue le **9 novembre 2022**

En vue de l'obtention du grade de docteur de l'Université de Lille

Discipline **Physique**

Spécialité **Milieux dilués et optique fondamentale**

Mesures en intensité et en phase le long de fibres optiques pour révéler la dynamique non linéaire complexe des récurrences de Fermi-Pasta-Ulam-Tsingou

Thèse dirigée par Arnaud Mussot directeur
Pascal Szriftgiser co-directeur

Composition du jury

Rapporteurs	Bertrand Kibler	directeur de recherche à l'Université Bourgogne-Franche-Comté	
	Victor Torres-Company	professeur au Chalmers University of Technology	
Examinateurs	Nicolas Cherroret	chargé de recherche à l'Université Paris Sorbonne	
	Claire Michel	MCF à l'Université Côte d'Azur	
	Alexandre Kudlinski	professeur à l'Université de Lille	président du jury
	Matteo Conforti	chargé de recherche à l'Université de Lille	
Directeurs de thèse	Arnaud Mussot	professeur à l'Université de Lille	
	Pascal Szriftgiser	directeur de recherche à l'Université de Lille	

This thesis has been prepared at the following research units.

Laboratoire de Physique des Lasers, Atomes et Molécules (PhLAM)
Bâtiment P5
Campus Cité Scientifique
2 Avenue Jean Perrin
59655 Villeneuve d'Ascq Cedex
France

Institut de Recherche en Composants logiciels et matériels pour l'Information et la Communication Avancée (IRCICA)
Parc scientifique de la Haute Borne
50 avenue Halley
59658 Villeneuve d'Ascq Cedex
France

Pour ma famille,

À toi Constance,

"There are two possible outcomes. If the result confirms the hypothesis, then you've made a measurement. If the result is contrary to the hypothesis, then you've made a discovery."

Enrico Fermi

Intensity and phase measurements along optical fibers to reveal the complex nonlinear dynamic of Fermi-Pasta-Ulam-Tsingou recurrences

Abstract

This thesis work deals with experimental investigations of the Fermi-Pasta-Ulam-Tsingou (FPUT) recurrences in optical fibers, which are induced by the nonlinear regime of modulation instability (MI). MI is one of the most universal phenomenon in nonlinear physics where a weak perturbation of a strong plane wave is exponentially amplified during its propagation in a nonlinear and dispersive medium. In case of a periodic modulation of the plane wave, a complex but coherent dynamics between the initial and the newly generated waves takes place. It reaches the saturation, then follows a decay stage and finally returns to its initial state. In this thesis, we were able to deeply characterize this dynamics by distributed measurements in amplitude and phase of the main spectral components thanks to a multi-heterodyne time domain reflectometry setup. By actively compensating for the fiber attenuation, we first managed to mimic an integrable system and to observe FPUT dynamics over long distances. It both allowed to confirm theoretical predictions of the NLSE and record up to 5 consecutive recurrences, as a seminal result for the following studies. Then, we investigated modulation instability and FPUT in non-integrable systems: from the noise instability as a detrimental effect leading to the recurrences break-up and an irreversibly thermalized system, from a weak damping or forcing contribution leading to separatrix crossings and multiple symmetry breakings of the process, and from the fiber shaping with an oscillating dispersion profile leading to MI even in the normal regime.

Keywords: nonlinear fiber optics, modulation instability, fermi-pasta-ulam-tsingou recurrences, breathers, nonlinear schrödinger equation

Mesures en intensité et en phase le long de fibres optiques pour révéler la dynamique non linéaire complexe des récurrences de Fermi-Pasta-Ulam-Tsingou

Résumé

Ces travaux de thèse portent sur des études expérimentales des récurrences de Fermi-Pasta-Ulam-Tsingou (FPUT) dans des fibres optiques, qui apparaissent en régime non linéaire de l'instabilité modulationnelle (IM). L'IM est l'un des phénomènes les plus universels en physique non linéaire dans lequel une faible perturbation d'une onde plane intense est amplifiée exponentiellement lors de sa propagation dans un milieu non linéaire et dispersif. Dans le cas d'une modulation périodique de l'onde plane, une dynamique complexe mais cohérente s'opère entre les ondes initialement excitées et celles nouvellement générées. Elle atteint ensuite la saturation, puis suit un cycle de décroissance et revient finalement à son état initial. Dans cette thèse, nous avons pu caractériser cette dynamique en profondeur par des mesures distribuées en amplitude et en phase des principales composantes spectrales grâce à un montage de détections hétérodynes couplé à un réflectomètre temporel. En compensant activement l'atténuation de la fibre, nous avons d'abord réussi à simuler un système intégrable et à observer la dynamique des récurrences de FPUT sur de longues distances. Cela nous a permis d'une part de confirmer des prédictions théoriques de l'équation de Schrödinger non linéaire et d'autre part d'enregistrer jusqu'à 5 récurrences d'affilée, comme résultat préliminaire aux études suivantes. Ensuite, nous avons examiné l'IM et les récurrences de FPUT dans des systèmes non intégrables : par l'instabilité du bruit en tant qu'effet nuisible conduisant à la brisure des récurrences et à un système irréversiblement thermalisé, par une faible atténuation ou amplification entrainant des passages de séparatrice et de multiples brisures de symétrie du processus, et par la mise en forme oscillante du profil de dispersion de la fibre amenant à de l'IM même en régime normal.

Mots clés : optique non linéaire fibrée, instabilité modulationelle, récurrences de fermi-pasta-ulam-tsingou, ondes de respiration, équation de schrödinger non linéaire

Laboratoire de Physique des Lasers, Atomes et Molécules (PhLAM)
Bâtiment P5 – Campus Cité Scientifique – 2 Avenue Jean Perrin – 59655 Villeneuve d'Ascq Cedex – France

Remerciements

Je souhaite tout d'abord remercier Marc Douay, ancien directeur, et Cristian Focsa, directeur du laboratoire PhLAM de l'Université de Lille et ancien directeur des études doctorales, pour m'avoir permis d'effectuer cette thèse. Je tiens également à remercier Céline Toubin, directrice des études doctorales, pour avoir veillé à son bon déroulement. Je remercie aussi les sources de financement de cette thèse, à savoir le label I-SITE du Programme d'Investissements d'Avenir et l'ED SMRE, sans lesquels elle n'aurait pas été possible.

Mes remerciements vont ensuite aux membres du jury pour avoir accepté d'évaluer mon travail, tout d'abord les rapporteurs, Bertrand Kibler, directeur de recherche CNRS à l'Université Bourgogne-Franche-Comté, Victor Torres-Company, professeur à l'Université de Technologie de Chalmers, ainsi que les examinateurs/trices, Nicolas Cherroret, chargé de recherche CNRS à l'Université Paris Sorbonne, et Claire Michel, maître de conférences à l'Université Côte d'Azur.

Bien évidemment cette thèse n'aurait pas été possible sans l'encadrement de mes directeurs de thèse, Arnaud Mussot et Pascal Szriftgiser, que je tiens à remercier chaleureusement. Vous m'avez permis de travailler dans des conditions optimales, que ce soit d'un point de vue matériel mais également humain. Pascal, je te remercie pour ta patience et ta pédagogie dans la transmission de tes connaissances, qu'elles soient techniques ou théoriques, mais toujours au service de l'expérience (même si j'ai encore beaucoup à apprendre de ton optimisation des codes Matlab). Arnaud, je te remercie pour ta patience et tes encouragements tout au long de ma thèse. Alors que tout avait commencé par un stage d'école d'ingénieurs en 2018, on a marqué quelques buts depuis. Je reste concentré, il en reste encore un à marquer le 9 novembre (le but en or ?). Merci de m'avoir partagé ta passion pour la recherche et pour les pots du vendredi. J'en profite pour remercier Matteo Conforti, que je venais embêter régulièrement pour des questions théoriques en tout genre, parfois futiles, et Alexandre Kudlinski, avec qui j'ai eu la chance de partager ma passion du basket lors de mon premier match NBA (let's go Warriors!).

J'adresse mes remerciements à l'ensemble des chercheurs à avec qui j'ai eu la chance de collaborer et d'échanger dans le cadre de certaines publications. Je pense à Stefano Trillo, dont la pédagogie et la rigueur m'ont beaucoup appris, ou encore Nail Akhmediev

et Amin Chabchoub. Je souhaite également remercier Gilbert Martinelli, qui m'a donné la possibilité d'enseigner à l'IMT Lille-Douai et pour nos discussions furtives en sortie de TD.

Mes remerciements vont ensuite à l'ensemble des mes collègues de l'équipe Photonique du PhLAM, avec qui j'ai grandement apprécié échanger que ce soit dans le cadre du travail ou au détour d'un pot, d'un barbecue. Plus particulièrement, je souhaite remercier mes acolytes de bureau, Dylan, camarade de la première heure (bon courage pour ta soutenance), Stefano, qui va rapidement devenir meilleur que moi aux mots croisés alors que le français n'est que sa troisième langue, ou encore Zoheir, dernier arrivé de la tribu 104. Je souhaite remercier aussi les autres compères du Techno Flamme. Gaëlle, la maman du groupe, Thomas, le volleyeur de bonne humeur, Vincent, le magicien des mots (malgré lui), Eve-Line, l'astrologue déchue, Sarah, la top chef des plats vegan, Jean, la force tranquille et Aymeric, le champion de France des mots croisés. Merci pour la bonne ambiance et la vie que vous apportez sur notre lieu de travail. J'ai adoré les repas partagés le midi, les échanges, les débats, les rires, les blagues, les restos, les bars et j'en passe. J'ai également une pensée pour les anciens doctorants du groupe non linéaire, Corentin et Florent, qui m'ont ouvert la voie, et les post-doctorants, actuels et anciens, Etienne, mon camarade d'escalade, JB et Andrea.

Bien-sûr, je remercie l'ensemble de mes amis, de Lille ou d'ailleurs, que j'ai connu en classe préparatoire, en école d'ingénieurs ou ailleurs. Merci d'avoir été là, et même si nous sommes, pour beaucoup, éloignés géographiquement, je ne vous oublie pas.

Viens maintenant le moment de remercier l'ensemble de ma famille pour leur bienveillance malgré ma fâcheuse tendance à ramener ma science. Maman, pour m'avoir toujours soutenu dans ce que je faisais, Thibault, pour avoir été, malgré toi, un modèle de grand frère, aîné oblige, Paul, pour avoir été le cadet mais surtout mon acolyte de bêtises depuis le plus jeune âge, et enfin Salomé, pour avoir surmonté la tâche non-aisée de grandir en tant que benjamine de trois grands frères. Je suis très fier des personnes que vous êtes devenues aujourd'hui et d'être votre frère. J'ai également une pensée pour Lucie et votre petit Tintin, qui n'est d'ailleurs plus si petit.

"Last but not least", comme on aime à le dire outre-Manche, ma pensée ira à toi, Constance, pour avoir le courage de me supporter mais aussi de m'aimer jour après jour, depuis plus de 3 ans. J'ai hâte de mettre à jour le chiffre de cette dernière ligne d'un "+1" tous les ans, à tes côtés. Je t'aime.

Table of contents

Abstract **xiii**

Remerciements **xv**

Table of contents **xvii**

Acronyms **xxi**

Introduction **1**

1 Propagation of light in optical fibers **5**
1.1 Linear effects 6
1.1.1 Attenuation 6
1.1.2 Dispersion 7
1.2 Nonlinear effects 8
1.2.1 Kerr effect 8
1.2.2 Raman scattering 10
1.3 Propagation equation: the nonlinear Schrödinger equation 11
1.3.1 Development of the NLSE 11
1.3.2 NLSE numerical solving 12

2 From modulation instability to the Fermi-Pasta-Ulam-Tsingou recurrences **15**
2.1 The Fermi-Pasta-Ulam-Tsingou paradox 16
2.2 Modulation instability theory 18
2.2.1 Linear stability analysis 19
2.2.2 Noise-driven modulation growth 21
2.3 Nonlinear MI-induced Fermi-Pasta-Ulam-Tsingou recurrences 23
2.3.1 Numerical example of FPUT dynamics 23
2.3.2 Solitons on finite background 26
2.3.3 The truncated three-wave mixing model 28
Chapter conclusions 33

3 Experimental setup **35**
3.1 Overview of the experimental setup . . . 36
3.2 Nonlinear pulse shaping . . . 36
3.3 Distributed measurements . . . 39
3.4 Phase measurements by heterodyning . . . 41
3.4.1 Heterodyne detection principle . . . 41
3.4.2 Heterodyning implementation in our setup . . . 42
3.5 Post-processing techniques . . . 44
3.6 Raman loss compensation . . . 46
3.7 Stability of the setup . . . 50
Chapter conclusions . . . 51

4 Demonstration of FPUT-predicting NLSE analytical solutions **53**
4.1 The first-order doubly periodic solutions . . . 54
4.1.1 Solutions description . . . 54
4.1.2 Three waves input approximation . . . 56
4.1.3 Experimental results . . . 58
B-type solutions . . . 58
A-type solutions . . . 59
4.2 Gain outside the conventional MI band . . . 61
4.2.1 Analytical feature . . . 61
4.2.2 Experimental demonstration . . . 63
Initial conditions . . . 63
Results . . . 63
Chapter conclusions . . . 67

5 FPUT recurrences in long fibers and route to the thermalization **69**
5.1 Multiple FPUT recurrences recording . . . 70
5.1.1 Initial conditions . . . 70
5.1.2 Results for phase-shifted recurrences . . . 72
5.1.3 Results for in-phase recurrences . . . 74
5.2 FPUT recurrences thermalization in optical fibers . . . 75
5.2.1 Noise-driven thermalization dynamic . . . 76
5.2.2 Experimental results . . . 79
Chapter conclusions . . . 83

6 Separatrix crossing and multiple symmetry breakings in weakly damped and forced FPUT recurrences **85**
6.1 Theory of separatrix crossing from damping and forcing . . . 86
6.1.1 Numerical approach . . . 86
6.1.2 Description from the three-waves model . . . 89
6.1.3 Description from the finite-gap theory . . . 90
6.2 Experimental demonstration . . . 91
6.2.1 Tuning of the loss and gain . . . 91

6.2.2 Weak damping results 93
6.2.3 Weak forcing results 97
Chapter conclusions 100

7 Modulation instability and FPUT recurrences in topographic fibers 101
7.1 Modulation instability in dispersion oscillating fibers 102
7.1.1 Introduction to fiber diameter modulation in nonlinear optics . . 102
7.1.2 Linear regime of MI in DOFs 103
7.1.3 Nonlinear regime of MI in DOFs 106
Concept of frequency gain shift in DOF 107
FPUT recurrences in DOF 108
7.2 Demonstration of the nonlinear MI stage in DOFs 109
7.2.1 Fiber characterization 109
7.2.2 Experimental setup for the gain shift observation 110
7.2.3 Experimental results of gain shift 112
7.2.4 Towards FPUT observation in DOFs 113
Chapter conclusions 115

Conclusion 117

A Analytical development of the first-order doubly periodic solutions of the NLSE 121
B-type solutions 121
A-type solutions 122

B Short pulse Raman amplification 125

C Raman pulse shaping, towards a perfect loss compensation 129

Bibliography 133

Author's bibliography 147

Acronyms

3WM Three-wave mixing

AB Akhmediev breather

AOM Acousto-optic modulator

AWG Arbitrary wave generator

CW Continuous wave

DC Direct current

DFB Distributed feedback

DOF Dispersion oscillating fiber

DSF Dispersion shifted fiber

EDFA Erbium-doped fiber amplifier

FFT Fast Fourier transform

FPUT Fermi-Pasta-Ulam-Tsingou

FWHM Full width at half maximum

FWM Four-wave mixing

GNLSE Generalized nonlinear Schrödinger equation

GVD Group velocity dispersion

HOTDR Heterodyne optical time-domain reflectometry

IM Intensity modulator

KM Kuznetsov-Ma

MI Modulation instability

MUX Multiplexer

NLSE Nonlinear Schrödinger equation

NZDSF Non-zero dispersion shifted fiber

OSA Optical spectrum analyzer

OTDR Optical time-domain reflectometry

PBS Polarization beam splitter

PC Polarization controller

PCF Photonic crystal fiber

PD Photodiode

PID Proportional-integral-derivative

PM Phase modulator

PS Peregrine soliton

PSD Power spectral density

QPM Quasi-phase matching

RF Radio frequency

SBS Stimulated Brillouin scattering

SMF Single mode fiber

SNR Signal to noise ratio

SOA Semiconductor optical amplifier

SPM Self-phase modulation

SSE Shannon spectral entropy

SSF Split-step Fourier

SVEA Slowly varying envelope

ULL Ultra-low loss

XPM Cross-phase modulation

ZDW Zero-dispersion wavelength

Introduction

The first observation of a laser radiation by T. Maiman in 1960 [1] paved the way of a broad and still growing range of applications. While lasers are commonly used for industrial (machining), military (guidance, armament) or medical (surgery, diagnosis) purposes, it also brought a great interest for the scientific research. As this highly coherent, focused and intense light is able to modify the optical properties during its propagation in the medium, it especially gave an incredible rise to nonlinear optics. Even if lasers are not indispensable to observe nonlinear effects (experimental works related to the Raman scattering discovery in 1928 [2] for example), this new source of light opened up new perspectives in the field and emulated the whole community. Indeed, barely a year later in 1961, lasers were used by P.A. Franken *et al.* to demonstrate the second harmonic generation in a quartz crystal [3] and by W. Kaiser *et al.* to reveal the two-photon absorption in CaF_2:Eu^{2+} [4]. Still in bulk media, other observations were made in the following years: the Kerr effect [5], the stimulated Brillouin scattering [6], the four-wave mixing [7].

A revolution concerning light propagation and transmission came along with the next decade through the development of optical fibers. In 1970, Corning company developed the first ever "low-loss" silica fiber [8] (an attenuation around 20 dB/km at 632.8 nm), following the seminal work of K.C. Kao about the benefit of glass material for optical transmissions [9]. In addition to its success in broadband optical telecommunications, this breakthrough also turned out to be a practical platform for nonlinear investigations. Indeed, by combining both the focused beam from the laser and the confinement in a fiber core over long distances, the optical fibers are a fantastic test bed to observe nonlinear effects as the light-matter interaction is highly enhanced. Then, many nonlinear phenomena were observed in fiber optics, especially by Stolen *et al.*, with the stimulated Brillouin scattering [10], the stimulated Raman scattering [11], the optical Kerr effect [12], the four-wave mixing [13] and the self-phase modulation [14]. It was followed in 1986 by the first demonstration of modulation instability (MI) in fibers

by K. Tai *et al.* [15], discovered two decades before in optics by Bespavlov and Talanov [16] and in hydrodynamics by Benjamin and Feir [17].

MI is a phenomenon of amplification of a weak perturbation from a plane wave in a nonlinear dispersive medium. These conditions being applicable to many other fields of physics, it is quite ubiquitous [18] and also observed in Bose-Einstein condensates [19] or in plasmas [20]. MI phenomenon have especially been investigated for its key role in the rogue waves formation [21–26] and the supercontinuum generation [27]. If the perturbation amplitude remains weak compared to the plane wave one, it is considered as the linear stage of MI and the perturbation keeps growing exponentially. However, when the perturbation amplitude becomes similar to the plane wave one, it is considered as the nonlinear MI stage and the system exhibits much more complex dynamics. For an initially weak periodic perturbation with an oscillation frequency unstable with respect to MI, the system follows successive nonlinear stages of periodic cycles of growth and decay of the modulation. It exhibits a periodic fashion, that can be characterized as a repeated breathers dynamics. The evolution in the Fourier domain reveals repeated broadenings and narrowings into a triangular shaped frequency comb [28] due to four-wave mixing. This process is commonly referred as Fermi-Pasta-Ulam-Tsingou recurrences, from the analogy with the historical discovery [29].

The experiment of Fermi, Pasta, Ulam and Tsingou, performed in Los Alamos in 1953 with the MANIAC computer, is undoubtedly a pioneer of numerical simulations which also gave birth to nonlinear physics. They aimed to study the energy transfers between the eigenmodes of a nonlinearly coupled oscillators chain. While they were expecting the thermalization of the system i.e. the equidistribution of the energy over all the modes, the system exhibited a paradoxical reversible behavior, returning to its initial state after a certain time. To borrow N. Akhmediev's expression in [30], the energy flows evolve like the letters in a palindrome as the system progresses with a certain dynamic until the saturation and follows then the exact same but reversed dynamic before recovering its initial state. Even if the paradox was no longer one from the following decade especially with the works of N. Zabusky and M. Kruskal in [31], it has remained intriguing and has created a great interest in many fields of nonlinear physics.

While it was done in 1977 in water waves [32] and in 1978 in electric transmission lines [33], the first observation of a FPUT recurrence in an optical fiber was only realized in 2001 by G. Van Simaeys *et al.* [34], 15 years after its analytical prediction from the nonlinear Schrödinger equation (NLSE) [35]. Thanks to the improvement of fiber attenuation and by ingeniously limiting the detrimental effect of SBS thanks to a quasi-CW regime, they were able to record a full growth and decay cycle. This aroused the curiosity

of the community [30] and paved the way of further experimental investigations. More generally, it emulated researches on the formation of breathers waves [36–38], these solutions of the NLSE representing a convincing formalism for rogue waves representation. Even if an optical fiber turns out to be an ideal platform to study this phenomenon due to the stability and control it offers, the question of distributed measurements remains. Contrary to hydrodynamics where direct observation and measurement of the FPUT recurrences are possible [32, 39], it requires measurement methods to indirectly retrieve the dynamics along the fiber propagation distance as in [34, 37, 40, 41]. Especially in 2018, A. Mussot *et al.* exposed an original non-invasive experimental setup which allowed them to record two full FPUT recurrences and to reveal their intrinsic broken symmetry nature [42]. By coupling an optical time domain reflectometer with a multi-heterodyning detection, they were able to recover both the power and phase evolutions of the main frequency components along the all propagation length. Thanks to an active loss compensation with a Raman amplifier, they also got free from the detrimental effect of fiber attenuation. The work presented in this thesis found its ground through this paper [42] and the corresponding PhD works of C. Naveau [43–45]. The main goal of this thesis was to improve this setup and to implement experimental methods to investigate in depth modulation instability and Fermi-Pasta-Ulam-Tsingou recurrences processes in longer optical fiber spans. First, we managed to observe long distance dynamics and confirm seminal theoretical predictions thanks to Raman amplified quasi-transparent fibers. Then, we also investigated and characterized the dynamics of modulation instability and FPUT recurrences in non-integrable (noise, damping and forcing) and non-uniform systems (dispersion oscillating fibers).

The manuscript is organized in seven chapters, as follows. The Chapter 1 is dedicated to the presentation of the generalities and notions associated to the propagation of light in optical fibers. It includes both the linear and the nonlinear phenomena, the NLSE that models the propagation and the corresponding numerical integration method. In Chapter 2, we describe the phenomena of modulation instability and FPUT recurrences in optical fibers. First, the subject is contextualized by introducing the original FPUT paradox. Then, we present the MI theory which accounts for the linear stage and the FPUT recurrences occurring in the nonlinear stage. The latter is generally described with two analytical approaches (breather theory, three-wave mixing model) which are discussed in the chapter. The Chapter 3 provides a stage by stage complete description of the experimental setup. We present respectively the nonlinear pulse shaping, the OTDR, the heterodyning technique, the post-processings and the active loss compensation scheme. In Chapter 4, we report the first observation of the doubly-periodic solutions

of the NLSE as we were able to mimic an integrable system in long fiber spans thanks to the Raman compensation [46]. In addition to predict the FPUT dynamics, these solutions present an instability regime beyond the conventional MI gain band which is also investigated [47]. Then, we study in Chapter 5 the multiple FPUT recurrences and the transition towards the thermalization in long fiber spans. We first report the observation of a high number (≥ 4) of FPUT recurrences [48] as a prerequisite to investigate then the noise-driven thermalization of the process [49]. The Chapter 6 provides a better understanding of the FPUT dynamics under realistic conditions, in a non-integrable system weakly damped or forced. It induces separatrix crossings and reveals multiple symmetry breakings which are predicted by theoretical models detailed in this chapter. Then, we experimentally demonstrate these predictions in the weakly both damped or forced regimes through a fine tuning of the loss/gain coefficient [50]. While the previous chapters deal with FPUT in uniform i.e. dispersion constant fibers, the Chapter 7 is dedicated to the study of MI and FPUT recurrences in dispersion oscillating fibers (DOFs). We present the theory explaining the presence of MI even in the normal dispersion regime in DOFs, the weakly nonlinear MI stage inducing a gain frequency shift of the parametric process and the highly nonlinear stage at the origin of FPUT recurrences. Then, we detail our experimental investigations and the results obtained so far concerning this new instability band induced by a weakly nonlinear MI regime. The manuscript also contains three appendices which detail: the formula for the first-order doubly periodic solutions of the NLSE, as derived in [51, 52], in Appendix A; an experimental study of the backward Raman amplification of short pulses and the associated saturation effects [53] in Appendix B; the experimental results of the Raman pump time shaping schemes to obtain transparent optical fibers in Appendix C.

Chapter 1

Propagation of light in optical fibers

Outline of the current chapter

1.1 Linear effects **6**
1.1.1 Attenuation 6
1.1.2 Dispersion 7
1.2 Nonlinear effects **8**
1.2.1 Kerr effect 8
1.2.2 Raman scattering 10
1.3 Propagation equation: the nonlinear Schrödinger equation **11**
1.3.1 Development of the NLSE 11
1.3.2 NLSE numerical solving 12

This chapter aims to present generalities and proper notions on the propagation of light in an optical fiber. It doesn't aim to be an exhaustive list of the phenomena occurring in fibers but to introduce the theoretical tools to take into account the main effects encountered through the subject of this thesis. The first two sections will focus on the linear and nonlinear effects and the corresponding physical quantities associated to the propagation of light in an optical fiber. In the last section, we will introduce the propagation model, which includes the presented effects, and the numerical method to solve this model.

1.1 Linear effects

1.1.1 Attenuation

During its propagation into an optical fiber, a signal suffers from linear losses of different natures depending on its wavelength. Considering the simple case of a standard single mode fiber, the signal intensity is mainly attenuated by two phenomena. The first one is the Rayleigh scattering, which is due to small inhomogeneities of the fused silica density, which result in local fluctuations of the refractive index. A tiny fraction of the propagating light is then scattered isotropically during its travel in the medium. The back-reflected part of the Rayleigh scattered light can be useful, in particular for optical time domain reflectometry (OTDR) to monitor the losses along a fiber span [54], which will be developed more in detail later in this manuscript. The second one is the silica infrared absorption, due to the photons-phonons interactions. Impurities appearing inside the glass during the fiber manufacturing can also be a reason for linear losses. In practice, it is especially the case with the OH ions, which is caused by a humid environment. Its absorption peak is at 2.73 μm, so at the origin of the high loss peak around 1.4 μm (the harmonic absorption wavelength), as seen in Fig. 1.1. The pollution

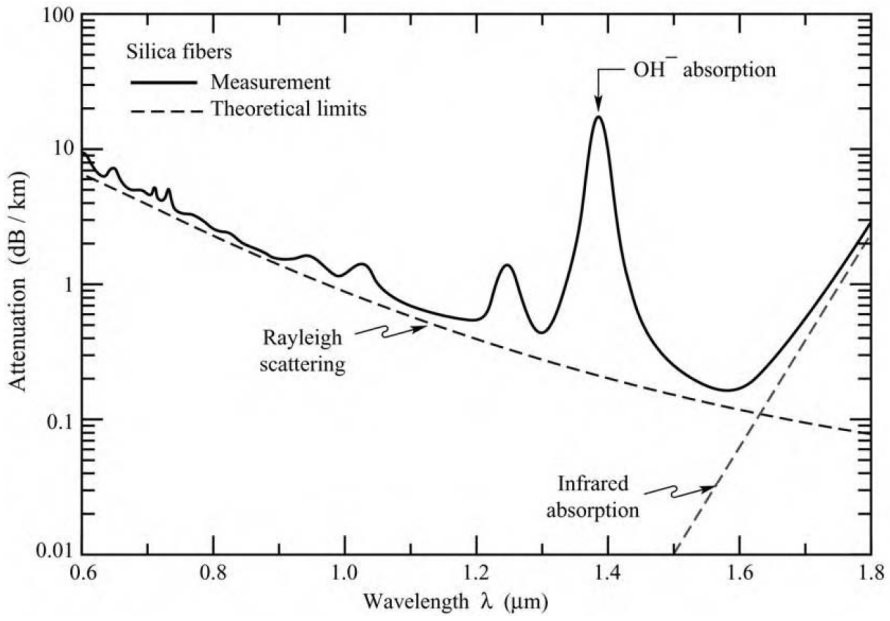

Figure 1.1: Spectral attenuation curve of silica, from [55].

from OH ions is then highly controlled during the fiber manufacturing process to reduce this attenuation peak, and even make it disappear [56]. The linear attenuation of an

optical fiber is generally noted α. A signal output power P_{out} from a fiber of length L is linked to the input power P_{in} through the Beer-Lambert law:

$$P_{out} = P_{in}e^{-\alpha L} \tag{1.1}$$

where α is expressed in m^{-1}. Commonly the attenuation is expressed in dB/km, defined with the relation:

$$\alpha_{dB} = -\frac{10}{L} log\left(\frac{P_{out}}{P_{in}}\right) = 4343\alpha \tag{1.2}$$

The minimum attenuation reached with a standard silica single mode fiber is α_{dB}(@1560 nm) = 0.1419 dB/km [57].

1.1.2 Dispersion

In a dielectric medium, such as silica, the refractive index n usually depends on the angular frequency ω. The chromatic dispersion is simply described by assuming the slowly varying envelope approximation (SVEA), considering a spectral with of the signal $\Delta\omega$ negligible compared to the carrier frequency ω_0. In the work presented here, this is always verified as the spectral broadening doesn't exceed 1 THz, while the carrier frequency is the telecom one (193 THz). This assumption allows to expand the propagation constant $\beta(\omega)$ in Taylor series around ω_0:

$$\beta(\omega) = n(\omega)\frac{\omega}{c} = \beta_0 + \beta_1(\omega-\omega_0) + \frac{\beta_2}{2}(\omega-\omega_0)^2 + \frac{\beta_3}{6}(\omega-\omega_0)^3 + ... = \sum_{k=0}^{\infty}\frac{\beta_k}{k!}(\omega-\omega_0)^k \tag{1.3}$$

where

$$\beta_k = \left(\frac{d^k\beta}{d\omega^k}\right)_{\omega=\omega_0} \tag{1.4}$$

β_1 is the inverse of the group velocity (in s/m), which is the velocity of the wave envelope, while β_2 is the group velocity dispersion (GVD, in s^2/m). As the refractive index depends on the wavelength, the GVD accounts for the velocity difference between the constitutive waves of a non-monochromatic signal. Two types of GVD regimes can be distinguished according to the sign of β_2. If $\beta_2 > 0$, the regime is called normal dispersion and the short wavelengths propagate slower than the long wavelengths. If $\beta_2 < 0$, the regime is called anomalous dispersion and the short wavelengths travel slower than the long wavelengths. Then, such a feature leads to the sliding of the frequencies and so the temporal broadening of the optical pulse into a chirp [58]. The Figure 1.2. (a) shows the effect of the group velocity dispersion on the temporal profile of a Gaussian pulse. The

pulse has initially a width of $\tau_0 = 10$ ps and a peak power $P_0 = 0.5$ W. The propagation

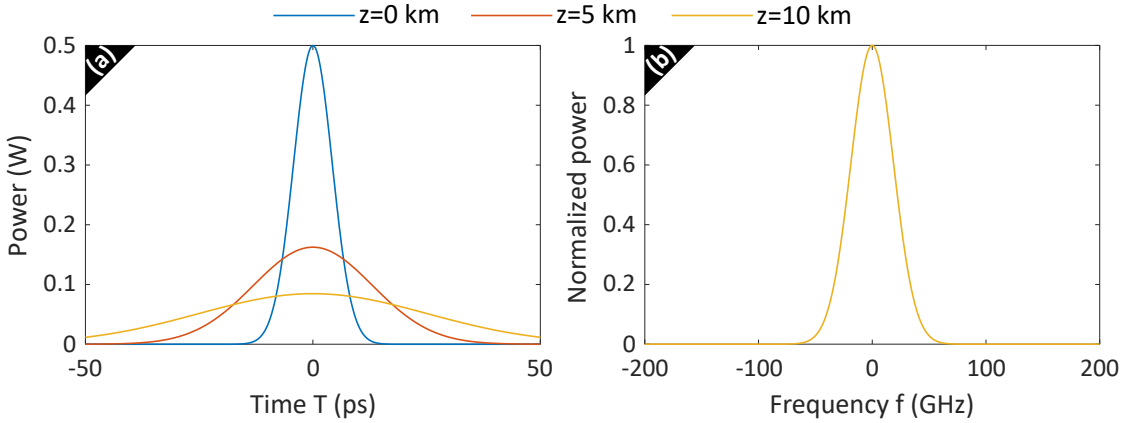

Figure 1.2: (a) Time evolution and (b) frequency power spectrum of a gaussian pulse propagating in a dispersive fiber with $\beta_2 = -21$ ps^2/km. The pulse has initially $\tau_0 = 10$ ps at FWHM, $\Delta f_0 = 44$ GHz at FWHM and $P_0 = 0.5$ at peak power. In blue $z = 0$, orange $z = 5$ km and yellow $z = 10$ km.

over 10 km of fiber leads the pulse to be temporally broadened by a factor 5, while the peak power is reduced by 5 (expected by energy conservation). We also notice through Fig. 1.2.(b) that, as for all the linear effects, the GVD doesn't have any impact on the wavelength intensity distribution. The dispersion of an optical fiber depends both on the dielectric material dispersion and the waveguide dispersion, that can be calculated or measured with standard techniques [59, 60]. The transition wavelength from the normal and anomalous regimes ($\beta_2 = 0$) is called zero dispersion wavelength (ZDW). Close to this transition and if $\Delta\omega$ is large enough, the higher order dispersion terms (β_3, β_4) are not negligible anymore, as the chromatic dispersion vanishes to zero, and have to be taken into account. This ZDW can be engineered to reach particular dispersion regimes and values at desired wavelengths. It can be achieved with photonic crystal fibers (PCF) [61, 62] or, from standard single-mode fibers, called dispersion shifted fibers (DSF) [63, 64].

1.2 Nonlinear effects

1.2.1 Kerr effect

The propagation of light in an optical fiber generates a polarization through the interaction of the electromagnetic field with the dielectric medium. The polarizability vector **P**

is related to the electromagnetic field with the susceptibility tensor χ as:

$$\mathbf{P} = \mathbf{P_L} + \mathbf{P_{NL}} = \epsilon_0 \left(\chi^{(1)} \cdot \mathbf{E} + \chi^{(2)} : \mathbf{EE} + \chi^{(3)} \vdots \mathbf{EEE} + ... \right) \tag{1.5}$$

where ϵ_0 is the vacuum dielectric permittivity and $\chi^{(k)}$ is the k^{th} order susceptibility. The propagation into the medium is considered linear if the field is weak and only the first-order susceptibility $\chi^{(1)}$ is considered. This term accounts for the chromatic dispersion, presented in the previous part, through the expression of the refractive index $n(\omega) = \sqrt{1 + Re(\chi^{(1)}(\omega))}$. If the field is intense, the polarizability isn't reduced to the first term and the nonlinear contribution $\mathbf{P_{NL}}$ has to be included. Due to the centro-symmetry of the silica, the second-order susceptibility $\chi^{(2)}$ can fairly be neglected in standard optical fibers as it vanishes. The main nonlinear contribution is then the third-order susceptibility $\chi^{(3)}$ and the higher-orders ($\chi^{(4)}$, $\chi^{(5)}$, etc.) are usually neglected. The third-order susceptibility is mainly responsible for the intensity dependence of the refractive index, commonly known as the Kerr effect, according:

$$n(\omega) = n_0(\omega) + n_2 I \tag{1.6}$$

where $I = |E|^2$ is the light intensity and n_2 the nonlinear refractive index (in $W^{-1}m^2$). The latter is proportional to the third-order susceptibility and can be developed as $n_2 = \frac{3Re(\chi^{(3)})}{8n_0}$. The nonlinear response of an optical fiber is generally quantified via the nonlinear coefficient γ defined as:

$$\gamma = \frac{n_2 \omega_0}{c A_{eff}} \tag{1.7}$$

where A_{eff} is the effective area of the field transverse mode. In standard monomode fibers, n_2 is around 2.6×10^{-20} [58] and A_{eff} at the telecommunications wavelength 1550 nm is 80 μm^2, leading to a nonlinear coefficient γ of 1.3 W^{-1}km^{-1}. For some specific applications which require high spectral broadenings (supercontinuum, frequency combs, etc.), optical fibers can be engineered to reach nonlinear coefficient of one or two orders of magnitude higher than silica [58], or even more using highly nonlinear materials such as chalcogenide glass [65] or silicon [61, 62, 66]. The Kerr effect is the source of several phenomena such as self-phase modulation (SPM), cross-phase modulation (XPM), or four-wave mixing (FWM). The SPM, as the name indicates, corresponds to the modulation of the pulse by itself during its propagation. Indeed, the pulse modifies locally the refraction index, which has an immediate impact on the wave phase. Figure

1.3 shows the influence of SPM on a Gaussian pulse, initially identical to the one in Fig. 1.2. New frequencies are created and the spectrum is progressively broadened and

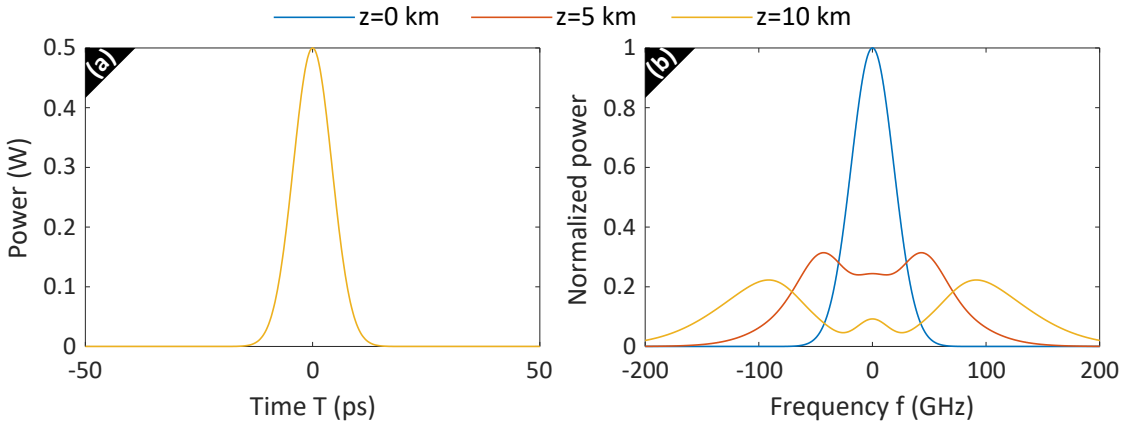

Figure 1.3: (a) Time evolution and (b) frequency power spectrum of a gaussian pulse propagating in a nonlinear fiber with $\gamma = 1.3$ W^{-1}km^{-1}. The pulse has initially $\tau_0 = 10$ ps at FWHM, $\Delta f_0 = 44$ GHz at FWHM, $P_0 = 0.5$ W at peak power. In blue $z = 0$, orange $z = 5$ km and yellow $z = 10$ km.

distorted from the Gaussian shape [58, 67–69], while it doesn't have any influence on the pulse temporal distribution. It is possible to define a length beyond which the Kerr effect becomes significant, the nonlinear length L_{NL} defined as:

$$L_{NL} = \frac{1}{\gamma P_0} \tag{1.8}$$

1.2.2 Raman scattering

The Raman scattering, taking its name from C. V. Raman who first discovered the process in 1928 [2], is an inelastic scattering process due to the nonlinear response from an electromagnetic wave excitation into vibrations of the matter lattice (i.e. optical phonons). This response is not instantaneous as it appears with a delay between 50 and 100 fs in silica. In optical fibers, such a process was observed in 1972 by Stolen *et al.* [11]. The process can be described using the energy diagram in Fig. 1.4.(a). A pump photon ω_P first excites a virtual state and then decays to a vibrational state of the silica medium by emitting a signal photon ω_S. To complete the transition, the remaining energy is released through the vibration of the silica lattice, in an optical phonon ω_R. To respect the energy conservation, the signal photon frequency is $\omega_S = \omega_P - \omega_R$, lower than the initial pump frequency. Due to the amorphous structure of the silica, the vibrational

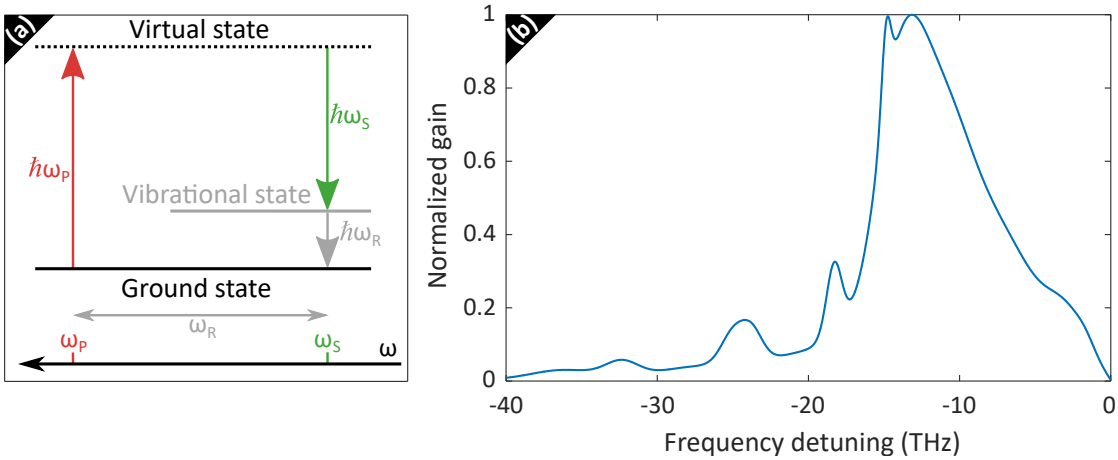

Figure 1.4: (a) Raman scattering energy diagram and (b) normalized silica Raman gain curve.

states are not discrete but continuous and the optical phonons frequency ω_R ranges then from 0 to 40 THz in standard fibers. It means that the Raman gain extends up to 40 THz from the pump frequency, as seen on the Raman gain curve in Fig. 1.4.(b) [70–72]. The converted energy into phonons is maximum for a 13.2 THz frequency shift from the pump wave, leading to a maximum of gain. Also, for very short pulses (below the picosecond) i.e. for wide spectra (beyond hundreds of GHz), the low frequencies are amplified at the expense of the high frequencies, due to the antisymmetry of the Raman gain curve. It leads to slight shift of the spectrum to the low frequencies. The stimulated Raman scattering is commonly used in telecommunications systems for a distributed amplification, to compensate the linear attenuation [73]. To amplify a 1550 nm signal, a 1450 nm laser pump (to benefit from the maximum gain 13.2 THz away) is injected in the fiber as a "photons reserve". As this technique is implemented in our experiments to get almost transparent optical fiber spans, it will be explained in detail later on in the manuscript.

1.3 Propagation equation: the nonlinear Schrödinger equation

1.3.1 Development of the NLSE

While the Maxwell equations were too complex to simulate numerically the propagation of light in an optical fiber in a decent amount of time, hypothesis have been done to reduce it to a simpler equation. Still considering the SVEA, a propagation equation of

the field envelope E in a single mode optical fiber is derived: the generalized nonlinear Schrödinger equation (GNLSE). This equation was established in [74, 75] in the time domain, but also in the spectral domain in [76]. It is widely used to describe the dynamics of nonlinear optical fiber systems and is written as:

$$\frac{\partial E(z,T)}{\partial z} = \sum_{k=2}^{\infty} \frac{i^{k+1}}{k!}\beta_k \frac{\partial^k E(z,T)}{\partial T^k} + i\gamma E(z,T)\int R(T')\left|E(z,T-T')\right|^2 dT' - \frac{\alpha}{2}E(z,T) \quad (1.9)$$

where $T = t - \beta_1 z$ is the time in a reference frame travelling at the group velocity of the carrier frequency ω_0, β_k are the k^{th} order chromatic dispersion terms (in $s^k m^{-1}$), γ is the nonlinear coefficient (in $W^{-1}m^{-1}$) and α is the linear attenuation (in m^{-1}). $R(T)$ is the nonlinear response of the medium which takes into account both the instantaneous Kerr effect and the delayed Raman scattering. Few approximations can be done to reduce Eq. 1.9 to the essential for our specific configuration [58]. As we work with a standard single-mode fiber and a 1550 nm signal i.e. far to the ZDW, the chromatic dispersion can be reduced to the 2^{nd} order β_2 and the higher orders neglected. The Raman scattering is also neglected as $\Delta\omega$ is much smaller than the characteristic frequencies of the optical phonons generated. The losses being compensated through a Raman amplification scheme to get a quasi-integrable system, the attenuation term is neglected. From Eq. 1.9 and these approximations, we get the nonlinear Schrödinger equation (NLSE) as follows:

$$\frac{\partial E(z,T)}{\partial z} = -i\frac{\beta_2}{2}\frac{\partial^2 E(z,T)}{\partial T^2} + i\gamma|E(z,T)|^2 E(z,T) \quad (1.10)$$

where γ is the nonlinear coefficient, β_2 is the GVD of the central frequency. For all results presented in this manuscript, we checked that these assumptions were relevant.

1.3.2 NLSE numerical solving

In the major cases, the NLSE cannot be solved analytically and a numerical solving method is required. The one which is commonly used is the split-step Fourier (SSF) method [58], where the propagation distance is discretized into short dz steps and which allows to separate the calculations of the linear and the nonlinear effects at each step. To do so, the contributions in the NLSE are splitted in two operators:

$$\frac{\partial E(z,T)}{\partial z} = \left(\hat{L} + \hat{N}\right)E(z,T) \quad (1.11)$$

with $\hat{L}$ and $\hat{N}$ the linear and the nonlinear operators respectively, defined as:

$$\hat{L} = -i\frac{\beta 2}{2}\frac{\partial^2}{\partial T^2} \text{ and } \hat{N} = i\gamma|E(z,T)|^2 \tag{1.12}$$

In the case where we cannot neglect the linear attenuation, the term $-\frac{\alpha}{2}$ is added to the linear operator. Other effects like Raman scattering and higher-orders dispersion can obviously be taken into account in these operators but it will not be necessary here. The SSF method, allowing to obtain from the field $E(z,T)$ the result of the propagation on a dz distance $E(z+dz,T)$, is simply developed here and schematized in Fig.1.5. On a

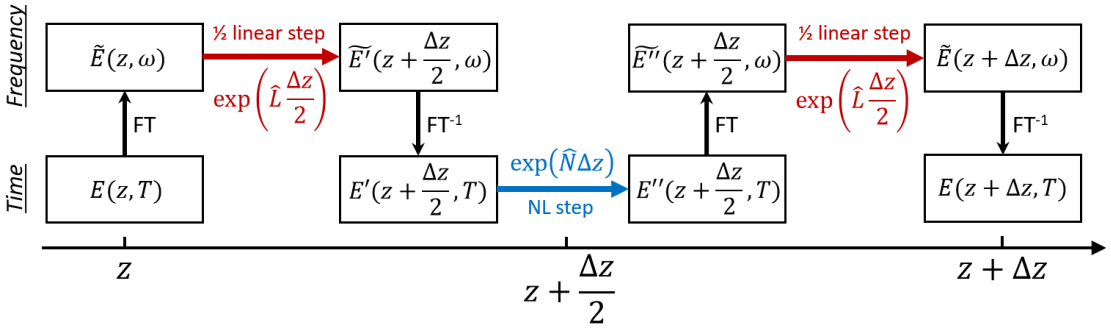

Figure 1.5: Diagram of the split-step Fourier method with the linear effect half-stepped.

first half-step $\frac{dz}{2}$, we handle the linear contributions, i.e. $\hat{N}=0$, in the Fourier domain, where an exact solution can easily be found. Then, we solve the nonlinear contributions, i.e. $\hat{L}=0$, on a step dz in the real domain, where an exact solution can also easily be found. Finally, we handle the linear contributions once again, on a second half-step $\frac{dz}{2}$, to complete the solving on a full dz step. To retrieve the evolution of the field along the all fiber length L, this stage is repeated from $z=0$ to $z=L$, with the necessary number of dz steps. To obtain precise numerical simulations, this step dz has to be chosen wisely, so that the error on the linear and nonlinear effects independence approximation is small enough. In practice, we implement dz smaller than the nonlinear and dispersion lengths by a few orders of magnitude.

Chapter 2

From modulation instability to the Fermi-Pasta-Ulam-Tsingou recurrences

Outline of the current chapter

2.1 The Fermi-Pasta-Ulam-Tsingou paradox **16**

2.2 Modulation instability theory **18**

2.2.1 Linear stability analysis 19

2.2.2 Noise-driven modulation growth 21

2.3 Nonlinear MI-induced Fermi-Pasta-Ulam-Tsingou recurrences **23**

2.3.1 Numerical example of FPUT dynamics 23

2.3.2 Solitons on finite background 26

2.3.3 The truncated three-wave mixing model 28

Chapter conclusions **33**

This chapter aims to introduce, describe and explain the complex dynamics at the origin of the Fermi-Pasta-Ulam-Tsingou (FPUT) recurrences formation in optical fibers. In a first section, we will introduce the numerical experiment that the FPUT paradox originates from as well as the solution found in term of solitons. In the following section, the modulation instability (MI) theory is reminded, allowing to describe the linear

stage of the process. Finally, the required tools to describe the nonlinear stage of MI, responsible for the FPUT recurrences, are presented in the last section.

2.1 The Fermi-Pasta-Ulam-Tsingou paradox

The Fermi-Pasta-Ulam-Tsingou problem, referring to the scientists who discovered it in 1953, is the first numerical simulation in nonlinear dynamics ever and even a pioneer in nonlinear physics. The original idea was to study solid-state physics thermalization i.e. how a crystal system evolves towards a thermal equilibrium. For this purpose, they used one of the first computer ever, MANIAC (Mathematical Analyzer, Numerical Integrator And Computer), initially designed to perform accurate calculations on nuclear reactions, based in Los Alamos. To put into perspective the performances of this computer, it was able to perform 10,000 operations per second [77] whereas the actual iPhone 13 with the Apple A15 chip is capable of 15.8 trillions operations per second [78]. While their working time was dedicated to the scientific and technological progress of their country in this beginning of Cold War, Fermi, Pasta, Ulam and Tsingou were working on their free time (and also the free time of the computer) to benefit from these new incredible computing capacities and to progress on their own researches. Working on energy modes transfers and thermal equilibrium, they modeled a chain, fixed at both extremities, of 16, 32 or 64 masses (see Fig. 2.1). The masses were linked to each other with springs classically following the Hooke law, adding a weak nonlinear interaction. The coupling equations and the nonlinear interaction models are detailed in [29]. While a linear coupling between the masses would make the energy remains in the initially excited vibration mode, the nonlinear interaction introduces a coupling between the modes at the origin of energy transfers. With an initial excitation of the fundamental mode i.e. the total initial energy is in the mode "1" in Fig. 2.1, they were expecting for the equipartition of the energy over the modes, as predicted by the statistical physics. In Fig. 2.1, the energy evolution of the five lowest modes is plotted over the simulation cycles (which can be converted into a time scale). The energy, initially contained in the fundamental mode, is distributed to the higher-order eigenmodes. However, while the mode "1" reaches a minimum and the mode "2" a maximum at around 14 thousands cycles, the energy transfers reverse until the system returns back to its initial state (in fact it is not perfectly back to the initial state, which is reached after a "super-recurrence" [80, 81]). This result was quickly called Fermi-Pasta-Ulam paradox, due to its counter-intuitive nature, and renamed Fermi-Pasta-Ulam recurrences once the paradox was no longer one and had been understood. With the high performances of modern computers,

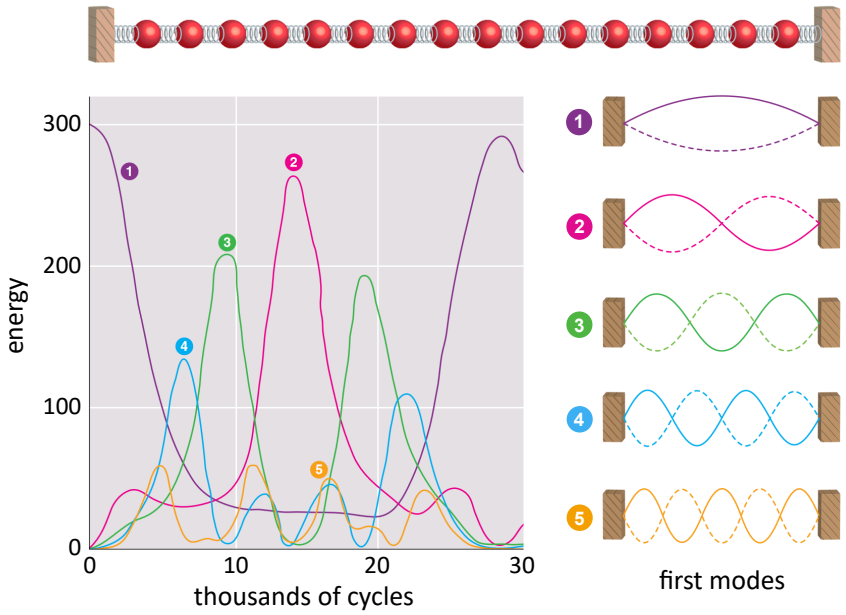

Figure 2.1: Chain of masses model with N=16. Energy (kinetic plus potential) evolutions of the first 5 oscillator modes for N=32 and a quadratic nonlinearity. Adapted from [79].

recent studies have shown that the oscillators chain thermalization, which was initially expected by the scientists, is reached after several recurrences [82–84]. Since recently, Mary Tsingou's great contribution to this discovery is progressively brought to light thanks to the publications of Thierry Dauxois on the subject [85–87]. We will preferably talk about Fermi-Pasta-Ulam-Tsingou recurrences now, and this is what we will do all along this manuscript. The solution of this paradox was found in 1965 by Zabusky and Kruskal in terms of solitons through the numerical solutions of the Korteweg-de Vries equation [31], which are presented in Fig. 2.2. While in the FPUT problem they studied the system in the Fourier space, i.e. the oscillator modes energy evolutions, the solution in the solitonic regime is obtained by looking at the evolution of the system in the real space. In their system, the initial excitation evolves and breaks into solitary waves (solitons), each with their own relative speed. After a certain time, the solitons get closer from each other until they all rejoin, returning then to the initial excitation state and completing a FPUT recurrence. The FPUT experiment had then a great impact on numerical simulations but also paved the way of nonlinear physics. Following these seminal works, solitons have been rapidly observed in optical fibers from the equilibrium between the Kerr effect and the anomalous dispersion [88], as predicted by the theory [89, 90]. While the Kerr effect leads to the temporal broadening of a

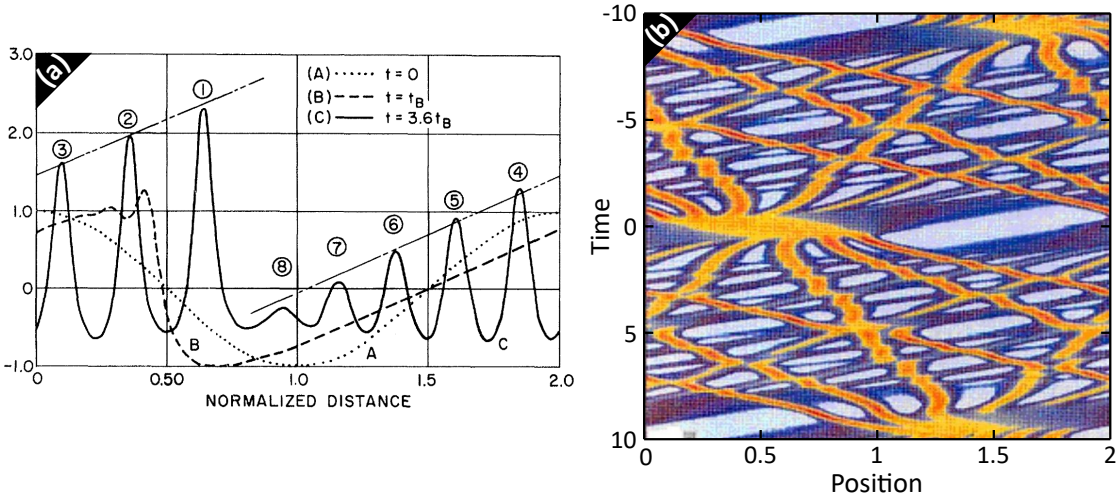

Figure 2.2: Korteweg-de Vries equation numerics. (a) Evolution of the initial condition at three distinct instants, from [31]. (b) False color plot spatio-temporal evolution of the system, from N. J. Zabusky.

pulse beam with the low frequencies shifting to the pulse front edge, the anomalous dispersion produces the opposite effect. Short pulses can then propagate inside a fiber without distortion, maintaining their shape, or with a periodic shape evolution, that may have a particular interest for telecommunications at some points. In the case of a CW beam, the simultaneous effects of GVD and SPM is although at the origin of weak perturbations instability, known as MI. This phenomenon also generates the appearance of solitonic structures, which will be described later on in this chapter.

2.2 Modulation instability theory

MI is a phenomenon resulting from the amplification of a weak perturbation on top of a plane wave during the propagation into a dispersive nonlinear medium. Also known as Benjamin-Feir instability in water waves [17] or Bespalov-Talanov instability in optics [16], this phenomenon is ubiquitous in physics [18] as it has also been observed in Bose-Einstein condensates [19], in plasmas [20] and in fiber optics [15]. It has been extensively studied particularly for its key role in the rogue wave formation [21–26] and supercontinuum generation [27]. In this section, we will first present the linear stability analysis of a perturbed solution in a system governed by the NLSE, commonly used to describe the linear MI stage and get the phase-matching condition. Then, we will display a numerical example of noise-induced MI and highlight the limit of the linear

stage description.

2.2.1 Linear stability analysis

To describe the unstable frequency band and the parameters of the parametric gain from MI, it is convenient to perform a linear stability analysis of a perturbed solution of the NLSE 1.10. The stationary solutions of this equation have the form $E(z,T) = E_0 e^{i\gamma P_0 z}$, where E_0 is the amplitude of the wave such as $|E_0|^2 = P_0$. On this stationary solution is added a small perturbation $\epsilon(z,T)$, with $|\epsilon|^2 \ll P_0$:

$$E = (E_0 + \epsilon(z,T))e^{i\gamma P_0 z} \tag{2.1}$$

By injecting Eq. 2.1 in Eq. 1.10 and by linearising in ϵ, we obtain the following propagation equation:

$$\frac{\partial \epsilon}{\partial z} = -i\frac{\beta_2}{2}\frac{\partial^2 \epsilon}{\partial T^2} + i\gamma P_0(\epsilon + \epsilon^*) \tag{2.2}$$

To find the dispersion relation from 2.2, we consider ϵ in the general form of:

$$\epsilon = u + iv \text{ with } u(z,T) = u_0 cos(\Omega T - Kz) \text{ and } v(z,T) = v_0 sin(\Omega T - Kz) \tag{2.3}$$

where K is the propagation constant and Ω the perturbation angular frequency. The injection of Eq. 2.3 in Eq. 2.2 gives these two coupled equations, obtained by splitting the real and imaginary parts:

$$\begin{aligned} \frac{\partial u}{\partial z} &= \frac{\beta_2}{2}\frac{\partial^2 v}{\partial T^2} \\ \frac{\partial v}{\partial z} &= -\frac{\beta_2}{2}\frac{\partial^2 u}{\partial T^2} + 2\gamma P_0 u \end{aligned} \tag{2.4}$$

By using the expressions of u and v in Eq. 2.3, we simplify the system and put it in a matrix form:

$$\begin{pmatrix} K & \frac{\beta_2}{2}\Omega^2 \\ \frac{\beta_2}{2}\Omega^2 + 2\gamma P_0 & K \end{pmatrix}\begin{pmatrix} u_0 \\ v_0 \end{pmatrix} = 0 \tag{2.5}$$

To get the non-trivial solutions of Eq. 2.5, we find the conditions so that the determinant of the matrix is 0 and we get the following dispersion relation:

$$K = \pm\sqrt{\frac{\beta_2}{2}\Omega^2\left(\frac{\beta_2}{2}\Omega^2 + 2\gamma P_0\right)} \tag{2.6}$$

Considering Eq. 2.6, K is a priori a complex quantity, so we set $K = k_1 + ik_2$, with $(k_1, k_2) \in \mathbb{R}^2$, and inject it in Eq. 2.3. The power associated to the perturbation ϵ is:

$$|\epsilon(z,t)|^2 = \left(\frac{u_0 + v_0}{2}\right)^2 e^{2k_2 z} + \left(\frac{u_0 - v_0}{2}\right)^2 e^{-2k_2 z} \tag{2.7}$$

Whatever the sign of k_2 is, the perturbation will be amplified by a power gain g, such as $g(\Omega) = 2|k_2|$: it is the MI phenomenon. If we are in the normal dispersion regime ($\beta_2 > 0$), the propagation constant K remains real, so $k_2 = 0$ and $g(\Omega) = 0$. MI (considering only β_2) is then not observed in the normal dispersion regime. On the contrary, if we are in the anomalous dispersion regime ($\beta_2 < 0$), the argument of the square root in 2.6 can be negative and so the propagation constant K can have an imaginary part ($k_2 \neq 0$ a priori). The MI gain band is given by the frequencies Ω which verify that $\frac{\beta_2}{2}\Omega^2\left(\frac{\beta_2}{2}\Omega^2 + 2\gamma P_0\right) < 0$. Such frequencies are then contained in the interval $-\Omega_c < \Omega < \Omega_c$ with Ω_c the cutoff frequency:

$$\Omega_c = 2\sqrt{\frac{\gamma P_0}{|\beta_2|}} \tag{2.8}$$

This gain band is defined as the unstable band from the MI process i.e. the frequencies within this gain will be amplified during the propagation. Below and beyond this band, the gain is zero and the frequencies are stable. The corresponding gain curve is depicted in Fig. 2.3. (a) for typical values of β_2, γ and P_0 we used in our experiments (SMF-28 fiber). It corresponds to two sidelobes, symmetric to the pump frequency where the gain

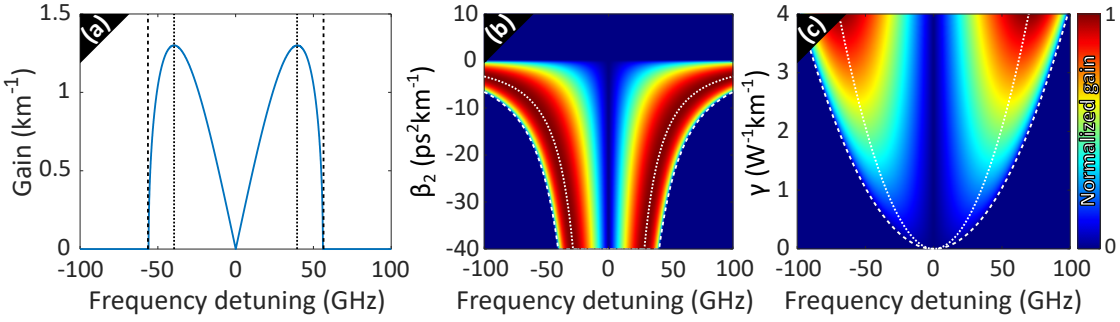

Figure 2.3: (a) MI gain curve with $P_0 = 500$ mW, $\beta_2 = -21$ ps^{2}km^{-1}, $\gamma = 1.3$ W^{-1}km^{-1}. Evolution of the gain curve as a function of (b) β_2 and (c) γ. Dotted lines refer to the MI phase-matching frequency from Eq. 2.10 and dashed lines to the MI cutoff frequency from Eq. 2.8.

is zero. In dashed lines are plotted the limits of the gain band $\Omega = \{-\Omega_c, \Omega_c\}$ while in dotted lines are plotted the maximum gain frequencies $\Omega = \{-\Omega_0, \Omega_0\}$. Ω_0 expression is

obtained by the maximum calculation of K, through the phase-matching relation:

$$\beta_2 \Omega_0^2 + 2\gamma P_0 = 0 \tag{2.9}$$

and so Ω_0 is:

$$\Omega_0 = \sqrt{\frac{2\gamma P_0}{|\beta_2|}} = \frac{\Omega_c}{\sqrt{2}} \tag{2.10}$$

The evolution of the MI gain band curve as a function of the dispersive factor β_2 and the nonlinear coefficient γ are displayed in Fig. 2.3. (b) and (c) respectively. The gain band broadens when β_2 is getting closer to the ZDW, but the maximum of gain remains constant. The MI process is logically enhanced (the unstable frequency band expands and the relative gain rises) when the nonlinearity is increased. The instability gain band calculated here is reduced to the anomalous dispersion regime, with neglected higher order dispersion terms. However, MI can occur in the normal dispersion regime by adding another degree of freedom. A parametric gain can then be observed considering additional dispersion terms [91, 92], the propagation in a cavity [93], weakly birefringent fibers [94, 95] or dispersion modulated topographic fibers [96, 97]. The latter will be investigated in Chapter 7.

2.2.2 Noise-driven modulation growth

An example of the influence of MI from a monochromatic laser, under realistic conditions (non negligible noise floor), is displayed in Fig. 2.4. We plotted the power evolution along the fiber length of both the pump (solid blue line) and a noise component located at the perfect MI phase-matching, at $\Omega = \Omega_0$ (solid red line). We notice that up to $z = 6$ km the pump remains almost undepleted, which corresponds to the stage of linear MI regime (grey zone). The amplification process follows then the one predicted by the linear stability analysis, with the phase-matching frequency fitting the power exponential growth with the gain $G = exp(\gamma P_0 z)$ (dotted grey line). Of course, an infinite exponential growth is unphysical and beyond this stage, the pump power begins then to drop as a signature of the saturation. The power of the Ω_0 noise contribution doesn't follow an exponential growth anymore and even reach a maximum around $z = 11$ km. The linear stability analysis is then insufficient to describe this stage. Then, we observe power oscillations of both components, sometimes referred as spontaneous FPUT recurrences [98, 99]. The evolution of the spectrum along the fiber length is plotted in Fig. 2.4. (b) for a single shot of noisy initial condition. In Fig. 2.4. (c, d, e) are

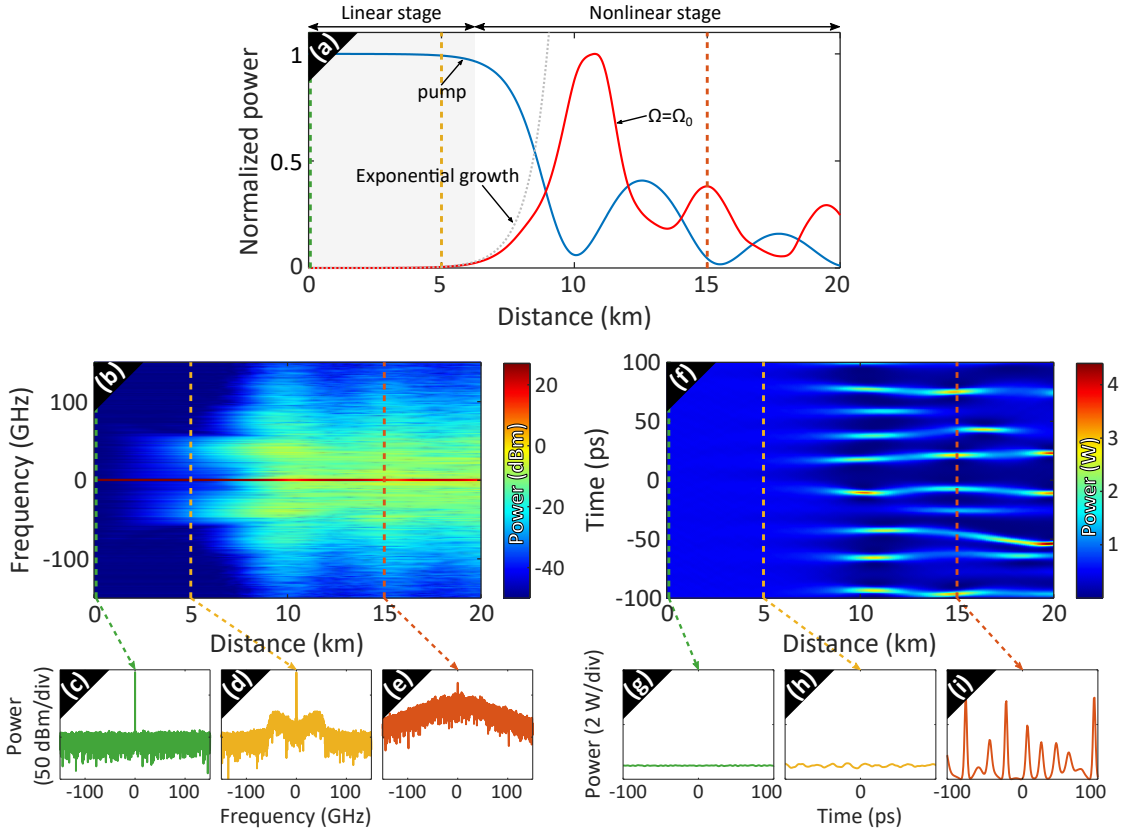

Figure 2.4: Single-shot noise-induced MI numerics. (a) Pump power (blue line) and noise component at $\Omega = \Omega_0$ power (red line) evolutions along the fiber length. (b) Spatio-spectral and (f) spatio-temporal evolutions of the power along the fiber distance. Parameters: same as Fig. 2.3 and the initial noise floor is set with a power spectra density of -127 dBm/Hz. (c, d, e) Spectra and (g, h, i) time profiles at $z = 0$, 5 and 15 km respectively.

plotted the corresponding spectra for $z = 0$, 5 and 15 km. At the beginning, up to $z = 6$ km, only the frequencies within the MI gain band are amplified, as seen in the subplot (d) (linear stage). Then, the spectrum broadens due to FWM into a triangular frequency continuum, as presented in the subplot (e) (nonlinear stage). The evolution in the time domain is displayed in Fig. 2.4. (f) and the $z = 0$, 5 and 15 km corresponding time profiles in Fig. 2.4. (g, h, i). From a low noise modulation of the plane wave background, the system evolves progressively towards the irregular and chaotic appearance of high power pulses. We can distinguish solitonic structures, as previously reported in [98, 100–103]. Due to the noisy fluctuations of the plane wave beam, the system exhibits an irreversible behavior and doesn't come back to its initial state when the amplification

stage saturates. However, a coherent and controlled modulation of the CW pump allows to get a reversible system. Repeated growth and decay cycles may be observed, referred to as FPUT recurrences. In this case, the system also reaches very quickly the pump saturation and it requires then also a description of the nonlinear stage dynamic.

2.3 Nonlinear MI-induced Fermi-Pasta-Ulam-Tsingou recurrences

A weak coherent modulation of a plane wave with a frequency unstable to MI will be exponentially amplified at the early stage of the propagation. However an infinite growth, as predicted by the linear theory, is unphysical. We have then to consider a nonlinear amplification stage when the amplitude of the seed wave and the CW pump depletion are no longer negligible. The nonlinear stage of MI predicts the modulation growth saturation before its decay, until the return to the initial state, a weakly modulated plane wave. These cycles, which can be repeated, are denoted FPUT recurrences. Such behavior has been observed in many fields of physics involving focusing cubic media, such as hydrodynamics [32, 39], planar waveguides [104], magnetic feedback rings [105], bulk crystal optics [106], and of course fiber optics [30, 34, 37, 41, 42, 107–109]. In this section, we will present the tools to describe this nonlinear stage of MI. First, we will introduce the recursive dynamics associated to the nonlinear MI stage through numerical simulations. Then, we will present analytical solutions and models, describing and predicting the FPUT recurrences, through the solitons on finite background solutions and the three-wave mixing (3WM) model.

2.3.1 Numerical example of FPUT dynamics

The coherently-driven MI is obtained by a weak amplitude or phase coherent modulation of the CW background pump with a characteristic frequency inside the MI unstable band of the plane wave. While at the beginning of the propagation, the amplification of the weak modulation through the MI process can be predicted by the gain calculation of the linear stability analysis, the nonlinear stage induced by the pump depletion prevents from any analytical prediction beyond. To illustrate the recursive dynamics from the MI of a three waves input (three modes in the Fourier domain corresponding to a CW pump and symmetric sidebands from a sine/cosine modulation), we perform numerics of the NLSE using the split-step Fourier method, which are displayed in Fig. 2.5.

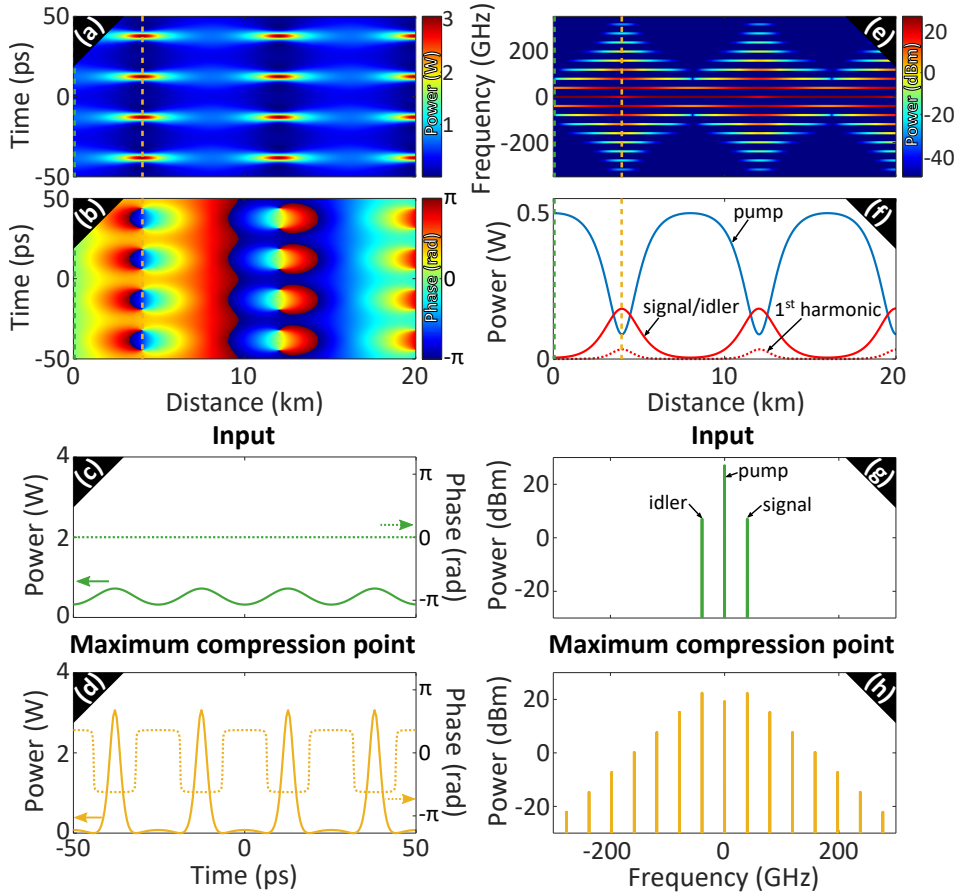

Figure 2.5: Coherently-driven MI numerics. Spatio-temporal evolutions of the (a) power and (b) phase along the fiber distance. (e) Spatio-spectral power evolution. (f) Pump (solid blue line), signal or idler (solid red line) and first harmonic at $f = 2f_m$ (dotted red line). (c, d) Power and phase time profiles and (g, h) power spectra at $z = 0$ and $z \simeq 4km$ (maximum modulation growth) respectively. Parameters: same as in Fig. 2.3 with also $P_s(z=0) = P_i(z=0) = 5$ mW, $\Delta\Phi(z=0) = 0$ (amplitude modulation) and $f_m = 39.6$ GHz.

The input signal is in the general form:

$$\begin{aligned} &E(z=0,T) = E_p(z=0) + E_s(z=0)e^{i\Omega_m T} + E_i(z=0)e^{-i\Omega_m T} \\ &\text{with } E_{p,s,i} = |E_{p,s,i}|e^{i\phi_{p,s,i}} \end{aligned} \tag{2.11}$$

where $E_{p,s,i}$ are the amplitudes of the pump, signal and idler waves, $\phi_{p,s,i}$ their respective phases and Ω_m the modulation angular frequency. To get a cosine amplitude modulated plane wave, we first consider the signal and idler waves initially symmetrical i.e. $|E_s(z=0)| = |E_i(z=0)|$ and $\phi_s(z=0) = \phi_i(z=0)$. Then, the relative phase $\Delta\Phi = \phi_p - \phi_s$ needs

to be a multiple of π and here we set $\Delta\Phi(z=0)=0$. The plane wave pump is set with the power $|E_p(z=0)|^2 = P_p(z=0) = 500$ mW and the modulation waves with the power $|E_s(z=0)|^2 = P_s(z=0) = 5$ mW. The signal propagates in a lossless fiber with the following parameters: a dispersion coefficient $\beta_2 = -21$ p^{2}km^{-1}, a nonlinear coefficient $\gamma = 1.3$ W^{-1}km^{-1} (SMF-28 fiber parameters, as in Fig. 2.3). The MI phase-matching relation from Eq. 2.10 of this fiber and this pump gives a maximum gain frequency $f_0 = \frac{\Omega_0}{2\pi} = 39.6$ GHz (Fig. 2.3. (a)). The modulation frequency f_m, such as $f_m = \frac{\Omega_m}{2\pi}$, is set to the value of f_0. Fig. 2.5. (a) and (b) display the temporal profile evolutions of the power and the phase respectively and Fig. 2.5. (c) the input signal power (solid green line) and phase (dotted green line) time distributions. The signal is initially amplitude modulated, so the power evolves as a cosine wave in [320 mW;720 mW] while the phase is constant, equal to 0. The modulation frequency being inside the MI gain band, the modulation is progressively amplified during the propagation, at the expense of the plane wave. The cosine wave is distorted until the system reaches a maximum compression point around $z = 4$ km, characterized by a train of very high power pulses. The power and phases profiles at this maximum compression point are potted in Fig. 2.5. (d). These high power pulses are located at the same time spots as the power maxima of the cosine wave and reach around 3 W peak power. We also notice two distinct evolutions of the phase according to the extrema of the initial cosine power distribution, whose phase-shift reaches a maximum of π at the compression point. Then, the process reverses and the system returns back to its initial state around $z = 8$ km, both in power and phase. A first FPUT recurrence is completed and the process repeats itself for one and a half more cycle in the remaining propagation distance. In the right panel the data are presented in the Fourier domain this time. In Fig. 2.5. (e) the power evolution of the spectrum is plotted while in Fig. 2.5. (f) the power evolution of the main Fourier modes, the pump (solid blue line), the signal/idler (solid red line) and the first harmonic (dotted red line), are displayed. Initially very weak, the modulation waves E_s and E_i are amplified due to the MI process and the first harmonic due to FWM, all at the expense of the pump wave E_p whose power decreases in the same time. The signal and idler powers increase from 5 mW to 172 mW, while the pump power decreases from 500 mW to 86 mW. We notice from the spectrum evolution that the spectrum broadens into a frequency comb with a maximal broadening at the compression point. Looking at the input (green spectral lines) and maximum compression point (yellow spectral lines) spectra from Fig 2.5. (g) and (h) respectively, the 3 waves input evolves then in a triangular shaped frequency comb [28], due to multiple cascaded FWM processes. Beyond the maximum compression point, the system returns back to its initial state

through energy transfers from the signal, idler and higher orders sidebands waves to the pump wave.

2.3.2 Solitons on finite background

The solitons on finite background, also called breathers, are a solution class of the focusing NLSE which interest us particularly. Indeed such solutions originate from the perturbation of a plane wave and then seem to be a good starting point to describe the FPUT dynamics. For convenience in the formulation of the solutions, the NLSE from Eq.1.10 is set in the dimensionless form:

$$i\frac{\partial\psi}{\partial\xi}+\frac{1}{2}\frac{\partial^2\psi}{\partial\tau^2}+|\psi|^2\psi=0 \tag{2.12}$$

where the variable changes applied are $\xi=\frac{z}{L_{NL}}$, with L_{NL} the nonlinear length defined as $L_{NL}=\frac{1}{\gamma P_0}$, $\tau=\frac{T}{T_0}=\frac{T}{\sqrt{|\beta_2|L_{NL}}}$ and $\psi=\frac{E}{\sqrt{P_0}}$. The space and time breather solution of Eq.2.12 is written, according to [35]:

$$\psi(\xi,\tau)=\left[1+\frac{2(1-2a)cosh(b\xi)+ibsinh(b\xi)}{\sqrt{2a}cos(\omega\tau)-cosh(b\xi)}\right]e^{i\xi} \tag{2.13}$$

The parameter a is commonly used to characterize the type of solution, while b and ω are expressed as functions of a, with $b=\sqrt{8a(1-2a)}$ and $\omega=2\sqrt{1-2a}$. Depending on the a value, three solution types are defined, the Akhmediev breather (AB) [35, 37], the Kuznetsov-Ma soliton (KM) [38, 110, 111] and the Peregrine soliton (PS) [36, 112]. They are displayed in Fig. 2.6.(a), (b) and (c) and their specifications are developed in Table 2.1. The type of solution that interests us the most for the study of the FPUT

	Akhmediev breather	Kuznetsov-Ma soliton	Peregrine soliton
a	$[0;0.5[$	$]0.5;+\infty[$	0.5
b	$\in\mathbb{R}$	$\in\mathbb{I}$	0
ω	$\in\mathbb{R}$	$\in\mathbb{I}$	0
τ	periodic	localized	localized
ξ	localized	periodic	localized

Table 2.1: Solitons on finite background properties

recurrences is the AB. Indeed this solution corresponds to a single cycle of growth and decay from a vanishing periodic sine modulation. At an infinite distance before the maximum compression point, an infinitesimal sine modulation is superimposed on a

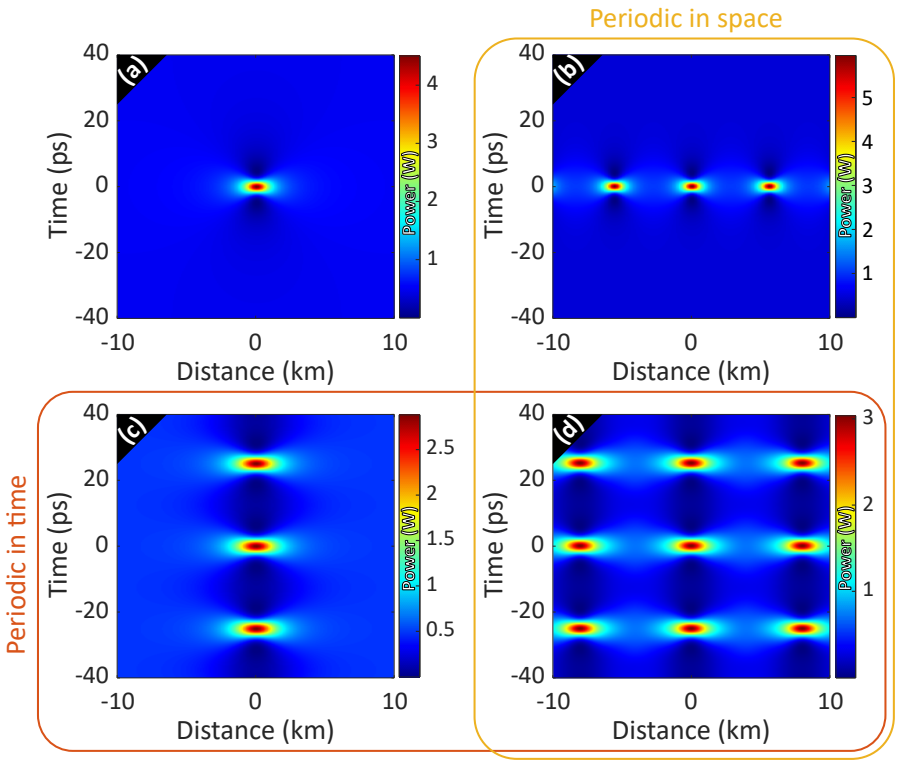

Figure 2.6: Solitons on CW background solutions with physical variables. (a) PS with $a = 0.5$. (b) KM soliton with $a = 0.75$. (c) AB with $a = 0.25$. (d) Numerics with a realistic 3 waves input (shifted to have a growth maxima at $z = 0$).

powerful CW background. This modulation progressively grows with the propagation distance until the system evolves, at the maximum compression point, into a train of periodic high power pulses. It is then followed by a decay stage, with the return at infinite distance to the initial state of a vanishing modulation on a plane wave. The modulation power decay is accompanied by a phase shift of the solution [113]. The FPUT recurrences dynamics, presented in the previous subsection, can then be described as a periodic repetition of AB growth and decay cycles along the propagation distance. For a comparison purpose, numerics with a realistic 3 waves excitation is displayed in Fig. 2.6. (d). However, the AB solution remains limited to model the MI-induced FPUT recurrences, as it is a simply periodic solution in time as seen in Fig. 2.6. (c) (the KM soliton is also a simply periodic solution but in space as seen in Fig. 2.6. (b)). Indeed, the AB dynamics only accounts for a single maximum compression point, and so a single growth and decay cycle, then it doesn't contain the desired doubly periodic recursive feature. Moreover, this solution takes into consideration an initial vanishing

modulation and can only model very weak modulation regimes, which is rarely the case in experiments with realistic conditions. Therefore, the AB dynamics and its ability to describe FPUT recurrences are investigated in [114] under realistic and experimental-like conditions. From this analytical study, a formula of the initial relative phase between the pump and the sidebands, $\Delta\Phi(z=0) = \phi_P(z=0) - \phi_S(z=0)$, is derived to excite an AB from a 3 waves initial excitation. This specific relative phase value is noted $\Delta\Phi_{AB}$ with:

$$\Delta\Phi_{AB} = \frac{1}{2} cos^{-1}(1-4a) \tag{2.14}$$

However the AB solution remains insufficient to describe analytically the recurrences dynamics and another NLSE solution is needed. A more complete description is obtained with the doubly-periodic solutions [51, 52], which will be detailed in Chapter 4. On their side, Grinevich and Santini investigated the NLSE equation with a weakly modulated plane wave excitation (3 waves input) through matched asymptotic expansion techniques [115]. They managed to match the perturbation theory with the AB solution to get a recursive dynamics and derived simple formulas to predict the position of the maximum compression points.

2.3.3 The truncated three-wave mixing model

To study the nonlinear stage of MI, it is possible to truncate the system to a limited number of waves, centered around the pump, and to obtain a much simpler coupled equations system [116, 117]. As the coherently-driven MI process requires an input of only 3 waves, it is convenient to use a truncated three-wave mixing (3WM) model, considering only the pump, signal and idler waves. The higher-order harmonics, generated through multiple cascading FWM processes, are neglected here. The field envelope can be written:

$$E(z) = E_p(z) + E_s(z)e^{i\Omega_m T} + E_i(z)e^{-i\Omega_m T} \tag{2.15}$$

while the different terms account for the pump, the signal and the idler waves fields respectively. Of course, the field in Eq. 2.15 has the same input form as the general case of coherently-driven MI in Eq. 2.11, but the propagation dynamic is only conducted by these 3 waves. By injecting the equation 2.15 inside the NLSE 1.10 and gathering the

terms with their frequency, we get the following set of coupled equations:

$$\begin{aligned}
\frac{dE_p}{dz} &= i\gamma\left(|E_p|^2 + 2|E_s|^2 + 2|E_i|^2\right)E_p + 2i\gamma E_s E_i E_p^* \\
\frac{dE_s}{dz} &= i\frac{\beta_2}{2}\Omega^2 E_s + i\gamma\left(|E_s|^2 + 2|E_p|^2 + 2|E_i|^2\right)E_s + 2i\gamma E_p^2 E_i^* \\
\frac{dE_i}{dz} &= i\frac{\beta_2}{2}\Omega^2 E_i + i\gamma\left(|E_i|^2 + 2|E_p|^2 + 2|E_s|^2\right)E_i + 2i\gamma E_p^2 E_s^*
\end{aligned} \tag{2.16}$$

By developing the fields as $E_{p,s,i} = |E_{p,s,i}|e^{i\phi_{p,s,i}}$ with $|E_{p,s,i}|^2 = P_{p,s,i}$ and defining the relative phase $\Delta\Phi = \frac{1}{2}(2\Phi_p - \Phi_s - \Phi_i)$, we can rewrite the coupled equations from Eq. 2.16, by splitting the real and imaginary parts, as follows:

$$\begin{aligned}
\frac{dP_p}{dz} &= 4\gamma P_p\sqrt{P_s P_i}sin(2\Delta\Phi) \\
\frac{dP_s}{dz} &= -2\gamma P_p\sqrt{P_s P_i}sin(2\Delta\Phi) \\
\frac{dP_i}{dz} &= -2\gamma P_p\sqrt{P_s P_i}sin(2\Delta\Phi) \\
\frac{d\Delta\Phi}{dz} &= -\frac{1}{2}\left[\beta_2\Omega^2 + \gamma(2P_p - P_s - P_i) + \gamma\left(P_p\sqrt{\frac{P_i}{P_s}} + P_p\sqrt{\frac{P_s}{P_i}} - 4\sqrt{P_s P_i}\right)cos(2\Delta\Phi)\right]
\end{aligned} \tag{2.17}$$

If we consider a symmetric modulation i.e. $P_s = P_i$ and $\phi_s = \phi_i$, the coupled equations system from Eq. 2.17 can be simplified. This system of ordinary differential equations is solved through standard numerical methods, of Runge-Kutta for example. An example of resolution is displayed in Fig. 2.7 (orange lines). The parameters are identical to those used for the numerical simulation of the NLSE in the subsection 2.3.1, both for the 3 waves input and the fiber. The power evolutions of both the pump P_p (solid line) and the signal P_s (dotted line), and the relative phase evolution $\Delta\Phi$ as a function of the fiber distance are plotted in the subplots (a) and (b) respectively. For comparison purposes, we display simultaneously the numerical simulations from the NLSE with the same 3 waves input (blue lines). We notice a qualitative agreement, with similar dynamics on both the power and the phase evolutions. However, the truncation leads to a quantitative gap between the 3WM model and the full-spectrum NLSE, as demonstrated in [118]. The most striking differences are the recurrence period and the power conversion ratio. This last is due to the fact that the pump energy is only transferred to the signal and idler waves and not to the full spectrum sidebands. To highlight the phase characteristics of the recurrences, it is convenient to plot the trajectory of the 3 waves dynamic inside a phase-plane $(\eta_s cos(\Delta\Phi), \eta_s sin(\Delta\Phi))$, where η_s is the signal wave fraction of the initial

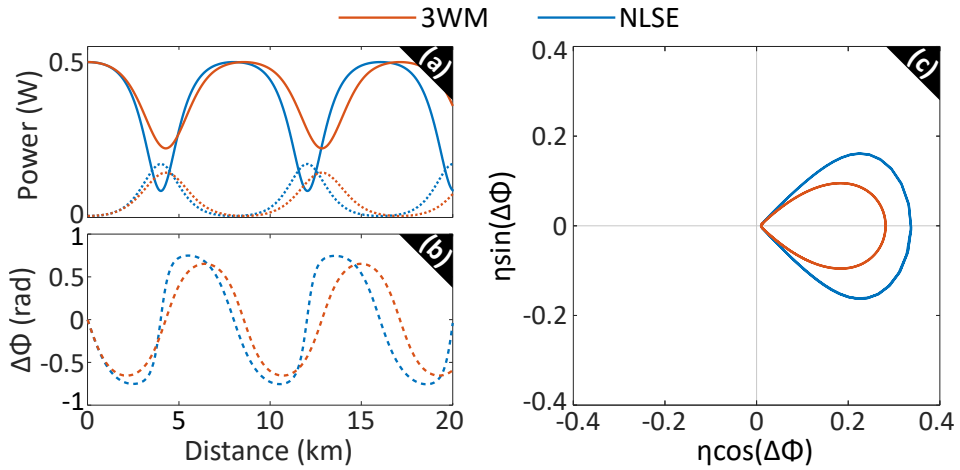

Figure 2.7: (a) Pump power P_p (solid line) and signal power P_s (dotted line) and (b) relative phase $\Delta\Phi$ evolutions along the fiber distance. (c) Representation in the phase-plane $(\eta cos(\Delta\Phi), \eta sin(\Delta\Phi))$. Orange: 3WM model; blue: full-spectrum NLSE numerics. Parameters: same as in Fig. 2.5.

total power such as $\eta_s(z) = \frac{P_s(z)}{P_p(z=0)+2P_s(z=0)}$. The trajectories of the 3WM model example and the NLSE simulations from a 3 waves input are displayed in Fig. 2.7. (c). Except the amplitude gap due to the power conversion difference, the trajectories are similar, looping back on themselves at each recurrence and remaining in the right half-plane. Inspired by what has been done in [108] and especially in [43], we want to quantify the gap between the 3WM model and the full-spectrum dynamics. To do so, we display the evolutions of the spatial period and the maximum signal relative power as a function of the input modulation power in Fig. 2.8. (a) and (b) respectively. From the 3WM

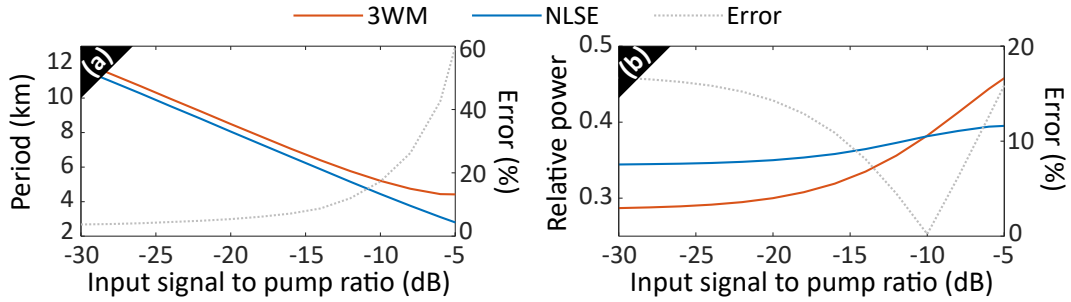

Figure 2.8: (a) Evolution of the spatial period as a function of the input signal to pump ratio. (b) Evolution of the signal relative power at the maximum compression. Orange: 3WM model; blue: full-spectrum NLSE numerics; grey: error of the 3WM model compared to NLSE numerics. Parameters: same as in Fig. 2.5 but with $\Delta\Phi(z=0) = -\frac{\pi}{2}$.

model (solid orange lines) and the NLSE numerics (solid blue lines), we calculated the relative error (dotted grey lines). Concerning the spatial period, the gap increases exponentially with the input signal to noise ratio, from less than 5% at −30 dB to around 60% at −5 dB. The 3WM model seems then to quite correctly predict the location of the maximum compression points of the seeded MI dynamics but for very low input modulation amplitudes. Concerning the signal power maxima, we don't have any quantitative agreement as the 3WM model underestimates the power conversion from the full-spectrum NLSE up to −10 dB and overestimates it beyond. The 3WM model is limited on a quantitative point of view but is an efficient tool to qualitatively apprehend the dynamics of FPUT recurrences induced by coherently driven MI, especially for the phase. The phase-plane trajectories meaning and their different types can be explained through an Hamiltonian approach of the 3WM model. Considering the conservation of the total power (transparent fiber) and a symmetric modulation, the set of coupled equations 2.17 admits then the conservation of the following Hamiltonian along the propagation distance [42, 116, 117]:

$$H(\eta, \Delta\Phi) = \eta(1-\eta)cos(2\Delta\Phi) + (1 - \frac{\omega_m^2}{2})\eta - \frac{3}{4}\eta^2 \tag{2.18}$$

where η is the modulation fraction, $\eta = 2\eta_s$, and ω_m the normalized frequency such as $\omega_m = \frac{2\Omega_m}{\Omega_c}$. It gives the evolution along the propagation distance of η and $\Delta\Phi$ through the equations:

$$\begin{aligned} \frac{d\eta}{d\xi} &= \frac{\partial H}{\partial \Delta\Phi} = -2\eta(1-\eta)sin(2\Delta\Phi) \\ \frac{d\Delta\Phi}{d\xi} &= -\frac{\partial H}{\partial \eta} = (\frac{\omega_m^2}{2} - 1) + \frac{3}{2}\eta - (1-2\eta)cos(2\Delta\Phi) \end{aligned} \tag{2.19}$$

where ξ is the normalized distance. With a set of initial conditions $(\eta(z=0), \Delta\Phi(z=0), \omega_m)$, we obtain a specific trajectory of the waves mixing dynamic in the phase portrait $(\eta cos(\Delta\Phi), \eta sin(\Delta\Phi))$. Multiple trajectories, each corresponding to a level curve of H, are plotted in Fig. 2.9. (a) with $\omega_m = \sqrt{2}$ (maximum MI gain frequency) and different initial conditions of modulation power fraction and relative phase. Two types of trajectories are discernible, separated by a homoclinic orbit [119] (dashed black line), also called separatrix. Either the trajectory is in the separatrix, spinning around one stable point C_0 or C_π and confined in one half-plane (red lines), or it is out of it, surrounding both stable points and crossing both half-planes (green lines). On the right panel, in Fig. 2.9. (b), (c) and (d), we plotted numerics from NLSE with the space-time evolutions of a

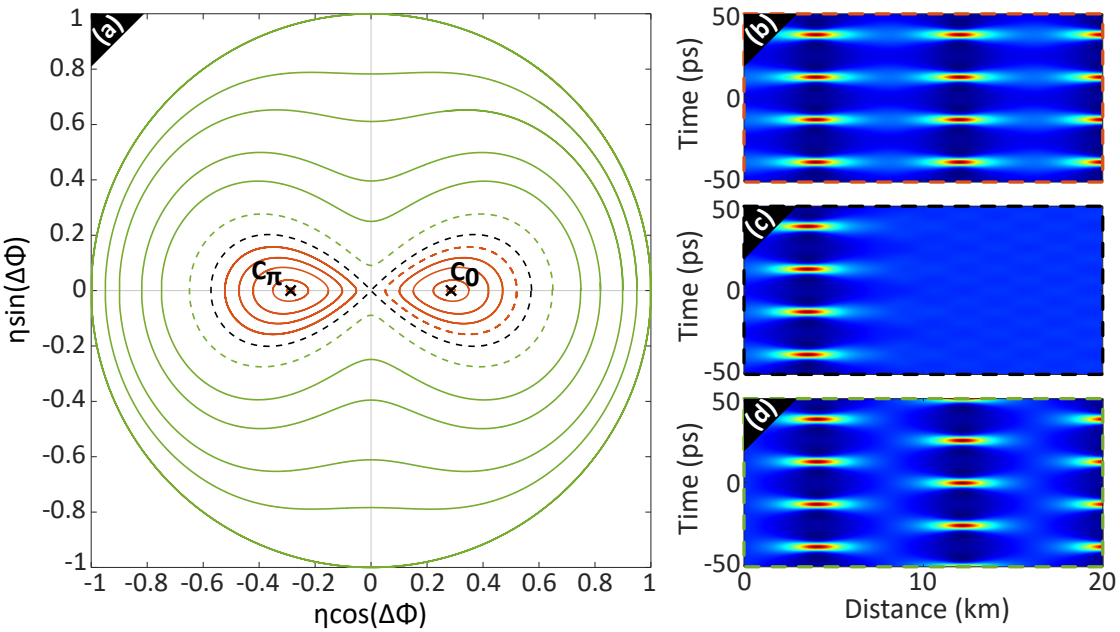

Figure 2.9: (a) Level curves of H in the phase-plane $(\eta cos(\Delta\Phi), \eta sin(\Delta\Phi))$. (b, c, d) Spatio-temporal evolutions of NLSE numerics with $\Delta\Phi(z=0) = \left\{0, \frac{\pi}{4}, \frac{\pi}{2}\right\}$ respectively.

signal from an initial 3 waves input, with $\omega_m = \sqrt{2}$ and $\eta(z=0) = 0.02$. The subplot (b) is performed with $\Delta\Phi(z=0) = 0$ i.e. the initial point is on the right side horizontal axis of the phase-plane and the trajectory is an inner one. We notice that, for two consecutive maximum amplification stages, the high power pulses appear in-phase, with the same temporal locations. Indeed, after one growth and decay cycle, the trajectory returns back to its exact starting point, to its initial state both in amplitude and phase. The following cycles take the same loop path, so the recurrences are in-phase. The subplot (d) is performed with $\Delta\Phi(z=0) = \frac{\pi}{2}$ i.e. the starting point is on the upper side vertical axis and the trajectory is an outer one. For two consecutive maximum compression points, the high power pulses appear phase-shifted by π, shifted by half a temporal period. Indeed, after one growth and decay cycle in one half-plane, the trajectory arrives on the lower side vertical axis, same as the initial conditions in power but with a shift of π for the phase. It then travels the exact same way but in the opposite half-plane, finding back the initial phase after two growth and decay cycles. Such a feature has been observed in hydrodynamics, due to dissipation [39] or controlled by the wind [120], as a loss or gain addition can induce a separatrix crossing from the initial trajectory. We will show in Chapter 6 the complete dynamics behind these separatrix crossings and symmetry breakings induced by an active control of the linear attenuation and

gain of the optical fiber. Also in fiber optics, such dynamic has been demonstrated by driving the initial relative phase from one side to the other of the separatrix [42, 44]. This duality of FPUT recurrences dynamics, either in phase or π-shifted, is referred as the symmetry breaking nature of the process. The limit trajectory between the inner and outer ones, the separatrix, is reached for the phase:

$$\Delta\Phi_{sptx} = cos^{-1}\left(\frac{\omega_m}{2}\right) \tag{2.20}$$

With few trigonometric transformations, we can notice that this separatrix phase is equivalent to the AB phase in Eq. 2.14. The subplot (c) is performed with $\Delta\Phi(z=0) \simeq \Delta\Phi_{sptx} = \frac{\pi}{4}$ (Eq. 2.20 is exact for an initially vanishing modulation). Only a single growth and decay cycle is observed, corresponding to the dynamics of the AB solution. Note that whatever the initial orbit type is, the maximum compression points are reached at $\Delta\Phi = \{0, \pi\}$. For an initial relative phase in $[-\Delta\Phi_{sptx}; \Delta\Phi_{sptx}]$ modulus π, the system exhibits an inner trajectory in the phase-plane, with in-phase recurrences. For the other initial phase values, it exhibits an outer trajectory, with π-shifted recurrences. Pay attention to distinguish this phase-shifted dynamic as the intrinsic symmetry breaking nature of the process from a phase drift occurring with an asymmetric perturbation of the CW background (exponential for example) [121].

Chapter conclusions

In this chapter, we reported the original numerical experiment performed by Fermi, Pasta, Ulam and Tsingou and Zabusky and Kruskal's solution to the paradox by means of solitons fission. Then, MI, which is at the origin of analog FPUT recurrences in focusing cubic media, was investigated. We first developed the calculations for the linear stage of MI, reporting the phase-matching condition and the exponential growth in the vanishing modulation regime. Then, a numerical example of FPUT recurrences was reported, as doubly periodic breathers obtained from the coherently-driven nonlinear stage of MI. The AB solution, one of the soliton of finite background solution of the NLSE, was presented as a good candidate for FPUT description, but limited due to its simple periodicity in time. We also introduced the truncated 3WM model, as a good qualitative tool for FPUT description both for the space periodicity and the phase dynamic (trajectories in the phase portrait, broken symmetry nature).

Chapter 3

Experimental setup

Outline of the current chapter

3.1 Overview of the experimental setup **36**

3.2 Nonlinear pulse shaping **36**

3.3 Distributed measurements **39**

3.4 Phase measurements by heterodyning **41**

3.4.1 Heterodyne detection principle 41

3.4.2 Heterodyning implementation in our setup 42

3.5 Post-processing techniques **44**

3.6 Raman loss compensation **46**

3.7 Stability of the setup **50**

Chapter conclusions **51**

The FPUT recurrences dynamics is investigated with the fantastic test bed that optical fibers represent. Indeed they offer the possibility to control precisely the initial conditions, especially the phase conditions and to get a high stability and repeatability. We can also retrieve the longitudinal dynamics and compensate the attenuation from the propagation along the fiber length, as it will be shown with this setup. It is made of a loss-compensated multi-heterodyning optical time domain reflectometer, principally implemented before and during C. Naveau PhD thesis [43]. The overall functioning, the improvements and the add-ons realized during my PhD work will be detailed in

this chapter. We will present the different stages of the setup: the shaping of the initial excitation into a nonlinear pulse train, the distributed measurements along the fiber length with the OTDR, the heterodyne measurement to retrieve the phase evolution, the post-processing techniques to get low noise and readable traces and the active loss compensation scheme through Raman scattering.

3.1 Overview of the experimental setup

A complete and detailed schematic of the experimental setup is reported in Fig. 3.1. The main stages of the setup are numbered from (1) to (14), that will be referred when necessary during the chapter.

3.2 Nonlinear pulse shaping

To excite a coherently-driven MI regime, the signal has to be shaped into a weakly modulated plane wave i.e. a 3 waves input made of a strong pump and a weak signal/idler pair inside the MI unstable band. The pulse shaping is similar to what is developed in [121, 122]. The initial CW background is generated from a CW laser (1) [NKT Photonics, Koheras BASIK], a very thin and stable DFB laser centered at $\lambda_p = 1550$ nm and with a linewidth around 100 Hz. It passes trough an electro-optic phase modulator (2) [iXblue, MPZ-LN-20], controlled with a doubled RF signal from a synthesizer (20 GHz Agilent E8257D) at the frequency $\frac{f_m}{2}$, creating a frequency comb with a triangular profile. The signal is then shaped into a train of 50 ns pulses with a 9.6 kHz repetition rate (104 μs period) with an electro-optic intensity modulator (3) [iXblue, MXER-LN-20], triggered with an arbitrary wave generator (AWG) (see Channel 1 in Fig. 3.2). We recently added this double RF channels AWG [Tektronix AWG 70000] to simplify and make more flexible the generation of RF pulse trains. It allows to control synchronously the modulation and the detection devices thanks to additional marker channels. On one side the optical pulses are short enough to avoid the stimulated Brillouin scattering (SBS) and get a sufficiently small OTDR resolution (around 10 m). On the other side it is long enough to contain a sufficiently high number of modulation periods (2000 periods for $f_m = 40$ GHz) and then to be consider as continuous for the MI process. To limit the optical noise between two consecutive pulses in the train, we added, before the intensity modulator, a pre-amplifying stage made of a semiconductor booster optical amplifier. From a multiple waves frequency comb, the signal is shaped into the desired 3 waves input with a programmable optical filter (4) [Finisar WaveShaper 1000A]. It is made of a liquid

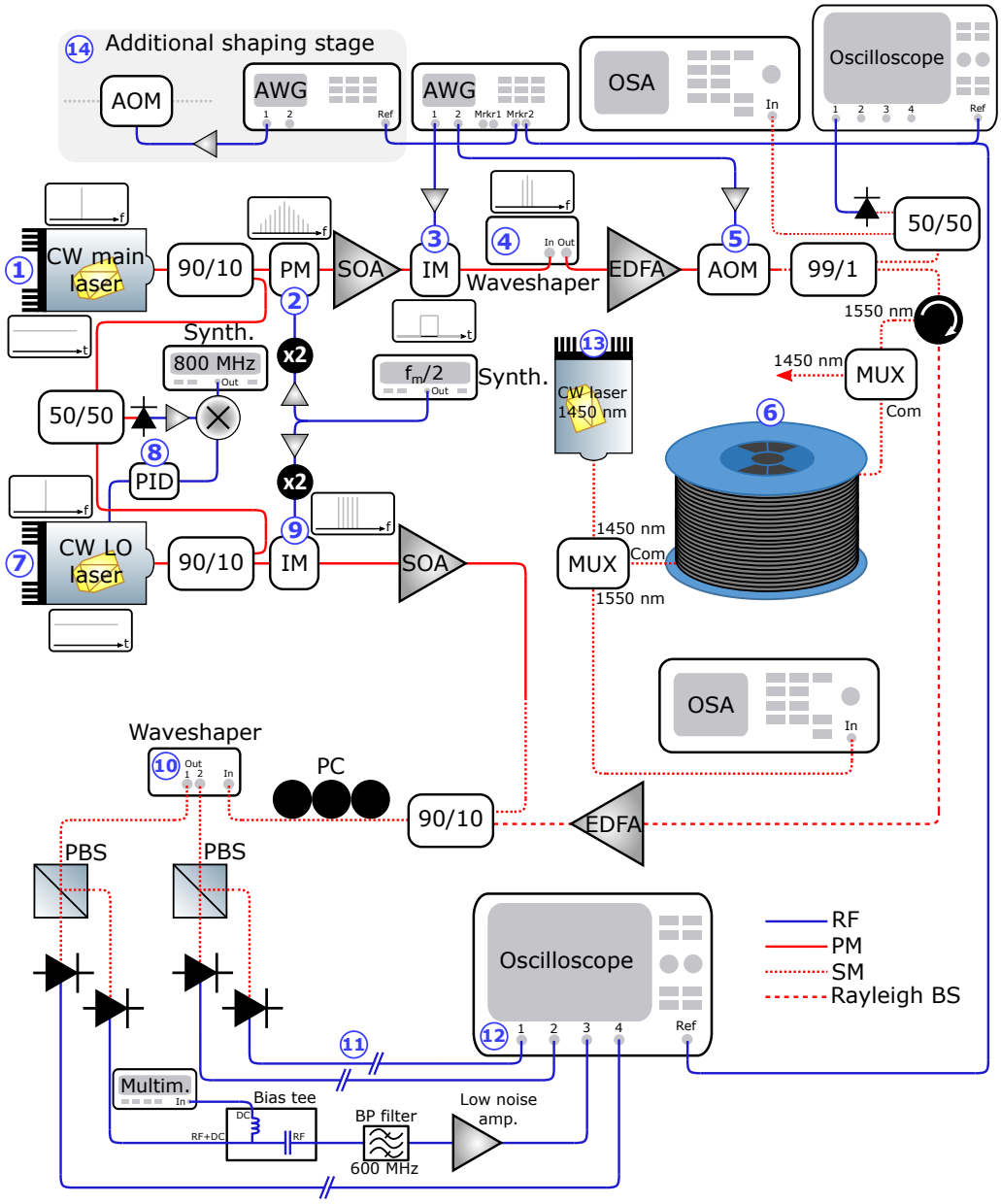

Figure 3.1: Schematic of the experimental setup. PM: electro-optic phase modulator. IM: electro-optic intensity modulator. SOA: semiconductor optical amplifier. EDFA: erbium doped fiber amplifier. AOM: acousto-optic modulator. a/b: coupler with a and b% of the transmitted power in the outputs 1 and 2 respectively. MUX: wavelength division multiplexer. PC: polarization controller. PBS: polarization beam splitter. PID: proportional-integral-derivative controller. OSA: optical spectrum analyzer. AWG: arbitrary wave generator.

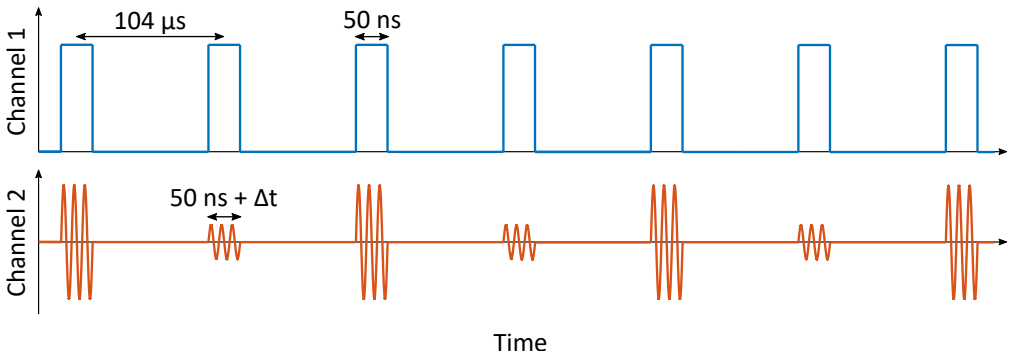

Figure 3.2: RF pulse trains generated by the AWG. The channel 1 drives the IM and the channel 2 drives the AOM.

crystal on silicon processor which acts as a spatial light modulator and allows to control precisely, with a 10 GHz resolution, both the attenuation and the phase. This allows to drive independently the relative power and phase of each frequency line of the comb (as we classically modulate around 40 GHz, beyond the WaveShaper resolution). All the peaks, except the three central ones, are filtered out and the signal and idler waves can be attenuated to get the desired ratio between the plane wave and the modulation. The phases of the waves are set to get the desired relative phase value (it is the initial relative phase value that determines the FPUT recurrences dynamics). The 3 waves input is then perfectly shaped both in relative power and phase, whose spectrum is plotted in Fig. 3.3. (b). At this stage, the pulses remain relatively weak (around tens of mW peak power) and need to be amplified to excite a sufficiently high nonlinear regime (generally more than 10 nonlinear lengths L_{NL} are contained within the fiber length). To do so, the pulses pass through an erbium doped fiber amplifier (EDFA). The modulation frequency f_m is then adjusted to be close to the MI phase-matching condition. To prevent from the noise fading from the OTDR technique [123], an innovative calibration technique is performed on the traces of the nonlinear pulses using the traces from the propagation of linear pulses [43] (detailed later in this chapter). The optical pulse train is then shaped into an alternated train of powerful pulses (to excite a nonlinear propagation regime) and weak pulses (to perform the calibration). To do so, it passes through an acousto-optic modulator (AOM) (5) [Gooch&Housego, Fiber-Q], which attenuates one pulse over two for time multiplexing of the powerful and weak pulses, as displayed in Channel 2 in Fig. 3.2. The 200 MHz RF pulse train triggering the AOM also allows to adapt the maximum fiber length for OTDR measurements and avoid the overlapping between the backscattered light from two different incident pulses. While fibers up to

10.6 km require a 104 μs period between the AOM pulses, longer fibers need longer pulses period. It is then possible to double it by lengthening the fibers up to 21.2 km (208 μs), to triple it for fiber up to 31.8 km (312 μs), etc. Thanks to a more than 50 dB extinction ratio, the AOM also allows to reduce the inter-pulses noise floor, especially since the EDFA has deteriorated the SNR at the previous stage. The signal is ready to be injected in the optical fiber (6). The profiles both in time and frequency are recorded and plotted in Fig. 3.3. From the input time profile in Fig. 3.3. (a), we notice square

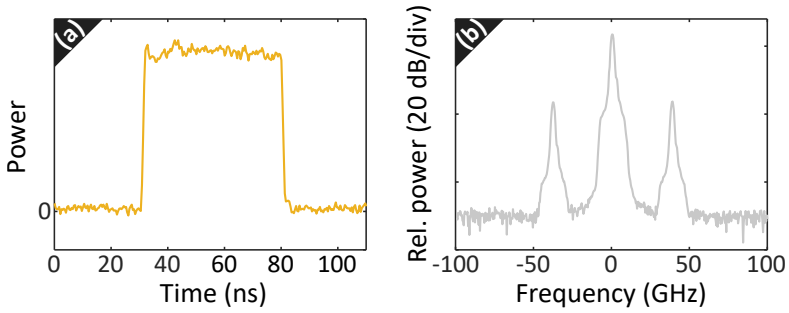

Figure 3.3: (a) Time profile of the pulse at the fiber input. (b) Spectrum at the fiber input.

shaped pulses of 50 ns width. From the input spectrum in Fig. 3.3. (b), we observe a three waves signal made of a powerful pump and symmetric sidebands, 20 dB below the pump here.

3.3 Distributed measurements

In fiber optics experiments, it is easy to measure the characteristics of a signal at both the input and the output of the fiber, as it is done in the setup with optical spectrum analyzers (OSA) [Yokogawa, AQ6370D]. However, to understand the dynamics all along the propagation distance, especially in nonlinear optics, it is necessary to develop methods to retrieve the distribution of the signal in intensity and phase. In the case of FPUT recurrences or breathers dynamics, different techniques have been implemented:

- the cut-back technique, easy to implement but invasive, unrepeatable and long to perform, used in [37, 40, 108] or similarly using multiple different lengths fibers in [124].
- the scaling-law technique, in which the nonlinear length is varied instead of the fiber length but which is also time consuming, used in [34, 36, 107].

- the iterated sequential propagation technique, which allows to get both the power and phase distribution but limited to a truncated spectrum dynamic, used in [118, 125].

- the recirculating loop, which allows to get directly the dime-domain measurement but with an incomplete compensation of the losses, used in [98, 126].

Another technique, the one implemented in our setup, uses the backscattered light from the signal propagating inside the fiber to retrieve distribution informations. Based on an elastic (Rayleigh) or an inelastic (Raman, Brillouin) scattering, it offers the possibility to perform non-destructive, very fast and well resolved measurements [127]. Recording the Rayleigh backscattered light, the optical time domain reflectometry (ODTR) technique is commonly used for fiber attenuation characterization [128], defects localization or temperature sensing. Also implemented in [41] for the FPUT recurrences recording but limited to the intensity distribution, this technique is the one used in this setup to realize distributed measurements. A simplified sketch of the OTDR technique for a breather dynamics is displayed in Fig. 3.4. On the upper side, we plotted an example of the evolution of a pulse along the fiber length, both in the time and the frequency domains, with the characteristic dimensions in the spatial domain to get a scaling perspective. In the following experiments presented, the fiber lengths remain around 20 km. The pulses injected in this fiber are generally 50 ns wide, which corresponds to a spatial width inside the fiber of 10 m. The modulation frequency is generally set around 40 GHz, leading, at maximum compression points, to trains of 25 ps spaced pulses i.e 5 mm spaced in the spatial domain. The fiber is long enough to contain 2000 pulse wide slots and then get a sufficiently precise OTDR resolution, while the pulses contain 2000 modulation periods, which is large enough to consider that the system is operating in a quasi continuous regime. On the lower side, we sketched a space-time diagram of an incident pulse propagating in a L length fiber (in blue) and the corresponding Rayleigh backscattered signal (in green). The latter is retrieved at the fiber input into a pulse of width $\frac{2L}{c_n}$, where c_n is the speed of light in the fiber medium. Each backscattered pulse time slot contains then the power and phase informations of the incident pulse propagating at a specific fiber location. The power of the backscattered light is proportional to the incident signal power and the relation is developped in [129]. According to [130], the Rayleigh backscattered coefficient for a 1 ns pulse at 1550 nm is -82 dB. In our case, with 500 mW and 50 ns pulses, we anticipate backscattered powers around 160 nW. To recover the phase evolutions, a heterodyning detection is performed through a beating between the Rayleigh backscattered light and a reference laser. This technique is developed in

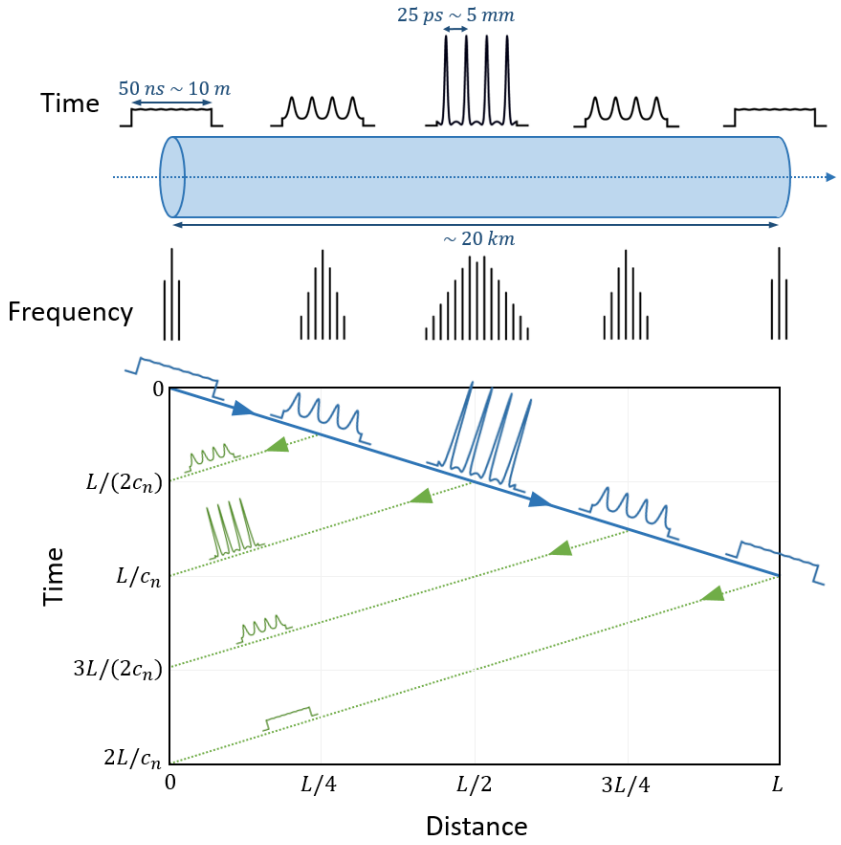

Figure 3.4: Diagram of the OTDR technique. Incident light pulse (solid blue line) and Rayleigh backscattered light (dotted green lines).

the following.

3.4 Phase measurements by heterodyning

3.4.1 Heterodyne detection principle

Let us consider a signal with the frequency f_1 defined as $E_1(t) = E_{0,1}cos(2\pi f_1 t + \phi_1)$ for which we want to record the phase ϕ_1. The intensity measured with a photodiode detector is:

$$I_{PD} = H_{PD}\left(|E_1(t)|^2\right) \tag{3.1}$$

where H_{PD} is the transfer function associated to the photodiode. If $f_{C,PD}$ is the cutoff frequency of the photodiode, the intensity contributions with a frequency higher than $f_{C,PD}$ will be averaged during the detection. The bandwidth of photodiodes are typically

a few GHz, while the telecom frequencies are about 193 THz. Then, if f_1 is at the telecom frequency, the cosine oscillations aren't resolved but averaged by the photodiode and the corresponding detected intensity is:

$$I_{PD} = \frac{1}{2}E_{0,1}^2 \tag{3.2}$$

All the information on the phase ϕ_1 is lost, only the amplitude is recorded. To bypass this issue, we generally use another laser to get a beating frequency with the main laser during the detection within the photodiode bandpass, in the RF domain. We talk about heterodyne (multiple frequencies) detection. The signal from the second laser, which is called reference or local oscillator, have a frequency f_2, slightly shifted from f_1 and is noted $E_2(t) = E_{0,2}cos(2\pi f_2 t + \phi_2)$. The intensity detected is then:

$$I_{PD} = H_{PD}\left(|E_1(t) + E_2(t)|^2\right) \tag{3.3}$$

By developing the calculations, we notice different oscillations, with the frequencies f_1, f_2, $f_1 + f_2$ and $f_1 - f_2$. The frequencies f_1, f_2 and $f_1 + f_2$ are too far from the detector bandwidth and their contributions are averaged during the detection. However, if f_2 is wisely chosen, the beating frequency $f_1 - f_2$ falls in the photodiode bandwidth and the intensity is:

$$I_{PD} = \frac{1}{2}(E_{0,1}^2 + E_{0,2}^2) + E_{0,1}E_{0,2}cos\left((\Omega_1 - \Omega_2)t + (\phi_1 - \phi_2)\right) \tag{3.4}$$

If both the amplitude $E_{0,2}$ and the phase ϕ_2 of the local oscillator remain fixed during the experiment, we retrieve the relative evolution of the amplitude $E_0, 1$ and the phase ϕ_1 of the main signal at the beating frequency $f_1 - f_2$. This also requires the continuous contributions to be filtered out.

3.4.2 Heterodyning implementation in our setup

A second CW laser [CQF938/50 50 mW] (7), the local oscillator, is used for the heterodyne detection. To retrieve the relative phase evolution from the cosine offset in Eq. 3.4, it is necessary to know and set the frequency detuning $f_1 - f_2$ between the main laser and the local oscillator. To do so, a phase-locking method is implemented based on [131]. At the exit of each laser, a small fraction of their signal is collected through 90/10 couplers and mixed together with a 50/50 coupler. The resulting beating at $f_1 - f_2$ is recorded with a photodiode and measured. The result is sent to a PID controller (8)

which modifies the local oscillator phase permanently through a feedback system to maintain it to the frequency of a 800 MHz synthesizer reference. The AOM leading to a shift of the main laser by 200 MHz, the heterodyne detection is then performed at 600 MHz. As we have seen, breathers and FPUT recurrences dynamics leads to the spectral broadening into a frequency comb. It is also interesting to look at the sidedands power and phase evolutions, especially the signal and idler waves for which we know the initial conditions. However, for the moment, the local oscillator only accounts for the beating with the pump, at 600 MHz, as the beatings with the signal and idler are outside of the photodetector bandwidth, at few tens of GHz ($f_m \pm 600$ MHz). The local oscillator is then modulated with an intensity modulator (9) at the frequency f_m (with the same RF synthesizer) to get a frequency comb reference, as presented in Fig. 3.5. (a). Each

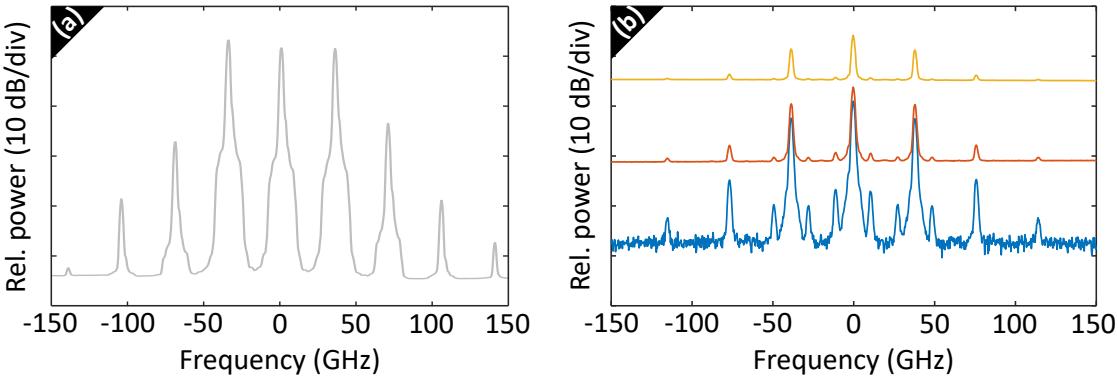

Figure 3.5: (a) Spectrum of the local oscillator. (b) Spectra of the Rayleigh backscattered signal before amplification by the EDFA, with the Raman pump off (solid blue line) and on (solid orange line), after amplification by the EDFA with the Raman pump on (solid yellow line). (a) is extracted from [43].

sideband from the main laser has its own local oscillator with a beating frequency of 600 MHz. The local oscillator is amplified with a SOA, to get a beating signal powerful enough to not be limited by the RF detection circuit noise. The Rayleigh backscattered signal power is very low, of about 160 nW and its spectrum is displayed in Fig. 3.5. (b) with the Raman pump both off (solid blue line) and on (solid orange line). To ensure that it is not limited by the local oscillator noise and the detection noise, the backscattered signal is also amplified with an EDFA designed for very weak signal amplification, up to about 150 mW and displayed in Fig. 3.5. (b) (solid yellow line). We notice that the SNR between the Fourier modes and the noise floor decreased. It is not of great importance as we are performing heterodying measurements and only the power and phase associated to the Fourier modes matter. Note that the weak symmetric sidebands surrounding

the Fourier modes and detuned by 10.9 GHz originate from the spontaneous Brillouin scattering. It gives us clues to prevent from any detrimental SBS as any dissymetry between Stokes and anti-Stokes Brillouin sidebands would be revealing it. Both arms, the local oscillator and the backscattered light, are then combined and pass through a multiple channels programmable filter (10) [Finisar, Wavashaper 4000A], to demultiplex the pump and signal/idler beatings into two distinctive detection channels. We limit the recording to the three central waves as we know the initial conditions only for these waves, which is enough to characterize the FPUT recurrences dynamics both in power and phase. The dynamic of a higher number of central waves, for example 5, can present an interest to get space-time diagrams in standard coherent MI [45] or to get a full insight of the incident waves in higher-order MI [132]. The beatings of both the pump and the signal are splitted at the output of the Waveshaper with a polarization beam splitter to record independently each polarization state with a photodiode. The acquired results are then recombined in post processing as it removes the polarization effects and bypass any polarization scrambling process. However, before being recorded with an oscilloscope, the RF signals from the photodetectors pass through an electronic circuit (11). It is made of a bias tee which separates the useful RF component, obtained by the heterodyning, from the useless DC component, obtained with the averaging by the PD of the out of bandwidth contributions. However, the DC current is still measured to optimize the balance between the polarization states. Then, it is followed by a band pass filter at 600 MHz to remove the maximum of noise and an amplifier. We finally record on a 4 channels 2.5 GHz oscilloscope (12) [Teledyne Lecroy, WavePro 254HD] the temporal traces which are easily converted back in a propagation distance.

3.5 Post-processing techniques

Despite the advantages that offers the OTDR technique, one inconvenient remains, the fading effect that appears as noise in amplitude and phase [123] and which is detrimental in the observation and characterization of the FPUT recurrences. It originates from both the random polarization state of the backscattered light and the speckle from the mixing between the high amount of Rayleigh reflected waves. We displayed, in Fig. 3.6, power and phase traces extracted and adapted from [43]. On the upper side are plotted the power evolutions of the pump (blue line) and the signal (red line) powers and, on the lower side the evolution of the relative phase (green line). The traces in Fig. 3.6. (a) and (e) were obtained without any calibration and exhibit the fading effect from OTDR. We observe very high fluctuations in power, even if we can slightly distinguish

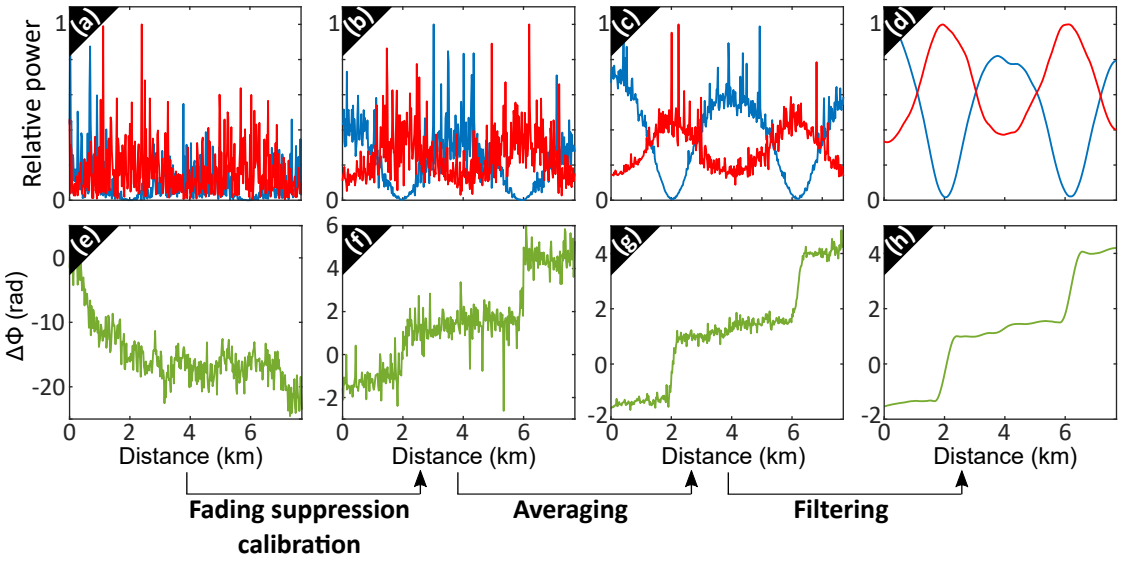

Figure 3.6: Upper side: evolution of the pump (blue line) and signal (red line) powers along the fiber length. Lower side: evolution of the relative phase $\Delta\Phi$ along the fiber length. (a), (e) Single-shot without fading noise calibration. (b), (f) Single-shot with fading noise calibration. (c), (g) Same as before but averaged over a hundred shots. (d), (h) Same as before but filtered. Extracted from [43].

evolution trends, and an apparently random phase evolution. The impact of fading noise on the recorded traces can be reduced in amplitude with averaging techniques [133, 134], or even in phase with frequency- [135] or space-division multiplexing [136]. A simpler technique for amplitude and phase fading noise reduction is implemented in this experimental setup, based on the calibration of the fading noise on the OTDR traces. To do so, we shape the pulse train into an alternation of powerful and weak pulses, as previously presented in Fig. 3.2 on Channel 2. While during its propagation, a powerful pulse will experience the nonlinear and the linear effects, which include the fading noise during the backscattering, a weak pulse will only experience the linear effects. By dividing the traces converted in the Fourier space of the powerful and weak pulses, we are then able to remove all the linear contributions and so to reduce the fading noise. Moreover, the pulse train period is long enough to prevent from the overlapping of the backscattered light but also short enough so we can neglect any thermo-mechanical fluctuation between consecutive powerful and weak pulses. However, as all the linear contributions are removed, it also includes the effect of GVD on the phase, which of course cannot be neglected. Considering the relative phase $\Delta\Phi(z) = \frac{1}{2}(2\phi_p - \phi_s - \phi_i)$, a corrective term of $-\frac{\beta_2}{2}\Omega_m^2 z$ is added to the relative phase during the post-processing. We

make sure that the weak pulses will experience nonlinear interactions that are negligible and we set them 10 dB weaker than the powerful pulses. The FWM processes are then strongly attenuated and the signal/idler pair is located way outside of the MI gain band. Indeed if we consider a modulation frequency f_m close to the MI phase-matching frequency f_0 ($f_c = \sqrt{2}f_0$) of the powerful pulse pump, f_m is higher than the MI cutoff frequency f_0' of the weak pulse pump $\left(f_c' = \frac{f_c}{\sqrt{10}} < \frac{f_c}{\sqrt{2}} = f_0\right)$. The weak pulse power is chosen as a compromise value. Indeed, a too powerful weak pulse would lead to non negligible nonlinear interactions and a wrong calibration of the powerful pulse traces. Conversely, a not enough powerful weak pulse would make the SNR too low to perform a calibration without information losses. The traces with the fading noise suppression technique are plotted in Fig. 3.6. (b) and (f). It highly reduces the power fluctuations and allows to recover a consistent phase evolution. As precised in the previous section, the polarization effects on the backscattered light are treated by recording independently the polarization states, which are recombined during the post-processing. The noise fading free traces are then demodulated with a FFT to get the evolution of power and phase at 600 MHz and the demodulated traces are averaged over a hundred single shot acquisitions. The traces from averaging are plotted in Fig. 3.6. (c) and (g) and we notice a very significant noise reduction on it. Two digital filters are successively applied, a median one and a Savitzky-Golay one, to smooth the traces from noisy fluctuations, as displayed in Fig. 3.6. (d) and (h).

3.6 Raman loss compensation

The optical fiber attenuation is detrimental for the observation of nonlinear effects. Indeed, the nonlinearity of a system depends directly on the intensity of the involved waves. The nonlinear length increases while the power decreases, leading the nonlinear interactions and phenomena to fade with the losses. Moreover, the NLSE equation is not integrable anymore with fiber attenuation, we can then no longer derive analytical solutions to predict the nonlinear phenomena. To prevent this, we made a special effort on optimizing the Raman amplifier based loss compensation scheme with a $\lambda_R = 1450$ nm Raman fiber laser (13) [Keopsys CRFL]. This distributed amplifier allows to actively compensate for the intrinsic losses, thanks to a continuous pump launched at the fiber end and amplifying the signal during the propagation through Raman scattering processes. It has been used for undersea communication channels [137], amplification of picosecond pulses [138], extreme events generation [139] or loss compensation for fundamental investigation [42, 44, 98, 140]. To illustrate the influence of loss compensa-

tion on the FPUT dynamics, we display data traces in Fig. 3.7 with, on the left panel, no Raman amplification and, on the right panel, an optimized compensation, with a counter-propagating Raman pump. The initial relative phase is set to $\Delta\Phi(z=0)=0$.

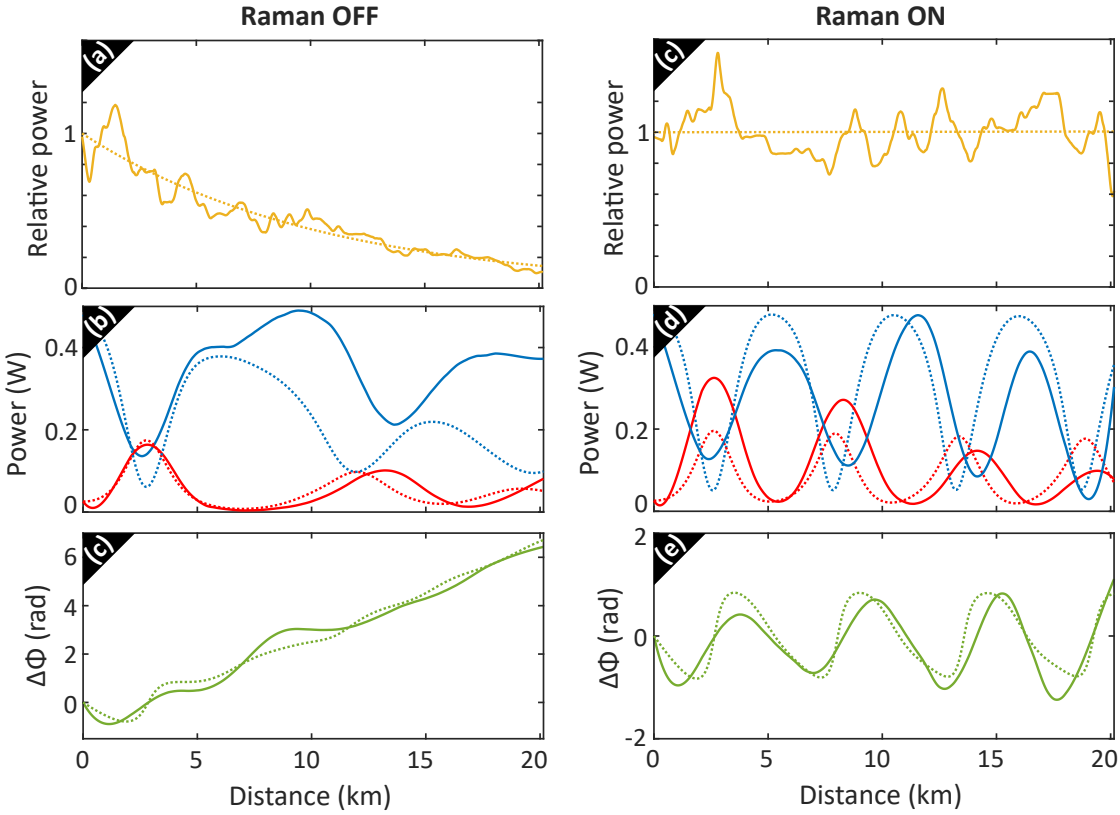

Figure 3.7: Comparison of FPUT recurrences experimental recordings when the Raman compensation is off (left panel) and on (right panel). (a), (c) Peak power evolutions of a weak pulse along the fiber length. (b), (d) Power evolutions of the pump (blue lines) and signal (red lines) waves along the fiber length, and (c), (e) corresponding relative phase evolutions (green lines). Experimental data are displayed in solid lines while numerical data in dotted lines. Parameters: $\beta_2=-19$ ps^{2}km^{-1}, $\gamma=1.3$ W^{-1}km^{-1}, $P_p(z=0)=480$ mW, $P_s(z=0)=P_i(z=0)=24$ mW, $\Delta\Phi(z=0)=0$, $P_R(z=L)=270$ mW.

Through the power evolution from the OTDR of a weak pulse (linear effects only) in Fig. 3.7. (a), we notice an exponential decrease, as expected from Eq. 1.1. The OTDR technique records backscattered signals which suffered twice the fiber attenuation (see Fig. 3.4). The measured attenuation value of 0.21 dB/km is then close to the datasheet value of the SMF-28 fiber of 0.2 dB/km [130]. The total loss suffered by a pulse that propagates over the entire fiber length is more than 4 dB. When the Raman pump is on in Fig. 3.7. (d), the power is globally constant which is an evidence of the good loss

compensation. The power evolutions of the pump and signal/idler waves in the case of FPUT dynamics, is presented in Fig. 3.7. (b) and (d). We notice that the attenuation leads to the slowdown of the recursive dynamic (longer recurrences). The second recurrence appears at 13 km without compensation while at 8 km with compensation. Two recurrences are recorded within the fiber length when the Raman pump is off and almost four recurrences when the pump is on. Moreover, the conversion efficiency from the pump to the sidedands is much lower without Raman amplification as the pump power increases and the signal power decreases for the successive maximum compression points. Indeed, the modulation frequency deviates from the MI phase-matching condition with the losses. If we consider a modulation frequency f_m at the MI phase-matching frequency $f_0 = 40$ GHz and a 4 dB total attenuation after 20 km long fiber propagation, the MI phase-matching frequency at the end of the fiber is $f_0' = 25.2$ GHz and the cutoff frequency $f_c' = 35.7$ GHz. The modulation isn't even located anymore in the unstable band from MI in the last few kilometers of propagation. Note that the pump and signal powers remain relatively high at the fiber center and end despiste the losses, which can be explained by the fading suppression technique that removes the linear effects contributions (including the attenuation). Looking at the relative phase $\Delta\Phi$ evolutions in Fig. 3.7. (c) and (e)., we notice that the phase is also impacted by the losses, increasing up to 2π when the compensation is off but bounded in $\left[-\frac{\pi}{2};\frac{\pi}{2}\right]$ when the compensation is on. The attenuation induces then a priori a change in the symmetry of the FPUT recurrences. This question will be widely investigated in Chapter 6. In addition to provide a better SNR than lumped amplifiers such as EDFA [73], the relative intensity noise transferred from the Raman pump is minimized by implementing the backward pumped configuration [141]. It is possible to improve the loss compensation scheme with an additional forward pump to make it bidirectional [73]. However the signal degradation with the noise is detrimental so we keep the Raman amplification to a single counter-propagating pump configuration which is good enough for fiber lengths around 20 km. As we are not performing amplification on a monochromatic signal but on a multiple waves signal, it is necessary to verify that all the waves experience the same gain so that the all dynamic is equally compensated. This is illustrated with the spectra in Fig. 3.8. The spectrum of the noise floor Raman amplification is displayed in Fig. 3.8. (a) with a pump at $\lambda_R = 1450$ nm. We notice that the maximum gain is located 13.2 THz away from the pump, as we have seen in Chapter 1, close to the 1550 nm signal wavelength. A 1 THz span centered to the maximum gain frequency is displayed in Fig. 3.8. (b). The gain variation on the 1 THz span is about 0.6 dB. At the maximum compression points in FPUT recurrences, the comb broadening doesn't exceed 1 THz

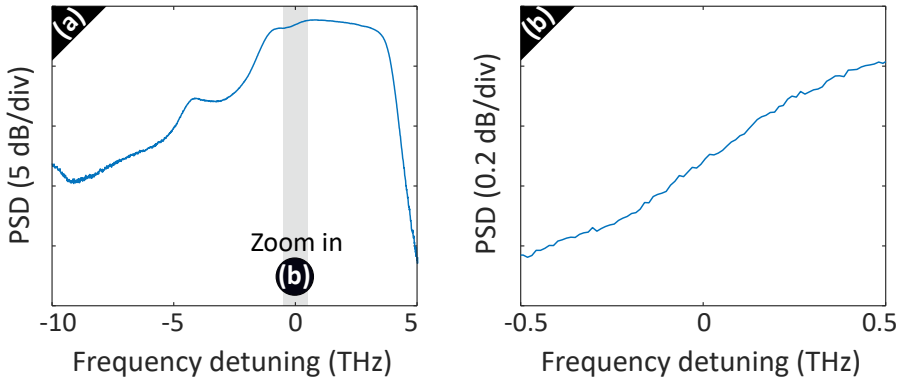

Figure 3.8: Experimental spontaneous Raman gain spectrum with (a) the original 15 THz span and (b) 1 THz span zoom centered around the CW background frequency. The steep decrease from 3 to 5 THz is due to the WDM 1450 nm rejection.

(corresponding to 12 sidebands on each side of the pump for $f_m = 40$ GHz), so we can consider that all the Fourier modes are compensated almost equally (and it is even better for the most important waves, the central ones). While the Raman gain is constant in the spectral domain, we also verified that the gain is constant all along the pulse duration. We checked that the pulses are short enough so that the Raman pump remains unsaturated. We investigated this feature in details in [53]. For a sake of clarity, these works are shown in Appendix B. They reveal that we can fairly consider an unsaturated Raman amplifier in a 20 km long fiber with 50 ns duration pulses. We also verified numerically that the pulse width can be increased up to 800 ns without significative Raman pump saturation effects (less than a 1% power variation of the amplified pulse). This is why the Raman compensation works quite well in our system and we can then consider an almost fully transparent fiber. To compensate more efficiently the losses in long fibers, it is possible to amplify the signal with optimized time shaped Raman pulses. To do so, we implemented a shaping stage of the Raman pulse, with another AWG synchronized with the rest of the setup and controlling an AO modulator (14). We investigated experimentally the benefit of a distributed control of the Raman gain, our results are presented in Appendix C. The Raman pump is injected in the fiber with a wavelength division multiplexer (WDM) at the fiber output to propagate backward. Another WDM is added at the fiber input to separate the Raman pump from the backscattered signal and to prevent any damage on the optical devices.

3.7 Stability of the setup

The stability of the experimental setup plays a key role in the reproducibility and the precision of the measurements. Indeed a lack of long-term stability would prevent from reproducible measurements and single parameter variation studies while a lack of short-term stability would impact averaging techniques. The latter can lead to blurring effects of the traces, as displayed in Fig. 3.9. We performed numerics of a FPUT dynamics over a

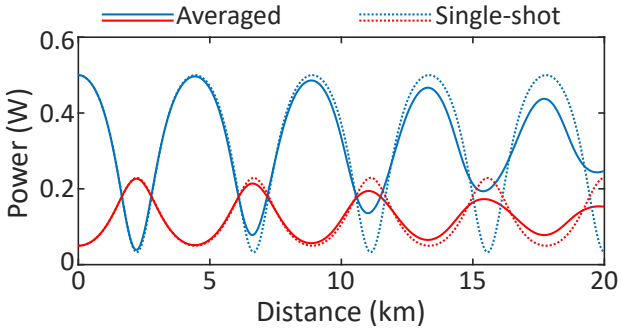

Figure 3.9: Power evolutions of the pump (blue lines) and the signal (red lines) along the fiber length. Solid lines: averaging of traces from 11 different values of $P_p(z = 0)$, from 450 to 550 mW. Dotted lines: single-shot traces for $P_p(z = 0) = 500$ mW.

20 km long optical fiber, with 11 distinct values of initial pump power $P_p(z = 0)$ linearly varying from 450 mW to 550 mW. We displayed the averaged pump (blue soid line) and signal (solid red line) powers evolutions along the fiber length and compared it with the single-shot case where $P_p(z = 0) = 500$ mW (dotted lines). It leads to a progressive lack of contrast of the longitudinal periodicity compared to the ideal case. The power minima are getting less and less weak while the power maxima less and less powerful as we propagate in the fiber. Indeed, the initial pump power influences the recurrence length and then the power extrema locations, that will be shifted from one single-shot to the other. To reduce such blurring effects, the measurements are performed in a restricted amount of time. The recordings, the post-processing steps (fading noise suppression, filtering) and the averaging (over a hundred of single-shot measurements) are fully automated and realized in less than a minute. To ensure that no major drift of the input power occurred, we record, before and after each acquisition, the spectrum from the noise-induced MI (phase modulator off) as an indicator of the input power. It allows to highlight possible power fluctuations either during an acquisition or between two acquisitions. To improve the stability of the excitation, we also modified all the optical fiber paths until the output of the AO modulator with polarization maintaining fibers

and components.

Chapter conclusions

In this chapter, we described in detail our fully fiber experimental setup, from the non-linear excitation shaping to the detection and the digital post-processing. We explained how we manage to perform very fast distributed measurements through an OTDR technique, coupled with phase measurements through multi-heterodyne detections. A particular consideration is given for the description of the active loss compensation scheme through backward Raman amplification as it represents an essential asset for the experimental studies that will be carried out.

Chapter 4

Demonstration of FPUT-predicting NLSE analytical solutions

Outline of the current chapter

4.1 The first-order doubly periodic solutions **54**
4.1.1 Solutions description 54
4.1.2 Three waves input approximation 56
4.1.3 Experimental results 58
B-type solutions 58
A-type solutions 59
4.2 Gain outside the conventional MI band **61**
4.2.1 Analytical feature 61
4.2.2 Experimental demonstration 63
Initial conditions 63
Results 63
Chapter conclusions **67**

We saw in the previous chapter that a very effective active compensation of the fiber losses is achieved thanks to a counter-propagating Raman pump, allowing to perform measurements in a quasi-transparent fiber. In the absence of losses, the equation that governs the system dynamic, in this case the NLSE, is integrable. It is then possible, with this setup, to directly observe and experimentally demonstrate analytical solutions from

the NLSE. In the case of breathers dynamics in optical fiber setups, theoretical solutions have already been observed like the Peregine soliton in [36] and the Akhmediev breather in [37]. However such specific solutions only account for a single growth and decay cycle. Then they do require only few L_{NL} propagation and are less sensitive to the fiber attenuation. Indeed the fiber lengths don't exceed the L_{NL} by 4 times in [36] and 5 times in [37]. In the case of FPUT recurrences, the breather repeats itself, as predicted by a more general description of breathers dynamics, the first-order doubly periodic solutions. They are observed over much more L_{NL} (fibers of 10 to 12 times the L_{NL} in our experiments) and require then an adequate fiber attenuation compensation. In a first section, we will describe and present our experimental results about this first observation of the doubly periodic solutions of the NLSE. A specific feature was also revealed from one type of these solutions, which is the instability of perturbations beyond the conventional gain band of MI. This "extraordinary" modulation instability gain is investigated and demonstrated with experimental results in a second section.

4.1 The first-order doubly periodic solutions

The AB solution of the NLSE, which describes the nonlinear stage of MI [37, 108, 125, 142, 143], turned out to be a good prototype for rogue waves description but also a good model for FPUT recurrences in cubic nonlinear media. However, as we have seen in Chapter 2, the AB only accounts for a single growth and decay cycle as the solution is periodic in time but localized in space, and doesn't allow to predict the formation of multiple recurrences, as observed in [34, 39–42, 44, 45, 106]. More general solutions have been found, characterized by repeated growth and decay cycles: the first-order doubly periodic solutions of the NLSE [51, 52].

4.1.1 Solutions description

General solutions from the NLSE, describing the observed recursive feature, have been found by Akhmediev *et al.* with the first-order doubly periodic solutions [51]. The solutions have been derived again and their Fourier coefficients have been calculated by Conforti *et al.* in [52]. The solitons on finite background (AB, PS, KM), presented in Chapter 2, are by the way particular cases of these solutions. In a desire of fluidity, the solutions expressions are detailed in Appendix A. They depend on only three parameters (α_1, α_2, α_3) and can be classified in two types, A or B, according to their phase shift between successive maximum compression points and so their location in the phase

portrait regarding the separatrix. This duality of solutions reveals the broken symmetry nature of the FPUT recurrences, as demonstrated in [42]. Either the consecutive maxima are in phase i.e. the phase space trajectory is an inner one and the solution is of B-type, or the consecutive maxima are π-shifted i.e. the phase space trajectory is an outer one and the solution is of A-type. An example of both types is displayed in Fig. 4.1, whose results are computed from the expressions in [52]. On the left panel

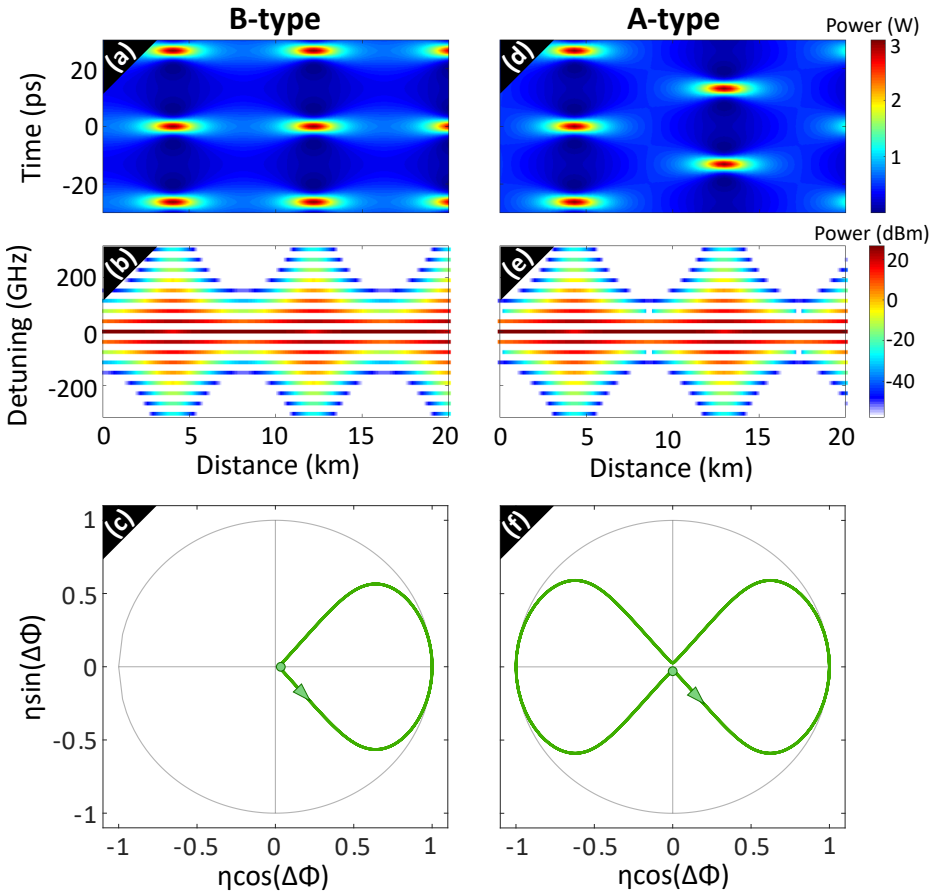

Figure 4.1: Calculated doubly periodic solutions of both B-type (left panel) and A-type (right panel) from [52], whose equations are reminded in Appendix A. (a), (d) Spatio-temporal evolutions of the power. (b), (e) Spatio-spectral evolutions of the power. (c), (f) Phase-plane $(\eta cos(\Delta\Phi), \eta sin(\Delta\Phi))$, with the green dots corresponding to the initial state.

is shown a B-type solution while on the right side a A-type. From the spatio-temporal evolution of the solutions in Fig. 4.1. (a) and (d), we notice a periodicity both in the time domain with pulse trains (more than two periods represented here) and in the spatial domain with repeated evolutions of the wave into these pulse trains (more than

two periods represented here). With the same doubly-periodicity, these solutions seem to be adequate to describe the FPUT recurrences dynamics. For the B-type solutions, the pulses from the maximum compression points always appear at the same temporal location, meaning that the recurrences are in-phase. The A-type solutions present pulses from two consecutive maximum compression points which are shifted by half a temporal period, meaning that the consecutive recurrences are π-shifted and also revealing the broken symmetry feature. In Fig. 4.1. (b) and (e), we show the corresponding spectral evolutions, which also highlight the periodicity along the propagation distance. For each case, the spectra broaden into a frequency comb trough multiple FWM processes, with a maximal broadening at the maximum compression locations. The associated trajectories in the phase-plane $(\eta cos(\Delta\Phi), \eta sin(\Delta\Phi))$, as presented in Chapter 2, are reported in Fig. 4.1. (c) and (f). For B-type solutions, two consecutive growth and decay cycles follow the same path in the right half-plane and the trajectory is then located in the separatrix (bounded by the AB). For A-type solutions, the trajectory is outside this separatrix and two consecutive cycles are then located in opposite half-planes, which highlights the π-shift.

4.1.2 Three waves input approximation

We know that the AB dynamics can easily be excited using a truncated three waves input spectrum (a pump and a signal/idler pair from the modulation) [37]. However, this imperfect excitation leads the system to exhibit a recursive dynamic of growth and decay cycles, as observed in [42, 109], and which are not predicted by AB theory. It is then important to look at the robustness of this truncated three waves excitation approximation to observe the doubly periodic solutions. The initial spectra of both doubly-periodic solutions are reported in Fig. 4.2. (a) and (b), calculated from [52] and the equations in Appendix A. While the B-type solution has a triangular-shaped frequency comb spectrum in $z = 0$, the A-type solutions contains only odd order sidebands (the even order sidebands amplitudes are strictly zero). For first-order sidebands (signal and idler) powers 20 dB lower than the zero order peak (pump) power, the third order sidebands powers are then 70 dB lower than the pump. The higher order sidebands are negligible in that case and it seems appropriate to approximate the input with only a three waves truncation (pump and signal/idler pair). In Fig. 4.2. (d), we displayed the first and second pump maximum locations for a A-type solution (dotted black lines) and NLSE numerics from a three waves input (solid red lines) as a function of the signal to pump ratio. The comparison between numerics and analytics is made possible as

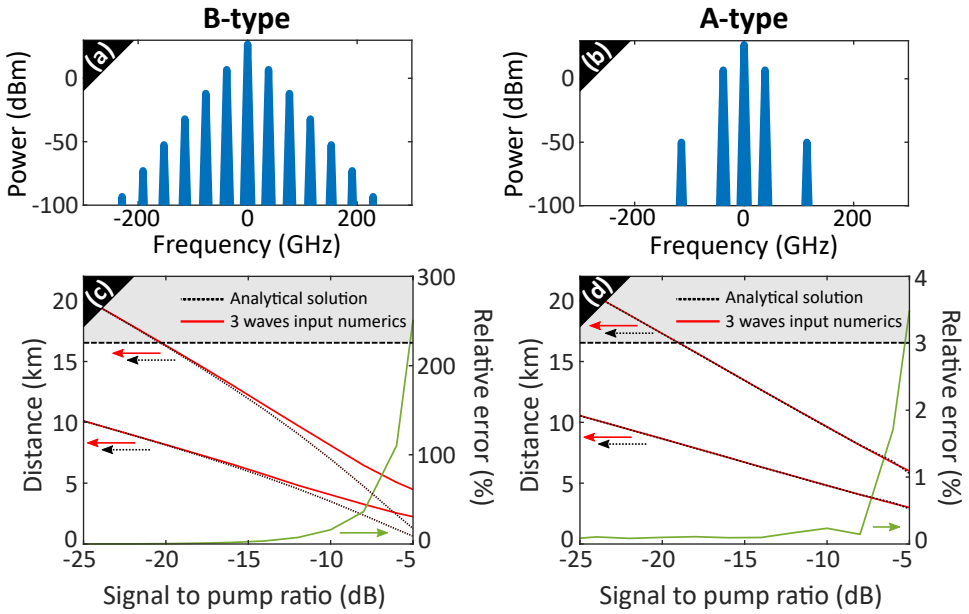

Figure 4.2: Spectra of the (a) B-type and (b) A-type solutions at the fiber input $z = 0$, calculated from the equations in Appendix A. (c), (d) First and second pump maxima locations as a function of the signal to pump ratio, for analytical solutions (dotted black lines) and three waves input numerics (solid red lines), and the corresponding relative error (solid green lines).

the parameters of the analytical solution are calculated by perfectly matching the three central waves of the input spectrum with the numerical truncated three waves input. Their respective pump maxima locations coincide very well, as revealed by the relative error between analytics and numerics (solid green line). It doesn't exceed a 0.2% gap until −10 dB and remains relatively low (up to 3%) at high modulation amplitudes. However, the second order sidebands for B-type solutions are not negligible a priori. From the pump maxima location in Fig. 4.2. (c), we notice that the gap increases with the signal to pump ratio. It remains below 1% until −20 dB but it increases exponentially after, up to few hundred % at high modulation amplitudes. Lower is the modulation, more accurate is the truncated three waves approximation, as a higher fraction of the total power remains confined in these three waves. However, a too weak modulation results in too long spatial periods, as seen in Fig. 4.2. (c) and (d). To highlight the broken symmetry feature of these solutions, it is necessary to record two full growth and decay cycles within the fiber length. With the achievable power ($P \sim 0.5$ W) and the fiber length limitation ($L = 16.54$ km, which is marked with dashed black lines in Fig. 4.2. (c) and (d)), the initial signal to pump ratio is set as a trade-off value to

−20 dB. From a truncated three waves input, both solution types are excited with a specific initial relative phase value. We know from [42] that an inner trajectory in the phase-plane (in phase recurrences) is obtained with an initial phase difference between the pump and the seed of $\Delta\Phi(z=0)=0$ and an outer one (phase-shifted recurrence) with $\Delta\Phi(z=0)=\pm\frac{\pi}{2}$. According to Fig. 4.1, a B-type solution can then be excited from a truncated three waves input with $\Delta\Phi(z=0)=0$ and a A-type with $\Delta\Phi(z=0)=\pm\frac{\pi}{2}$. The doubly-periodic solutions are characterized with only three arbitrary parameters, denoted α_1, α_2 and α_3, which are nonzero roots of a fourth-order polynomial. In our case, to compare the experimental data with a truncated three waves excitation with full-spectrum input analytics, these parameters are calculated numerically by matching in amplitude and phase, at the fiber input, the zero and first-order Fourier bands of the analytical solutions with the three waves.

4.1.3 Experimental results

The recordings are performed on a 16.54 km long SMF-28 optical fiber (G.652 standard), with $\beta_2=-19$ ps^{2}km^{-1} and $\gamma=1.3$ W^{-1}km^{-1}. The three waves are set with an input pump power $P_p(z=0)=480$ mW, signal and idler powers $P_s(z=0)=P_i(z=0)=4.8$ mW and a modulation frequency $f_m=38.2$ GHz (close to the MI peak gain frequency of 40.8 GHz).

B-type solutions

For B-type solutions demonstration, the initial relative phase is set to $\Delta\Phi(z=0)=0$ and the experimental data are presented in Fig. 4.3 (solid lines). The relative power evolutions of the pump (blue line) and the signal (red line) are displayed in Fig. 4.3. (a). The pump power decreases while the signal power increases and they reach a minimum and a maximum respectively at $z\sim 4.5$ km. At this stage, the signal is amplified by about 30 times from its input value. The power evolutions reverse back then to return to the initial state at $z\sim 8.5$ km and complete one growth and decay cycle. Another cycle is observed from $z=8.5$ km to $z=15$ km. The relative phase evolution is plotted in Fig. 4.3. (b) and is also periodic. We observe two cycles of phase which remain bounded within $\left[\frac{-\pi}{2},\frac{\pi}{2}\right]$. From the phase portrait representation in Fig. 4.3. (c), we notice that the trajectory remains in the right semi-plane for both cycles. These experimental results are compared to the zero and first-order Fourier bands of a B-type analytical solution (dotted lines). The solution three parameters, determined from the input truncated waves perfect matching, are $\alpha_1=0.426$, $\alpha_2=0.728$ and $\alpha_3=1.026$. The global agreement

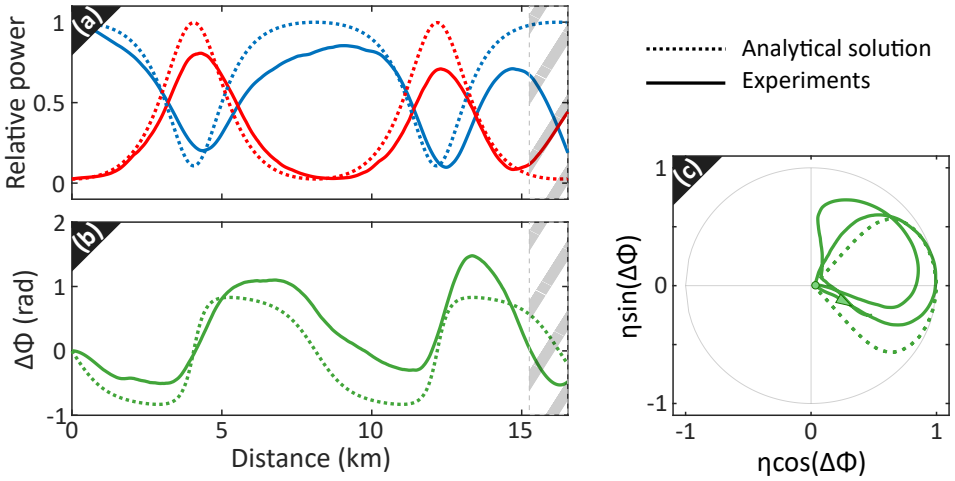

Figure 4.3: Spatial evolutions of (a) the pump (blue lines) and the signal (red lines) relative powers, (b) the relative phase. (c) Phase-plane representation, with the green dot corresponding to the input state. Solid lines correspond to the experimental data and dotted lines to the B-type first-order solution of the NLSE ($\alpha_1 = 0.426$, $\alpha_2 = 0.728$, $\alpha_3 = 1.026$). Each component is normalized with respect to the maximum value of the analytical solution. $\Delta\Phi(z = 0) = 0$.

of the experimental data with the analytical solution is very good. It is confirmed by the spatial period given by the solution three parameters which is 8.12 km. However, some discrepancies are observed, especially looking at the fiber end. Indeed, in case of a counter-propagating Raman pump, the fiber end region is always more amplified than the central part [73]. We decided to amplify beyond the optimal compensation along the full fiber length and to improve the compensation on a more restricted part of the fiber. A quasi-transparent fiber is then obtained along the first 15 km at the expense of an over-amplification in the last few kilometers. The nonlinear dynamic is accelerated there, leading to a gap from the theory. This hatched region (both in Fig.4.3 and 4.4) should then be omitted when comparing the experiments with the analytics. However the power maxima gap cannot be attributed to an imperfect loss compensation since a very good accordance is reached for the extrema locations. We rather assume that it is due to a blurring effect from the averaging over a high number of traces (see Chapter 2 for more details).

A-type solutions

To excite a A-type solution, the initial relative phase is set to $\Delta\Phi(z = 0) = -\frac{\pi}{2}$. The corresponding experimental data are reported in Fig. 4.4 (solid lines). The power

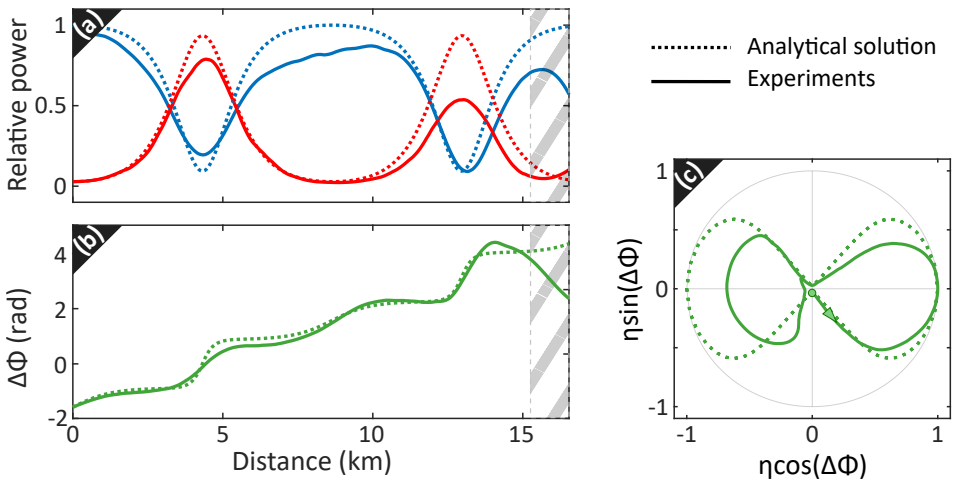

Figure 4.4: Same as in Fig. 4.3 but for $\Delta\Phi(z=0) = -\frac{\pi}{2}$ (A-type solution with $\rho = 0.565$, $\eta = 0.129$ and $\alpha_3 = 0.980$).

evolution of the pump (blue line) and the signal (red line) in Fig. 4.4. (a) are similar to those of the B-type solution, except for the first and second pump minima and signal maxima which are reached for $z = 4.4$ km and $z = 13.1$ km respectively. The relative phase evolution in Fig. 4.4. (b) is rather different and increases monotonically from $-\frac{\pi}{2}$ to almost $\frac{3\pi}{2}$ at the end of the second growth and decay cycle. The dynamic of both cycles is identical except for the phase of the second cycle which is π-shifted from the first one. The trajectory in the phase-plane is shown in Fig. 4.4. (c). The first cycle occurs in the right half-plane while the second one does in the left half-plane, revealing the pulses shift for consecutive maximum compression points. These experimental results are also compared to the zero and first-order Fourier bands of a A-type analytical solution (dotted lines), whose parameters are $\alpha_{1,2} = \rho \pm i\eta$, with $\rho = 0.565$ and $\eta = 0.129$, and $\alpha_3 = 0.980$. The agreement between the analytical solution and the experimental data is very good, especially considering the growth and decay cycles period. Indeed, the half analytical spatial period (the full period corresponding also to the return to the initial phase) is 8.64 km, corresponding to less than a 1% gap with the experimental value.

These results, which demonstrates for the first time the first-order doubly periodic solutions of the NLSE of both types, are published in [46]. As we performed measurements by recording only the three central waves evolution, we assume that more complex breathing dynamics may be observed, as higher order rogue waves [144, 145] and higher order MI [146–150], by increasing the number of recorded waves, as it has

already been done in [45].

4.2 Gain outside the conventional MI band

The frequency band for which the doubly-periodic solutions exist is delimited by MI. However, while the limiting case for B-type solutions is the standard MI, obtained from the linear stability analysis (see Chapter 2), the limiting case for A-type solutions is more general, beyond the conventional MI band [52].

4.2.1 Analytical feature

When the parameters of the solution are found with $0 < \rho < 1$ and $\eta \to 0$, it corresponds then to the growth of weak periodic perturbation on a CW background. The exact conditions of MI are fulfilled, as described in the linear stability analysis, and the solutions are then found for $\omega \in [0, 2]$, the standard normalized gain band of MI. However, with ρ and η beyond this range, it exists solutions with a perturbation beyond the MI gain band ($\omega > 2$) that grows with all the features of MI. The gain bands corresponding to the amplification of a periodic perturbation and calculated from the analytical doubly periodic solutions are reported in Fig. 4.5. (a). The dotted lines represent the gain bands

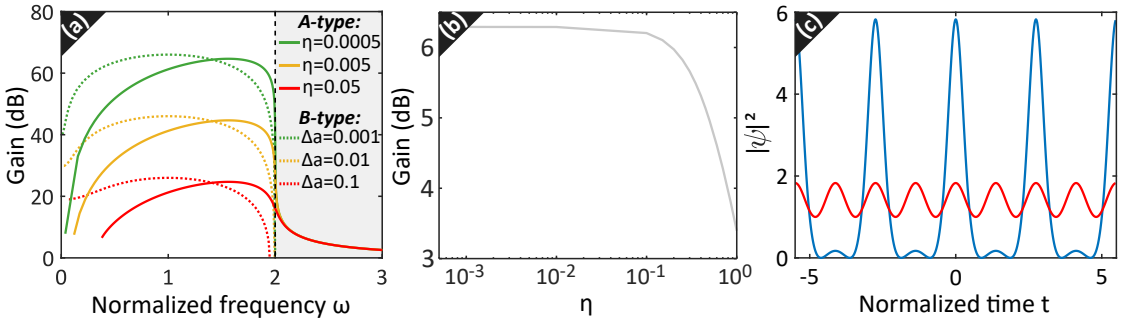

Figure 4.5: (a) Gain band profiles of a periodic component for A-type solutions (solid lines) and B-type solutions (dotted lines), calculated from the equations in Appendix A. The frequency ω is varied through the parameter ρ that changes within $[-3, 1]$. The grey area is the range $\omega > 2$, beyond the standard MI band. (b) Evolution of the gain at $\omega_m = 2.287$ as a function of η. (c) An initial weak periodic modulation, with a frequency $\omega_m = 2.287 > 2$, on a CW background (solid red line) and its profile at the maximum compression (solid blue line). The parameters of the solution are $\rho = 0$, $\eta = 1$ and $\alpha_3 = 1$. (a), (c) Adapted from [52].

from B-type solutions and the solid lines from A-type solutions. Whatever the solution type is, we notice the presence of gain within the band $\omega \in [0, 2]$, which is expected from

the standard MI. Looking beyond, for $\omega > 2$, the gain for B-type solutions is zero, as expected from the MI linear stability analysis but is not zero for A-type. The amplification is lower than for standard MI but remains significant, especially close to the standard cutoff frequency $\omega_c = 2$, progressively vanishing at higher frequencies. While the gain depends on the value of the parameter η (related to the perturbation amplitude) within the standard band and is lower at higher η, the gain outside this band doesn't seem to depend on η. We report the evolution of the gain at a fixed frequency $\omega_m = 2.287$ as a function of η in Fig. 4.5. (b). Indeed the gain remains almost constant at low η until 0.1 but it decreases after, as the "extraordinary" MI gain always remains lower than the standard MI gain. In Fig. 4.5. (b) is plotted the intensity profiles of the A-type solution with a perturbation frequency outside the MI conventional band of $\omega_m = 2.287$. From the lowest modulation amplitude (solid red line), the perturbation grows on the CW background, similarly as in Fig. 4.1, until it reaches the maximum compression (solid blue line). We also notice another feature from A-type doubly periodic solutions. From the initial modulation, only one out of two maxima grow and the other decay, leading to the period doubling of the initial frequency. An explanation for the presence of gain outside the conventional MI band only in A-type solutions can be found by looking at the nonlinear deformation of linear solutions [52]. We consider the initial three waves input:

$$\psi(z = 0, t) = \psi_{p,0} + \psi_{s,0}(e^{i\omega_m t} + e^{-i\omega_m t}) \tag{4.1}$$

If this wave propagates in a linear fiber i.e. according to the NLSE in Eq. 2.12 but without the Kerr effect, the linear solution is easily found as:

$$\psi(z, t) = \psi_{p,0} + \psi_{s,0}(e^{i\omega_m t} + e^{-i\omega_m t})e^{-i\frac{\omega_m^2}{2}z} \tag{4.2}$$

During the propagation, the phase of the linear solution is rotating and alternates between amplitude (0 and π) and phase ($\frac{\pi}{2}$ and $-\frac{\pi}{2}$) modulation states, as exhibited by the A-type solutions behavior. Moreover we notice that a π-phase shift, from the propagation of an amplitude modulation state to the next, induces a temporal shift of half a period in intensity, as observed with A-type solutions. This linear phase shift exists whatever the modulation frequency is ($\omega_m > 2$ is possible). A-type solutions can then be seen as the nonlinear dressing of these linear solutions. The gain band $\omega_m \in [0, 2]$ appears then with the MI, in the presence of the Kerr effect, while the gain for $\omega_m > 2$ is the smooth transition to the validity band of the linear solution. On their side, B-type solutions have a purely nonlinear origin associated to the phase-space deformation

induced by this nonlinearity, that can't be compared to any linear solution. Another explanation can be formulated looking at the phase portraits from the Hamiltonian approach of the 3WM process in Fig. 2.9. (a). We notice that the limit case of outer trajectories (excited with A-type solutions) is the external circular trajectory, with a constant modulation amplitude but a rotating phase, corresponding then to the linear solution from Eq. 4.2. Conversely, the limit cases of inner trajectories (excited with B-type solutions) are the stable points C_0 and C_π (from the Hamiltonian approach of the three waves model in Chapter 2), with the amplitude and the phase of the modulation both constant.

4.2.2 Experimental demonstration

Initial conditions

As for the demonstration of the doubly periodic solutions presented earlier in this chapter, the solutions are experimentally excited with a truncated three waves input. The gain outside the standard MI band being observed for A-type solutions, the truncation is very accurate in this case, as discussed in the previous section. The gain outside the band is constant with η, so to benefit of sufficiently high power conversions, it is necessary to have a relatively high modulation power. The intensity of the signal/idler pair is then set 5.3 dB below the pump power. The study is performed in a $L = 18.28$ km long single mode fiber, with the G.652 standard ($\beta_2 = -21$ ps^{2}km^{-1} and $\gamma = 1.3$ W^{-1}km^{-1}) and the pump power is set to $P_p = 180$ mW. It results in a MI cutoff frequency, from Eq. 2.8, at $f_c = 33.6$ GHz. For all the experiments, we set the modulation frequency so that $f_m > f_c$. The experimental spectra of the truncated three waves input and the spontaneous noise floor MI amplification (revealing the conventional gain band) are reported in Fig. 4.6. We clearly notice that, in this case where $f_m = 40$ GHz, the signal/idler pair (sidebands from the solid purple line) is located beyond the cutoff frequency of the MI sidelobes (dotted yellow line). As it has been done in the previous section, the initial relative phase is set to $\Delta\Phi(z = 0) = -\frac{\pi}{2}$ to excite a A-type dynamic.

Results

For a modulation frequency $f_m = 40$ GHz, the experimental data (solid lines) and the corresponding analytical A-type solution (dotted lines), with a perfect matching of the three central waves, are displayed in Fig. 4.7. The evolution of the pump (blue lines) and signal (red lines) powers along the fiber length are plotted in Fig. 4.7. (a). Similarly to the results in the previous section, we observe multiple growth and decay cycles, up to

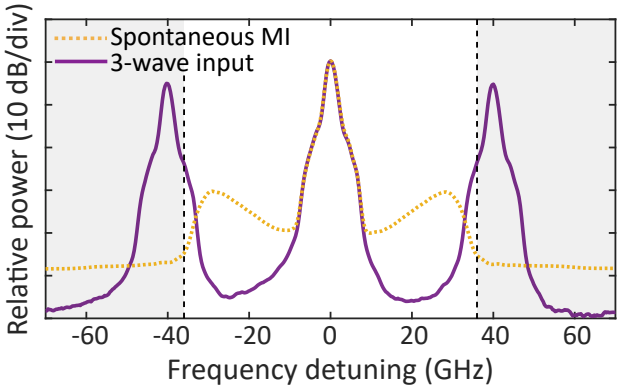

Figure 4.6: Experimental spectra of the truncated three waves input (solid purple line) and noise-induced MI (dotted yellow line). The two vertical dashed black lines correspond to the cutoff frequencies $\{-f_c, f_c\}$ and set the limits of the conventional MI gain band. The grey areas are the bands beyond.

almost four here. In the first cycle, the signal is amplified and the pump depleted until $z = 2.5$ km, the process reverses and returns to the initial state at $z = 5$ km. Regarding the recurrence period, the agreement is very good as the analytical half spatial period is 4.94 km. At the first maximum compression point in experiments, the signal is amplified by 1.7 dB from its initial value, while in theory by 2.8 dB. As explained in the previous section, the disagreement of power maxima cannot be attributed to an imperfect loss compensation as a very good accordance is obtained for the maxima locations. In Fig. 4.7. (b), we plotted the relative phase $\Delta\Phi$ evolution. Despite the dominant linear term, we notice a periodic modulation of the phase and the evolution fits very well to analytics. As observed for A-type solutions in the previous section, two consecutive growth and decay cycles present a π relative phase-shift and the initial relative is then recovered after two cycles, at $z = 10$ km. The trajectory in the phase-plane $(\eta cos(\Delta\Phi), \eta sin(\Delta\Phi))$ is portrayed in Fig. 4.7. (c). The dynamic oscillates between both half-planes and reveals an outer trajectory, as expected from A-type solutions. The Fig. 4.7. (d) and (f) show the space-time evolutions of the power and phase respectively, calculated with the inverse Fourier transform of the three central waves evolution (in Fig. 4.7. (a) and (b)), as it has previously been done in [45]. We obtain breather patterns, confirming a modulation instability regime, with the expected half a temporal period shift of the high power pulses between two consecutive maximum compression points. The agreement with the analytical profiles in Fig. 4.7. (e) and (g) is very good as the reconstruction of the temporal dynamic with the inverse Fourier transform is very effective. Indeed, the large majority of the total power remains contained within the three central waves. From the

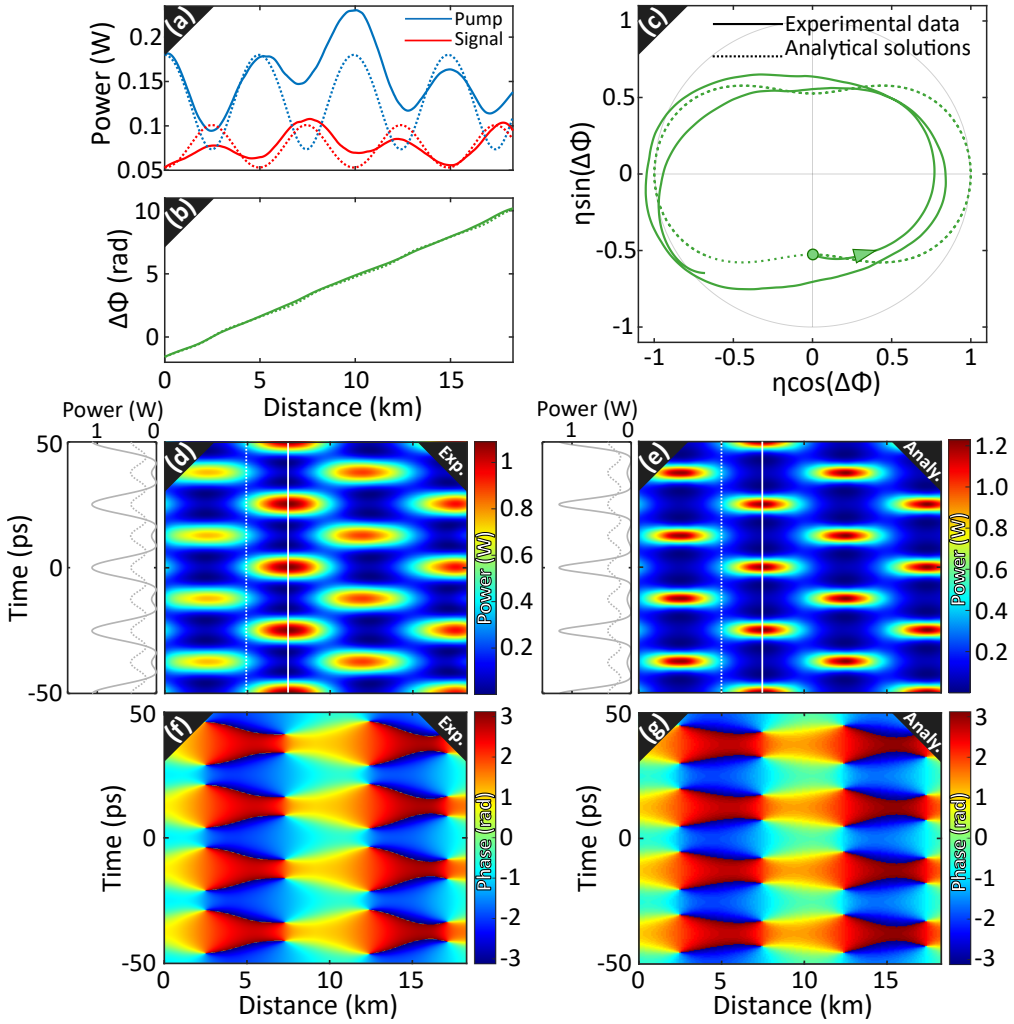

Figure 4.7: Evolutions of (a) the pump (blue lines) and signal (red lines) powers, and (b) the relative phase along the fiber length. (c) Trajectory in the phase-plane $(\eta cos(\Delta\Phi), \eta sin(\Delta\Phi))$, with the green dot corresponding to the input state. Experimental data are plotted in solid lines, while the corresponding analytical solution in dashed lines. Experimental (calculated by the inverse Fourier transform of the data in (a) and (b)) and analytical space-time false-color profiles of (d), (e) the power and (f), (g) the phase. Aside of the power plots are sectional views at minimum (dotted lines) and maximum (solid lines) compression points. The modulation frequency is $f_m = 40$ GHz ($\omega_m = 2.381$) and the parameters of the analytical solution are $\eta = 1.242$, $\rho = 0.0317$ and $\alpha_3 = 1.0$.

sectional views of the power, we get the time profiles at the minimum (dotted lines) and maximum (solid lines) compression points. It confirms the very good accordance, even

if the pulses at the maximum compression point are wider for the experiments due to the spectrum truncation. The evolutions of the longitudinal period and the gain are experimentally studied (orange crosses) as a function of the modulation frequency f_m, with $f_m > f_c$, in Fig. 4.8. (a) and (b). We notice that lower is the modulation frequency,

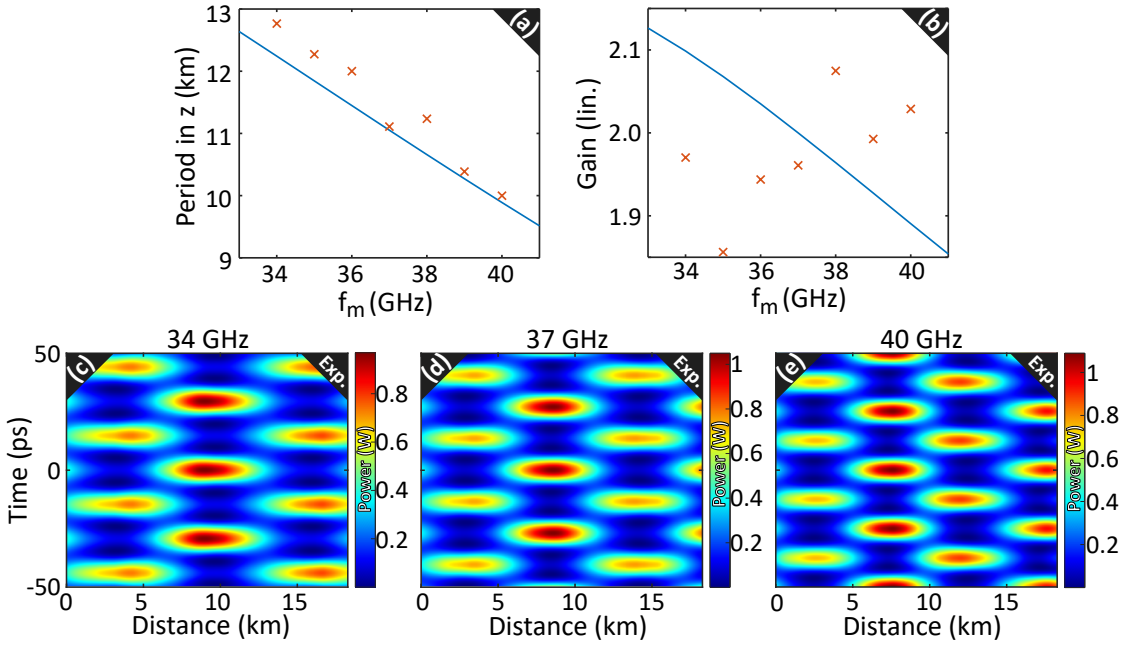

Figure 4.8: Evolutions according to f_m of (a) the spatial period and (b) the gain. Experimental data are displayed in oranges crosses and analytical ones in solid blue lines. Experimental space-time evolutions of the power for (c) $f_m = 34$ GHz ($\omega_m = 2.024$), (d) $f_m = 37$ GHz ($\omega_m = 2.202$) and $f_m = 40$ GHz ($\omega_m = 2.381$).

longer is the spatial period, as it decreases from 12.8 km at $f_m = 34$ GHz to 10 km at $f_m = 40$ GHz. It is in very good agreement with the analytical evolution (solid blue line). From the gain data, we cannot deduce any clear evolution, while the analytical solutions predict a slight decrease, of around 10% between $f_m = 34$ GHz and $f_m = 40$ GHz. The corresponding reconstructed experimental space-time power profiles are plotted in Fig. 4.8. (c), (d) and (e) for $f_m = 34$, 37 and 40 GHz respectively.

The experimental results presented here are a convincing demonstration of the existence of MI beyond the conventional instability band, predicted by the linear stability analysis. These optical results are published in [47], where water waves experiments are also performed in collaboration with Amin Chabchoub from the University of Sidney. Similar dynamics are observed and also very convincing results are obtained in hydrodynamics, displayed in Fig. 4.9. The simultaneous demonstration of this

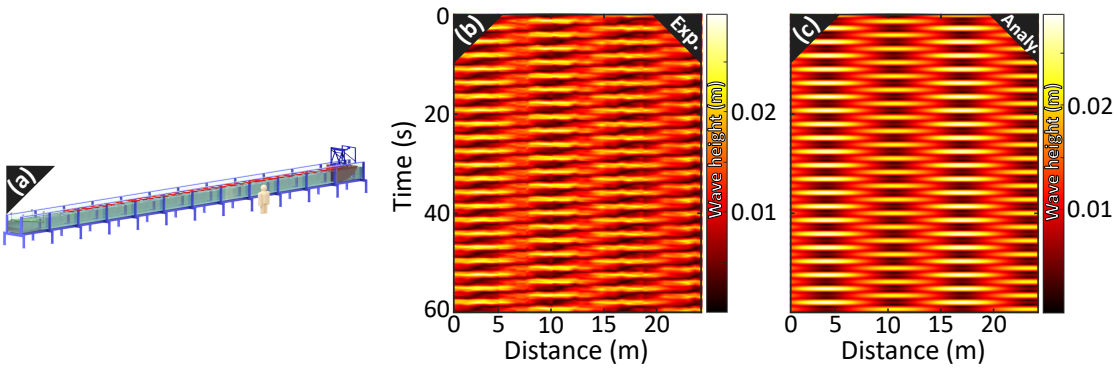

Figure 4.9: (a) Sketch of the water tank at the University of Sidney. (b), (c) Space-time evolutions of the wave height in experiments and analytics ($\eta = 1.9$, $\rho = -0.9$, $\alpha_3 = 1.0$) respectively. The modulation frequency $f_m = 0.37$ Hz is well beyond the MI cut-off $f_c = 0.22$ Hz.

feature in two different fields, which such different time and space scales, allows to strongly validate the results and highlight the interdisciplinary of MI. We expect then similar phenomena to be observed in plasmas [151, 152] or in Bose-Einstein condensates [153–155]. Whereas the physical phenomenon behind this unexpected gain remains misunderstood, here are some clues to find a beginning of answer. While the MI linear stability analysis is calculated for a single wave and is strictly valid considering an infinitesimal modulation ($\eta \to 0$), the gain outside the standard band only makes sense for $\eta \neq 0$. Then, multiple waves are considered here when studying the modulation instability band. A first step response would be to do the analogy with FWM processes in optical fibers, and especially with MI from multiple FWM as it has been studied from a dual-frequency pump in [156, 157]. Regarding the exclusivity of this feature for A-type solutions, it may be wise to look at the phase sensitivity of FWM frequency conversion as it has been done in [158]. Indeed, we saw previously the initial phase dependence for the solutions excitation and therefore, we can assume the process to be more favorable to "extraordinary" MI with a A-type solutions input phase configuration.

Chapter conclusions

In this chapter, we were able to demonstrate general solutions of the NLSE which predict the appearance of doubly periodic breather structures. It was made possible by obtaining a quasi-transparent optical fiber and so an almost integrable system. We demonstrated the capabilities of the setup as a powerful tool to observe analytical solutions of the NLSE, especially when a propagation on many nonlinear lengths is required. We first

demonstrated with a great concordance the first-order doubly periodic solutions of the NLSE, the only solutions which account for the periodicity in both space and time as observed in FPUT recurrences. Then, we provided an experimental proof of an "extraordinary" MI gain, not predicted by the linear stability analysis but revealed by the derivation of these solutions.

Chapter 5

FPUT recurrences in long fibers and route to the thermalization

Outline of the current chapter

5.1 Multiple FPUT recurrences recording **70**
5.1.1 Initial conditions 70
5.1.2 Results for phase-shifted recurrences 72
5.1.3 Results for in-phase recurrences 74
5.2 FPUT recurrences thermalization in optical fibers **75**
5.2.1 Noise-driven thermalization dynamic 76
5.2.2 Experimental results 79
Chapter conclusions **83**

We saw in the previous chapter that the efficiency of the loss compensation scheme allows to perform measurements in quasi conservative systems and then to excite analytical solutions of the NLSE. It also allows to study nonlinear dynamics in longer fibers, and thus on more nonlinear lengths than usual. Indeed, we recover the dynamic over 10 to 13 nonlinear lengths while it doesn't exceed 5.5 in [43–45]. In the context of FPUT recurrences phenomenon, one major issue is to observe the transition from a perfectly periodic regime to a thermalized state, as firstly expected by Fermi, Pasta, Ulam and Tsingou. In oscillator mechanics, this equipartition of the energy between eigenmodes is expected to occur after very long times [81–84]. By analogy, in fiber optics, we call

thermalization the evolution towards the distribution of the energy among the whole spectrum, in the Fourier modes as well as in the noise modes [159]. However, in that case the recurrences break-up, induced by the MI amplification of the noise, is expected to appear relatively quickly. A prerequisite for this study is to extend the observation of FPUT to several number of recurrences. In a first section we will demonstrate that this prerequisite is satisfied by reporting the observation of a high number of FPUT recurrences of both types (regular and shifted). In a second section we will study the noise-driven thermalization of the recurrences, with the controlled transition from a highly coherent periodic fashion to an irreversible incoherent thermalized state.

5.1 Multiple FPUT recurrences recording

While the fiber attenuation have been a critical issue to observe more than one single FPUT recurrence in many fiber optics systems [34, 37, 40, 41, 107, 108], an active compensation of the losses [42] or the use of a recirculating fiber loop [109] allowed to record up to two cycles. The observation of more than a single recurrence was a major advance since it allowed, on one side, to observe the symmetry breaking nature of the FPUT phenomenon and, on the other side, to highlight the invariance of the spectrum in the inverse scattering formalism. However, the study of FPUT thermalization in a MI-driven system requires the observation of a higher number of spatial periods within the fiber length [159]. In addition, our aim is to report the distinct observation of several cycles for both types of recurrences (in-phase and shifted) as a strong evidence of a highly reversible and quasi conservative system.

5.1.1 Initial conditions

The original experiments reported in [42, 44, 45] or in the previous section [46, 47] used a SMF-28 fiber or similar fibers with the G.652 standard. Even if the attenuation was relatively low with α(@1550 nm) = 0.2 dB/km and actively compensated by a Raman pump, it was detrimental to record more than two recurrences, especially for in-phase recurrences which are very sensitive to the losses (see more in details in Chapter 6). The experimental setup had to be improved to generate and observe more recurrences. In addition to a pre-amplification stage to increase the SNR and the optimization of Raman amplification scheme which were previously detailed in Chapter 3, we used for this demonstration an ultra-low loss (ULL) optical fiber. The fiber used was a 18.35 km long Corning Vascade EX2000, with a very low attenuation coefficient at 1550 nm

of $\alpha = 0.147$ dB/km, which is close to the record of $\alpha = 0.1419$ dB/km obtained in [57]. The benefit of such a fiber, compared to a G.652 fiber, is illustrated thanks to numerical simulations in Fig. 5.1. In Fig. 5.1. (a), we plotted, as a function of the signal

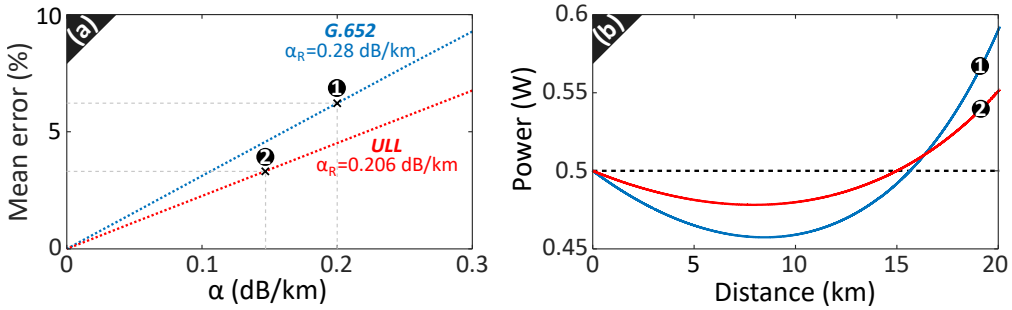

Figure 5.1: (a) Numerical calculations of the Raman compensation mean error as a function of the 1550 nm signal attenuation α for a 1450 nm Raman pump attenuation $\alpha_R = 0.28$ dB/km (dotted blue line) and $\alpha_R = 0.206$ dB/km (dotted red line). Optimized compensation power profiles for: a G.652 fiber, $\alpha = 0.2$ dB/km and $\alpha_R = 0.28$ dB/km (solid blue line); a ULL fiber, $\alpha = 0.147$ dB/km and $\alpha_R = 0.206$ dB/km (solid red line).

attenuation factor α, the mean error between the power profiles from the propagation in a fully transparent fiber and an optimized compensation with backward Raman pumping (mean gap between the dashed line and the colored lines in Fig. 5.1. (b)). It is calculated for two distinct Raman pump attenuation factors α_R (attenuation at 1450 nm), the one of the G.652 fiber $\alpha_R = 0.28$ dB/km (dotted red line) and the one of the ULL fiber $\alpha_R = 0.206$ dB/km (dotted blue line). We first notice that the error decreases linearly with α (in dB/km). As the intrinsic losses are lower, we reduce the mean error by 26.5% by using the ULL fiber considering only the impact of α. Then, it also allows to get a more efficient loss compensation since the Raman pump is also less attenuated and the mean error is reduced by 27% by using a ULL fiber, only considering the impact of α_R. Considering both, the mean error is reduced by 47% from ① to ②. The corresponding optimized compensated power profiles are displayed in Fig. 5.1. (b). The power evolution in the ULL fiber (solid red line) exhibits much less fluctuations around the input value than the evolution in the G.652 fiber (solid blue line). We estimate the gap with a fully transparent fiber to be reduced by a factor of 2, in accordance with the previous calculation. The other propagation parameters of this ULL fiber are a GVD coefficient $\beta_2 = -24$ ps^{2}km^{-1} and a nonlinear coefficient $\gamma = 0.77$ W^{-1}km^{-1}. This fiber has a lower nonlinear coefficient than a SMF-28 fiber, and so higher pump powers are required to get similar nonlinear length values to [42]. The initial pump power is then set to $P_p(z = 0) = 840$ mW, leading to a phase-matching frequency, according to Eq. 2.10,

of $f_0 = 37$ GHz. The modulation frequency is set close to this value, at $f_m = 34$ GHz, so that the signal/idler pair of the three waves input almost benefits from the maximum MI gain. The modulation amplitude is also managed, so that the sideband pair is 10 dB below the pump wave i.e. $P_s(z=0) = P_i(z=0) = 84$ mW. The modulation amplitude is adjusted low enough (compared to the CW background) to excite highly periodic solutions, close to the first-order doubly periodic solutions, and high enough to generate a sufficient number of recurrences within the fiber length. The three waves input will then experience a propagation along almost 12 nonlinear lengths ($L_{NL} = 1.55$ km) in a quasi conservative system. As for the demonstration of the doubly-periodic solutions in the Chapter 4, both recurrences regimes are excited with a precise control of the initial relative phase.

5.1.2 Results for phase-shifted recurrences

We know from [42, 116] the range of initial relative phase between the three waves required to excite the regime of phase-shifted recurrences. Then, we set it to $\Delta\Phi(z = 0) = -\frac{\pi}{2}$. The results in power and phase are summed up in Fig. 5.2. In Fig. 5.2. (a) we

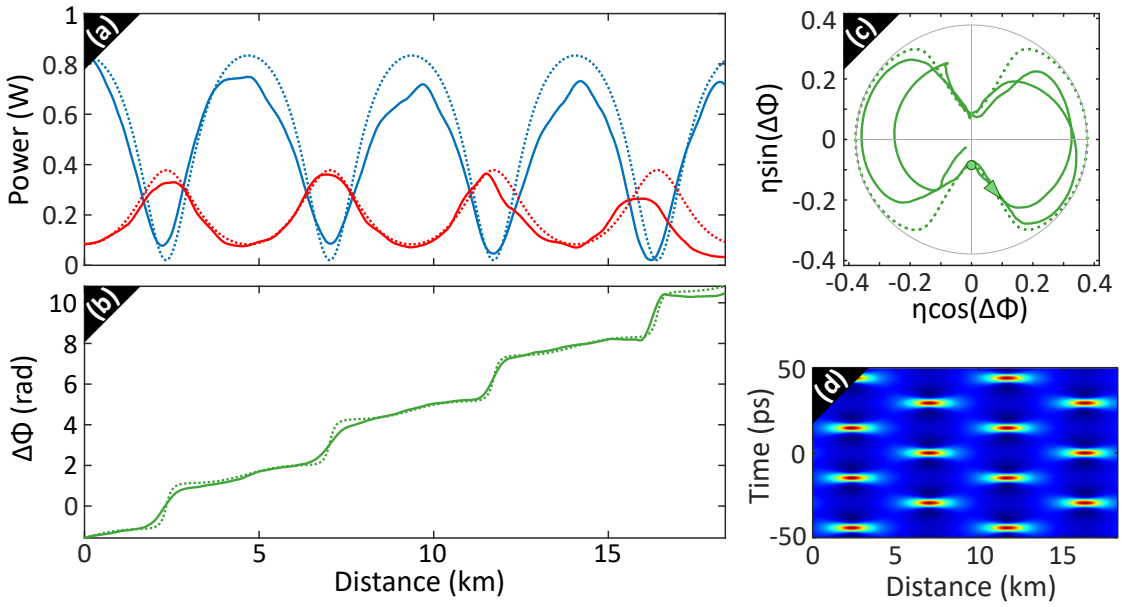

Figure 5.2: Evolutions along the fiber length of (a) the pump (blue lines) and the signal (red lines) powers, (b) the relative phase. (c) Representation in the phase-plane $(\eta cos(\Delta\Phi), \eta sin(\Delta\Phi))$. Solid lines correspond to the experimental data and dotted lines to numerical results integrated from the NLSE. (d) Numerics of the spatio-temporal evolution of the system. $\Delta\Phi(z = 0) = -\frac{\pi}{2}$.

displayed the experimental power evolution along the fiber length of the main three waves, with the pump (solid blue line) and the signal/idler (solid red line). Similarly to what we have seen in Chapter 4, the signal and idler waves are amplified at the expense of the pump wave at the early stage of the propagation. They reach a maximum and minimum respectively, corresponding to the maximum saturation point, at $z = 2.4$ km. It is then followed by an inversion of the energy flows and a return to the initial state of a powerful pump and a weak signal/idler pair at about $z = 4.5$ km. This process reproduces three more times during the rest of the propagation, resulting in the formation of four growth and decay cycles along the fiber length. These experimental results are compared to numerical results (dotted lines), obtained by integrating the NLSE from Eq. 1.10 with the exact same initial conditions as in experiments. We notice that the agreement concerning the location of the power extrema is very good. However, there is a small gap that progressively appears regarding the amplitude envelopes. In experiments, the values of the pump power maxima slightly decrease from 0.84 W at the first maximum to 0.73 W at the fourth maximum, while in numerics it remains constant. As mentioned in Chapter 4, such discrepancies can't be attributed to an imperfect compensation of the losses since the agreement for the amplitude extrema locations is very satisfying. We rather suppose that it is due to a blurring effect from the averaging over a high number of traces (see Chapter 3 for more details). At the end of the fiber, the gap with numerics can also be explained by the progressive coherence loss of seeded MI at the expense of spontaneous MI. A fraction of the Fourier modes energy has irreversibly been transferred to the noise. It will be studied more deeply later in this chapter. The evolution of the relative phase is plotted in Fig. 5.2. (b). The relative phase increases quasi-linearly during the propagation, but with faster variations around the maximum compression point. We also notice that two consecutive growth and decay cycles follow the same phase evolution but with a global π-shift. It means that the system returns to its initial state, both in power and phase, only after two cycles. The agreement with numerics is also very convincing here. The system dynamic is represented in a phase-plane with Fig. 5.2. (c). The trajectory oscillates from one half-plane to the other at each growth and decay cycle, which means that two consecutive cycles are π-shifted and that the even and odd cycles are respectively in phase. According to the Hamiltonian approach of the truncated 3WM model, detailed in Chapter 2, the system follows a trajectory which is outside the separatrix, as expected from this initial phase value [42]. The corresponding space-time profile, obtained from numerical calculations, is reported in Fig. 5.2. (d). It reveals the shift by half a time period from the high amplitude pulse trains at two consecutive maximum compression

points, equivalent to the π-shift of the relative phase.

5.1.3 Results for in-phase recurrences

To observe regular (in-phase) recurrences, we set the initial relative phase to $\Delta\Phi(z=0) = 0$ but all other parameters remain the same as in the previous case. The corresponding experimental results are shown in Fig. 5.3. From the power evolution of pump and

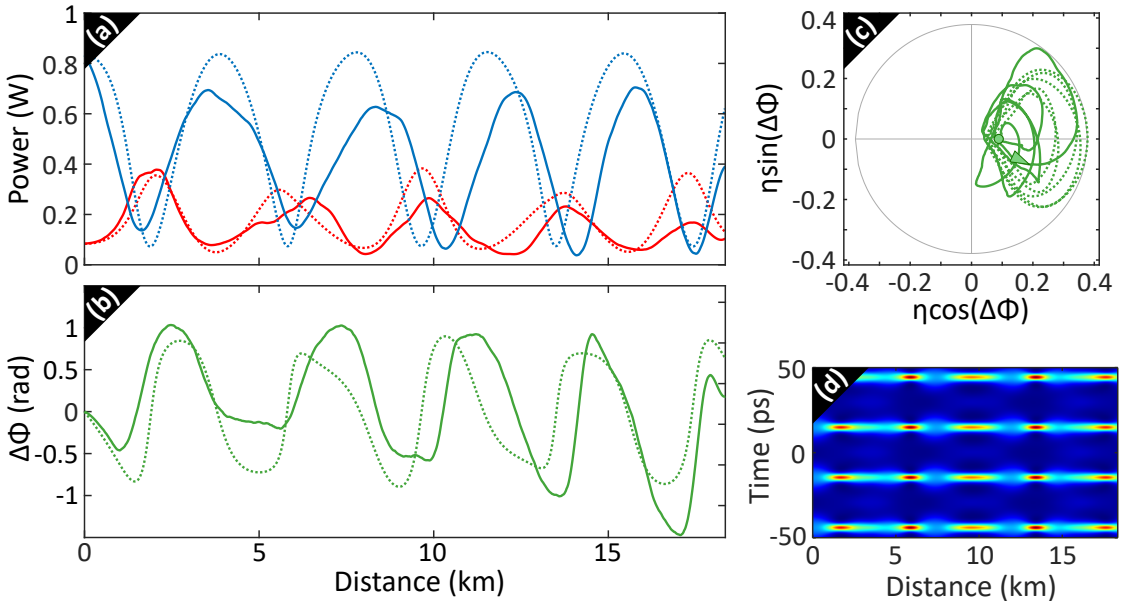

Figure 5.3: Same as in Fig. 5.2 but with $\Delta\Phi(z=0) = 0$.

signal waves in Fig. 5.3. (a), we observe nearly five growth and decay cycles, which is almost one more than in the previous case within the same fiber length. Looking at the relative phase evolution in Fig. 5.3. (b), we notice it remains bounded in $\left[-\frac{\pi}{2}, \frac{\pi}{2}\right]$. In this case, the relative phase of the system returns to the initial value 0 after each growth and decay cycle and follows the same evolution for each cycle. The growth and decay stages are discernible from the sign of the relative phase, which is negative and positive respectively. The dynamic is summed up with the phase portrait in Fig. 5.3. (c). Due to the boundedness of the phase, the trajectory remains confined in the right half-plane at each recurrence (trajectory inside the separatrix), as expected with this input relative phase value [42]. The unshifted FPUT recurrences allow to better judge the quality of the loss compensation scheme as the dissipation can modify the recurrences nature and force the symmetry breaking [39, 160]. The influence of dissipation on in-phase recurrences is studied and presented in Chapter 6. The fact that all the recurrences remain in phase all

along the propagation length confirms that the system is almost perfectly conservative and that the Raman compensation scheme is efficient enough. However, the system remains imperfectly loss compensated as we observe fluctuations of the total power along the propagation, as predicted by the numerics in Fig. 5.1. (b). These fluctuations are responsible for disturbing the dynamic and especially the longitudinal periodicity as we notice for example an almost 1 km gap of the third pump power minimum between experiments and numerics. The numerical spatio-temporal profile is reported in Fig. 5.3. (d) and it exhibits unshifted high power pulse trains. However, conversely to the shifted recurrences case, the dynamic is not identical for each recurrence, leading for example to amplitude gaps of the pulses at the maximum compression points. This is related to the fact that the excitation of perfectly periodic in-phase FPUT recurrences with a truncated three waves input is less robust and more sensitive to initial conditions perturbations. We saw through Chapter 4 that A-type doubly-periodic solutions (shifted recurrences) can be excited even with a high modulation amplitude three waves truncation, while a high modulation is detrimental for B-type solutions (regular recurrences) [46]. In the latter, perfectly periodic evolutions are observed only for sufficiently weak modulations and deviations from these perfectly periodic evolutions are then observed (signal/idler pair power is initially 10 dB below the pump power). The system rather follows a quasi-periodic dynamic, closer to a higher-order solution of the NLSE [161]. It contributes, in addition to the effects of losses on regular recurrences, to a worse agreement between experiments and numerics in this case than for shifted recurrences. Nevertheless, we were able to report the observation of a high number of recurrences (4 periodic cycles for shifted recurrences and almost 5 for regular recurrences), which had never been done before in optical fibers. These results have been published in [48]. The very convincing agreement of experiments with numerics confirms the efficiency of the active loss compensation scheme. It then opens the way to investigate the thermalization of the FPUT recurrences [159], in the spirit of the original work of Fermi, Pasta, Ulam and Tsingou.

5.2 FPUT recurrences thermalization in optical fibers

By analogy with oscillator mechanics, we call FPUT thermalization in fiber optics the recurrences break-up generated by the predominance of noise-induced MI over coherently-driven MI. The energy isn't only distributed among the Fourier modes comb but also to all the spectrum including the noisy spectral components. It is often referred in this case as a noise-induced thermalization [159]. Even if noise-driven MI effect has

already been widely investigated in the context of supercontinuum generation and rogue waves formation [21, 23, 27, 98, 100–103], the simultaneous effects with coherently-driven MI have only been reported to increase the supercontinuum coherence or inhibit rogue waves formation [162, 163]. However their competition and the thermalization in the context of FPUT recurrences have never been experimentally investigated so far.

5.2.1 Noise-driven thermalization dynamic

Let us begin with simulations to understand how the competition between spontaneous and seeded MI can lead to the noise-induced thermalization of the FPUT recurrences. The single-shot evolutions of spontaneous MI, seeded MI and the competition between both dynamics are displayed in Fig. 5.4. First, the numerical results for noise-driven (or spontaneous) MI are presented on the left panel, similarly to Fig. 2.4 in Chapter 2. From the input power time profile in Fig. 5.4. (a), we get its evolution along the fiber length in Fig. 5.4. (b). From a low noise modulation of the plane wave background, the system evolves progressively towards the chaotic emergence of high amplitude pulses, from which we can distinguish solitonic structures, previously reported in [98, 100–103]. This initially incoherent modulation of the CW background from the noise leads the system to exhibit an irreversible behavior. From the input power spectrum in Fig. 5.4. (c), the spectral evolution along the fiber length is plotted in Fig. 5.4. (d). In addition to the monochromatic pump, a white noise floor is initially added, with a power spectral density $PSD = -112$ dBm/Hz. This noise is defined, in all the simulations performed here, with two independent Gaussian variables (mean 0 and variance 1) for the real and imaginary parts of each frequency bin. The level is then adjusted at the desired PSD by an all noise floor multiplying factor. At the beginning, up to 5 km, only the spectral components within the MI gain band are amplified (the cutoff frequency is $f_c = 56$ GHz). Then, the spectrum broadens due to FWM into a triangular shaped frequency continuum. It doesn't broaden indefinitely since the pump wave saturates and we observe then weak oscillations of the energy transfers, referred as spontaneous FPUT recurrences [98, 99]. Moreover, in the center panel are presented the numerical results for coherently-driven (or seeded) MI, as reported in Fig. 2.5 in Chapter 2. From the input power time profile and spectrum in Fig. 5.4. (e) and (g), we get the respective temporal and spectral evolutions along the fiber length in Fig. 5.4. (f) and (h). As it has been extensively presented in Chapter 2, we won't go into further details here. The system is initially excited, as usual, with a three waves input made of a pump and a signal/idler pair which modulate the pump close to the maximum of MI gain

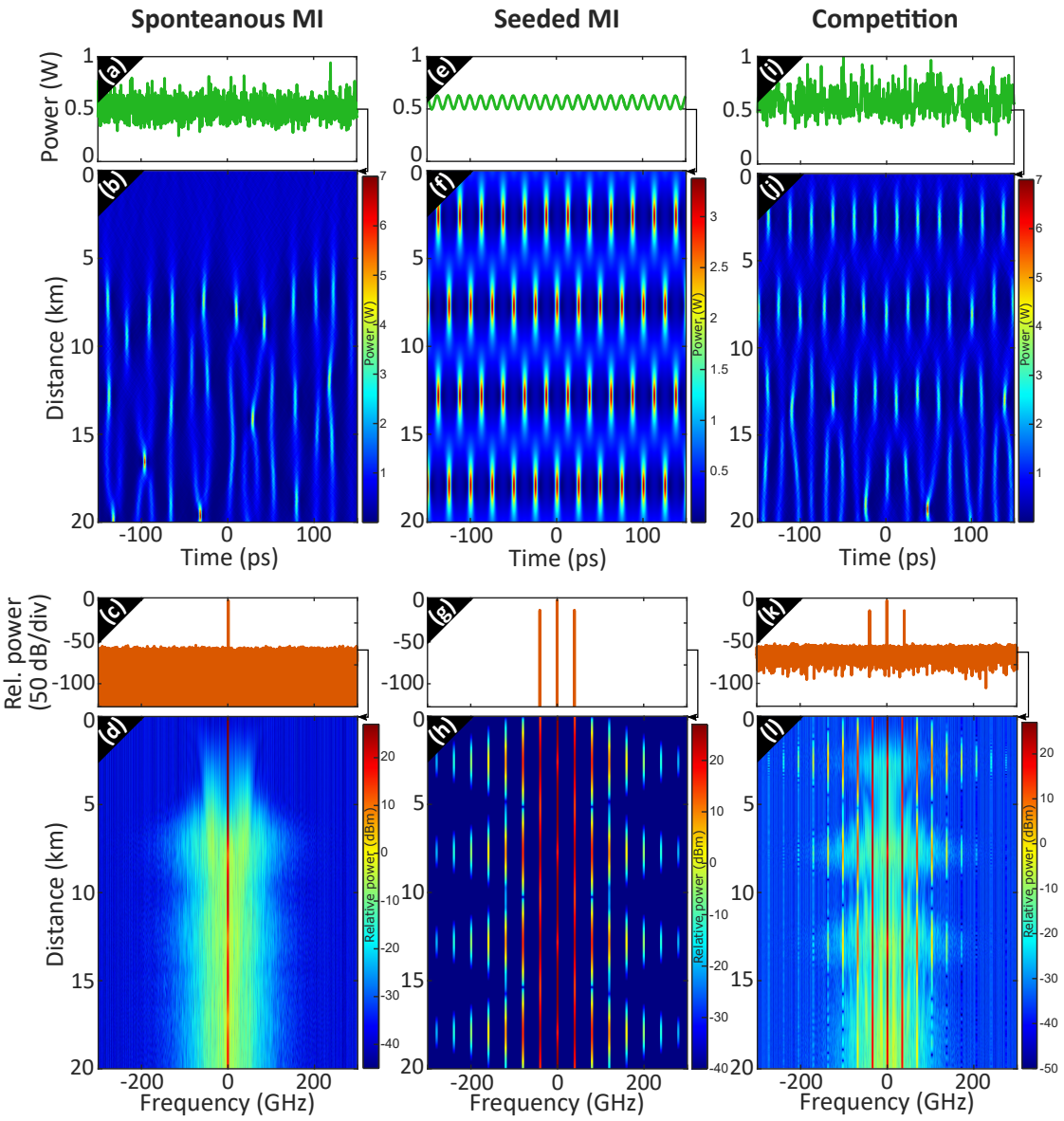

Figure 5.4: Numerical simulations of noise-driven MI (left panel), coherently-driven MI (center panel) and the competition between both (right panel). (a, e, i) Power time profiles at the fiber input. (b, f, j) Corresponding temporal evolutions of the power along the fiber length. (c, g, k) Power spectra at the fiber input. (d, h, l) Corresponding spectral evolutions of the power along the fiber length. General parameters: GVD $\beta_2 = -21$ ps^{2}km^{-1}, nonlinear coefficient $\gamma = 1.3$ W^{-1}km^{-1}, input pump power $P_p(z = 0) = 500$ mW, initial noise $PSD = -112$ dBm/Hz (for spontaneous MI and the competition) and modulation waves power $P_s(z = 0) = P_i(z = 0) = 32$ mW (for seeded MI and the competition).

(f_0 = 39.6 GHz). The initial relative phase is chosen at $\Delta\Phi(z=0) = -\frac{\pi}{2}$, as the three waves truncation is more robust in that case. We observe four growth and decay cycles here over 20 km fiber distance, both in the time and frequency domains. The system is reversible as it returns to the exact initial conditions at each recurrence and we could imagine to observe an infinite number of cycles by increasing the propagation distance as the system is initially noiseless. In reality, the system is never perfectly noiseless, even in numerical simulations, since it is limited by the digital precision (the minimal noise PSD is estimated at −400 dBm/Hz). Finally, in the right panel, the numerical results for the competition between spontaneous and seeded MI are presented. The input power time profile and spectrum are displayed in Fig. 5.4. (i) and (k) respectively and show a three waves input but with also a non negligible white noise floor (noise $PSD = -112$ dBm/Hz). The corresponding temporal and spectral evolutions along the fiber length are presented in Fig. 5.4. (j) and (l) respectively. At the beginning of the propagation, we discern two recurrences and a dynamic very similar to the coherently-driven MI case, which dominates the global process there. Then, further in the propagation, the frequencies in the MI gain band are amplified enough to disturb the energy transfers between the Fourier modes, which are progressively disappearing into the noise floor. Noise-driven MI becomes dominant as we observe the chaotic appearance of breathers and the disappearance of the periodicity both in space and time. The noise-induced thermalization of the FPUT recurrences in an optical fiber has just occurred. To highlight the evolution of the coherence during the propagation, we calculate the Shannon spectral entropy (SSE) which quantify the continuous spectral broadening and which is defined as [99, 164]:

$$SSE = -\sum_{\omega} p_\omega log_e(p_\omega) \tag{5.1}$$

where p_ω is the fraction of the total power contained in the frequency bin ω. In addition to the SSE evolution in Fig. 5.5. (a) for spontaneous MI (solid lines), seeded MI (dotted lines) and the competition between both (dashed lines), we plotted the evolution of the three central waves power $P_p + 2P_s$ (due to the symmetry $P_i = P_s$) in Fig. 5.5. (b). For noise-driven MI, the SSE is initially close to 1 and begins to increase around $z = 5$ km, corresponding to the broadening beyond the MI band due to FWM, to reach a maximum value around 7. It weakly oscillates around this maximum value during the rest of the propagation. It reveals the irreversible and incoherent behavior of spontaneous MI. For coherently-driven MI, the SSE remains weak below 2, exhibiting periodic oscillations associated to FPUT recurrences discrete broadenings. We deduce from it that seeded MI shows a reversible and perfectly coherent dynamic. For the

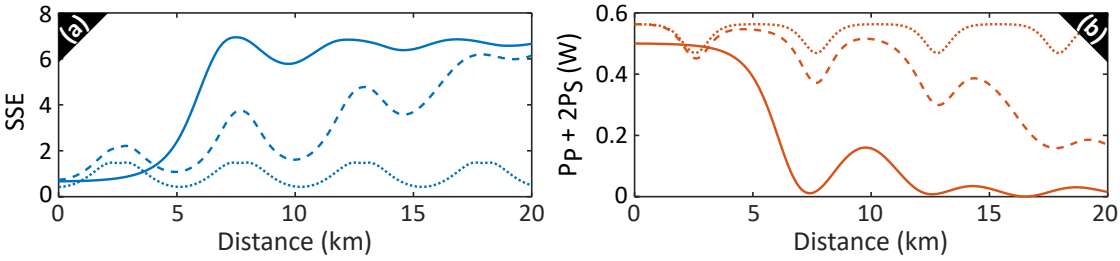

Figure 5.5: Evolutions along the fiber length of (a) the Shannon spectral entropy SSE and (b) the total power contained in the three central waves $P_p + 2P_s$. Solid lines: spontaneous MI; dotted lines: seeded MI; dashed lines: noise-induced thermalization.

noise-induced thermalization, the SSE follows the same evolution as seeded MI at the beginning but then increases up to 7 as in spontaneous MI. It reveals the progressive coherence loss resulting in an irreversible thermalized state, similar to noise-driven MI. We notice that the three central waves power follows the same but inverted evolution as the entropy, so we can use the evolution of $P_p + 2P_s$ to get a quantitative insight of the coherency evolution along the propagation. Indeed, the calculations of the SSE require to get all the spectrum amplitude evolutions (the Fourier modes and the noise floor) while our experimental setup allows us to get only the evolutions of a finite number of Fourier modes (classically three with the pump, the signal and the idler). In experiments, we can then look at the three central waves power evolution to substitute the SSE. The previous simulations have been realized with a noise floor level with $PSD = -112$ dBm/Hz. We easily understand that if we decrease this noise value, the thermalization will appear later on during the propagation, but sooner if we increase it. The transition speed to the thermalized state depends directly on the input noise floor level and we will be able to control it experimentally to accelerate the FPUT recurrences break-up and observe the transition from a perfectly periodic to an irreversible thermalized regime.

5.2.2 Experimental results

The system is initially excited, as usual, with a three waves input with a plane wave such as $P_p(z = 0) = 470$ mW. The propagation is performed in a 16.8 km long G.652 standard optical fiber, with a GVD coefficient $\beta_2 = -21$ ps^{2}km^{-1} and a nonlinear coefficient $\gamma = 1.3$ W^{-1}km^{-1}. It results in a MI phase-matching with a maximum gain frequency at $f_0 = 38.4$ GHz. The CW background is then modulated with a frequency close to f_0, at $f_m = 38.2$ GHz, with an amplitude so that $P_s(z = 0) = P_i(z = 0) = 47$ mW. The initial relative phase is set to $\Delta\Phi(z = 0) = -\frac{\pi}{2}$, to excite a dynamic very close to a first-order doubly periodic

solution. A power tunable white noise source is shaped both in the frequency domain with a band pass filter and in the time domain with an AO modulator (to keep only the useful signal and prevent from the main EDFA saturation with the noise) with the additional shaping stage (14) from Fig. 3.1 in Chapter 3. It is then easily combined to the nonlinear main pulses as the secondary AWG is synchronized. The input noise power is increased progressively, with a PSD from −121.3 to −91.9 dBm/Hz. For each initial noise level value, we record the pump and signal waves (due to the symmetry, we consider that the idler wave evolves identically to the signal) power evolutions along the fiber length and the spectrum at the fiber end. These experimental results are summed up in the upper panel of Fig. 5.6. In Fig. 5.6. (a), we display the fiber output spectra as a function of the initial noise power level. At low input noise PSD, all the Fourier modes within the presented band are discernible, namely the pump, the signal/idler pair and the first harmonics at $f = \pm 76.4$ GHz. However, we notice that the noise between the frequency lines is amplified by MI. It creates incoherent lobes in the middle but spectral holes closer to the Fourier modes, which are explained through multiple FWM process and demonstrated in [165]. By further increasing the input noise PSD, the Fourier modes power decreases and the first-order sidebands are even falling into the noise floor from −105 dBm/Hz. We also notice the increase of the inter-bands lobes power. The signal/idler pair in turn falls from about −95 dBm/Hz into the noise, which is amplified into a triangular shaped continuum. This shape is typical from parametrically driven systems [28] and spontaneous MI. Indeed, with a high input noise floor, most of the pump wave energy is used to amplify the noise components at the expense of the coherent energy transfers with the Fourier modes. Noise-driven MI takes then the lead in the competition with coherently-driven MI. We report in Fig. 5.6. (b), (c) and (d) the power evolutions of the pump (solid blue line), the signal (dotted blue line) and the relative evolution of the power contained in the three central waves $P_p + 2P_s$ along the fiber length for the respective input noise PSD of −121.3, −101.8 and −92.4 dBm/Hz. In the first case, the recordings are performed with the intrinsic noise of the setup as no noise is added. We observe three recurrences and a half within the fiber length which are well resolved, even though we notice a slight decrease of the total power in the three waves. Indeed, the SNR of the three waves input is very good but still insufficient to observe a perfectly coherent dynamic all along the fiber length, as we saw in the previous section or in [48]. The process still remains highly coherent with seeded MI dominating spontaneous one throughout the propagation. In the second case, the pump and signal powers decrease much more and the power contained in the three waves is down to only 17% at the fiber end. The remaining energy have been transferred to the

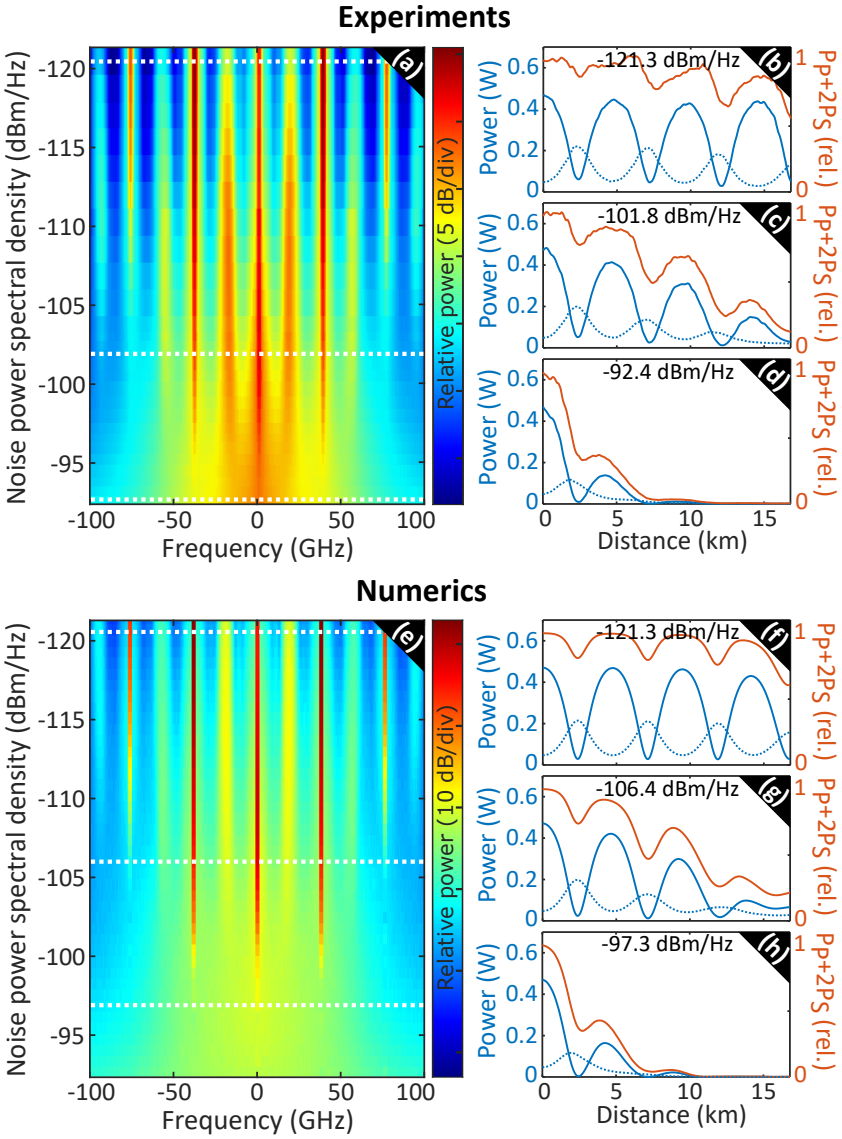

Figure 5.6: (a), (e) Evolution of the fiber end spectrum as a function of the initial noise PSD. (b), (c), (d) and (f), (g), (h) Power evolutions of the pump (solid blue line), the signal (dotted blue line) and the total of the three central waves $P_p + 2P_s$ (solid orange line) along the fiber length. The upper panel is for experimental recordings and the lower one for numerical data.

noise components through the spontaneous MI process, which is no longer negligible. In the last case, we can only distinguish a single recurrence as the pump and signal powers decrease very quickly (less than 50% remaining in the three waves after half a recurrence). The Fourier modes, even the pump, are dropping rapidly to the noise

floor level and the system turns into an incoherent frequency continuum. It evolves irreversibly to a thermalized state, which is accompanied by the FPUT recurrences break-up and an impossibility to come back to a coherent Fourier modes comb state. These experimental results are compared with numerical simulations of the NLSE which are displayed in the lower panel of Fig. 5.6. A very good agreement between experiments and numerics is obtained. Indeed, the experimental dynamic is very similar to the one predicted by the simulations, both looking at the output spectra which reveal the irreversible evolution towards a thermalized state and the Fourier modes powers which reveal the FPUT recurrences break-up. We also calculated and plotted the evolution of the fiber output SSE in Fig. 5.7. (a) for experiments (red crosses) and numerics (solid blue line). We notice similar behaviour between both of them as it logically increases

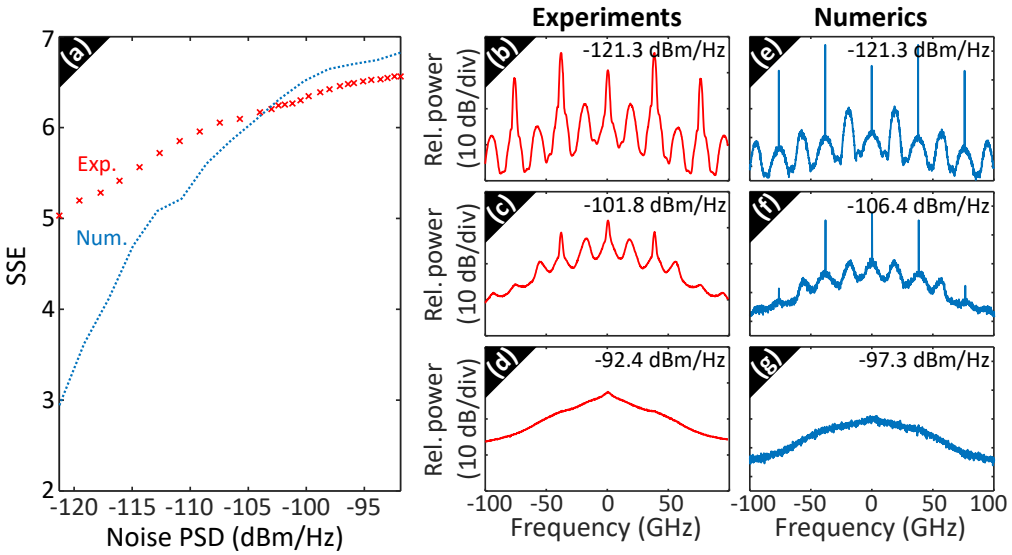

Figure 5.7: (a) Experimental (red crosses) and numerical (solid blue line) evolution of the fiber output SSE as a function of the initial noise PSD. Calculated within [−100 GHz; 100 GHz]. (b), (c), (d) Experimental and (e), (f), (g) numerical spectra at the fiber end for increasing input noise PSD values.

with the input noise level. Indeed the higher the initial noise is, the higher it will be at the fiber end and the more continuously broadened it will be. However the numerical SSE is much lower at low initial noise PSD than the experimental one. We can find the explanation in the spectra displayed in the right panel of Fig. 5.7. Despite the very thin linewidth of our laser (100 Hz), the Fourier modes of the recorded spectrum in Fig. 5.7. (b) are much thicker, due to the limited resolution of the OSA (4 GHz), than the numerical ones in Fig. 5.7. (e). It artificially broadens the real spectrum and increases

the SSE. By increasing the input noise PSD from −121.3 dBm/Hz to −101.8 dBm/Hz and to −92.4 dBm/Hz in Fig. 5.7. (b), (c) and (d) respectively, we observe the progressive transition to a thermalized state. The Fourier modes are progressively falling into the noise floor and irreversibly evolving into a triangular shaped frequency continuum, as seen previously in Fig. 5.6. The agreement with the spectra from numerics is also very convincing as a very similar transition is observed. At the time of this manuscript printing, the corresponding results are published as a preprint [49] and are currently processed to be published in Physical Review A.

Chapter conclusions

In this chapter, we managed to report, in a first section, the observation of multiple FPUT recurrences, up to 4 for $\Delta\Phi(z=0) = -\frac{\pi}{2}$ and even almost 5 for $\Delta\Phi(z=0) = 0$. It was made possible thanks to an improved SNR of the initial excitation and the efficiency of the active loss compensation scheme. The very good agreement with the NLSE numerics highlighted the conservativity of our system. However, the dynamic remained highly periodic and reversible and didn't reveal any transition to a thermalized state. Then, in a second section, we triggered this transition by driving the initial noise and forcing the competition between spontaneous and seeded MI. We reported the transition from a perfectly reversible regime to a thermalized one and the recurrences break-up.

Chapter 6

Separatrix crossing and multiple symmetry breakings in weakly damped and forced FPUT recurrences

Outline of the current chapter

6.1 Theory of separatrix crossing from damping and forcing **86**
6.1.1 Numerical approach 86
6.1.2 Description from the three-waves model 89
6.1.3 Description from the finite-gap theory 90
6.2 Experimental demonstration **91**
6.2.1 Tuning of the loss and gain 91
6.2.2 Weak damping results 93
6.2.3 Weak forcing results 97
Chapter conclusions **100**

While the FPUT recurrences dynamics have been widely investigated in quasi integrable lossless systems by means of an active attenuation compensation, as in the previous chapters, it is interesting to have a global understanding of the phenomenon by studying it under realistic conditions. The perturbation effects that will be investigated here are the damping and forcing. They have already been studied analytically through the 3WM model in the NLSE with higher-order contributions to account for the effect of the wind in

[166] for deep-water waves (only forcing) and through the perturbative finite-gap theory in [167] (damping and forcing). Damping always exists in physical systems, through the fiber linear attenuation in fiber optics or the dissipation from viscosity in hydrodynamics. The effect of dissipation on FPUT cycles has been experimentally explored in water waves in [39], highlighting phase-shifted recurrences observation. Concerning the forcing, the system can naturally be forced in hydrodynamics by the effect of wind, as it is showed experimentally in [120], revealing the separatrix crossing induced by the forcing. However, in fiber optics, the system can't naturally be forced and requires then an additional system such as a distributed amplifier along the fiber span. To the best of our knowledges, the effects of weak damping and forcing on FPUT recurrences process have never been investigated in fiber optics so far. In our experiments, instead of settling the Raman pump power to the optimal loss compensation as we did in Chapters 4 and 5, we tune it to reach either the weak damping regime with an undercompensation or the weak forcing regime with an overcompensation. Thanks to a fine tuning of the Raman pump power, we will show that we also manage to observe critical points corresponding to the separatrix crossing and thus revealing multiple symmetry breakings. In this chapter, we will first present the theoretical models which allow to predict the effects of damping and forcing and the symmetry transition critical points. Then, we will detail the experimental demonstration with the loss and gain tuning method and the results for both the damping and the forcing.

6.1 Theory of separatrix crossing from damping and forcing

The theoretical development have been realized in collaboration with Stefano Trillo who derived the analytical formalism presented in the subsection 6.1.2.

6.1.1 Numerical approach

Let us begin by considering the NLSE from Eq. 1.10, with damping or forcing written as:

$$\frac{\partial E(z,T)}{\partial z} = -i\frac{\beta_2}{2}\frac{\partial^2 E(z,T)}{\partial T^2} + i\gamma|E(z,T)|^2E(z,T) - \frac{\alpha}{2}E(z,T) \tag{6.1}$$

where α is the linear attenuation coefficient as defined in Eq. 1.1 (if $\alpha > 0$) or the linear amplification coefficient (if $\alpha < 0$). For the latter case, we introduce the coefficient g such $g = -\alpha$. If $\alpha = 0$, we saw in the previous chapters that the FPUT recurrences can exhibit two distinct types of recurrences depending on the initial modulation conditions. Either it is described as unshifted recurrences (inner single loop trajectory in the phase-plane)

with in-phase compression points, or as shifted recurrences (outer double loop trajectory in the phase-plane) with compression points shifted by half a temporal period at each recurrence. We also know from [42] and have demonstrated in Chapters 4 and 5 that both types can be excited from a three waves input with the suitable initial relative phase conditions. The systems were considered as quasi-integrable and the recurrences types either unshifted or shifted throughout the propagation. We display, in Fig. 6.1, numerics from damped/forced NLSE (Eq. 6.1 with $\alpha > 0$ or < 0 respectively) to highlight the effect of a linear loss and gain on the FPUT recurrences. A convenient way to study the impact of damping and forcing is to plot the evolution of the signal wave power P_s along the fiber length as a function of α or g. This is what we did in Fig. 6.1. (a) and (b) to investigate the incidence of the linear attenuation α ($\alpha > 0$) on initially unshifted ($\Delta\Phi(z = 0) = 0$) and shifted ($\Delta\Phi(z = 0) = -\frac{\pi}{2}$) excitation respectively. While the damping only induces a slight decrease of the recurrence period for the shifted case, it generates a much more complex dynamics for the unshifted case. We observe a succession of critical loss values α_{cn}, where n is a non-zero positive integer. These critical points are characterized by the shift of the $(n+1)^{th}$ signal maximum and the followings at very long distances. Even if the n^{th} recurrence period seems to asymptotically increase to infinity similarly to an AB dynamics at this point, we verified numerically that the following compression point actually appears at a finite distance. Such critical points originate from the separatrix crossing during the propagation and delimit transitions from unshifted to shifted recurrences. The space-time power diagrams, with α between α_{c3} and α_{c2}, between α_{c2} and α_{c1} and beyond α_{c1} in Fig. 6.1. (e), (f) and (f) respectively, help us to identify a general behavior. Considering an attenuation value such as $\alpha_{cn} < \alpha < \alpha_{c(n-1)}$, the first n maximum compression points are in phase while the next ones are phase-shifted. It signifies that the separatrix has been crossed during the n^{th} recurrence. We also plotted the approximated distances where the separatrix crossings took place (dashed white lines). In Fig. 6.1. (c) and (d), we displayed similar numerical results but with a linear amplification ($\alpha < 0$ and $g = -\alpha$) from unshifted and shifted recurrences excitation respectively. The forcing only reduces the spatial period in the single loop orbit case but exhibits critical amplification values g_{cn} in the double loop orbit case. The dynamic in the vicinity of these critical points is comparable to the damping as it also results from the separatrix crossing during the propagation. Conversely, it transits from a shifted to an unshifted orbit. From the space-time power profiles in Fig. 6.1. (h), (i) and (j), we also deduce a general behavior according to the value of g. If $g_{cn} < g < g_{c(n-1)}$, the first n maximum compression points are consecutively shifted by half a temporal period while the following ones are in-phase with the n^{th} one. The separatrix crossing occurs

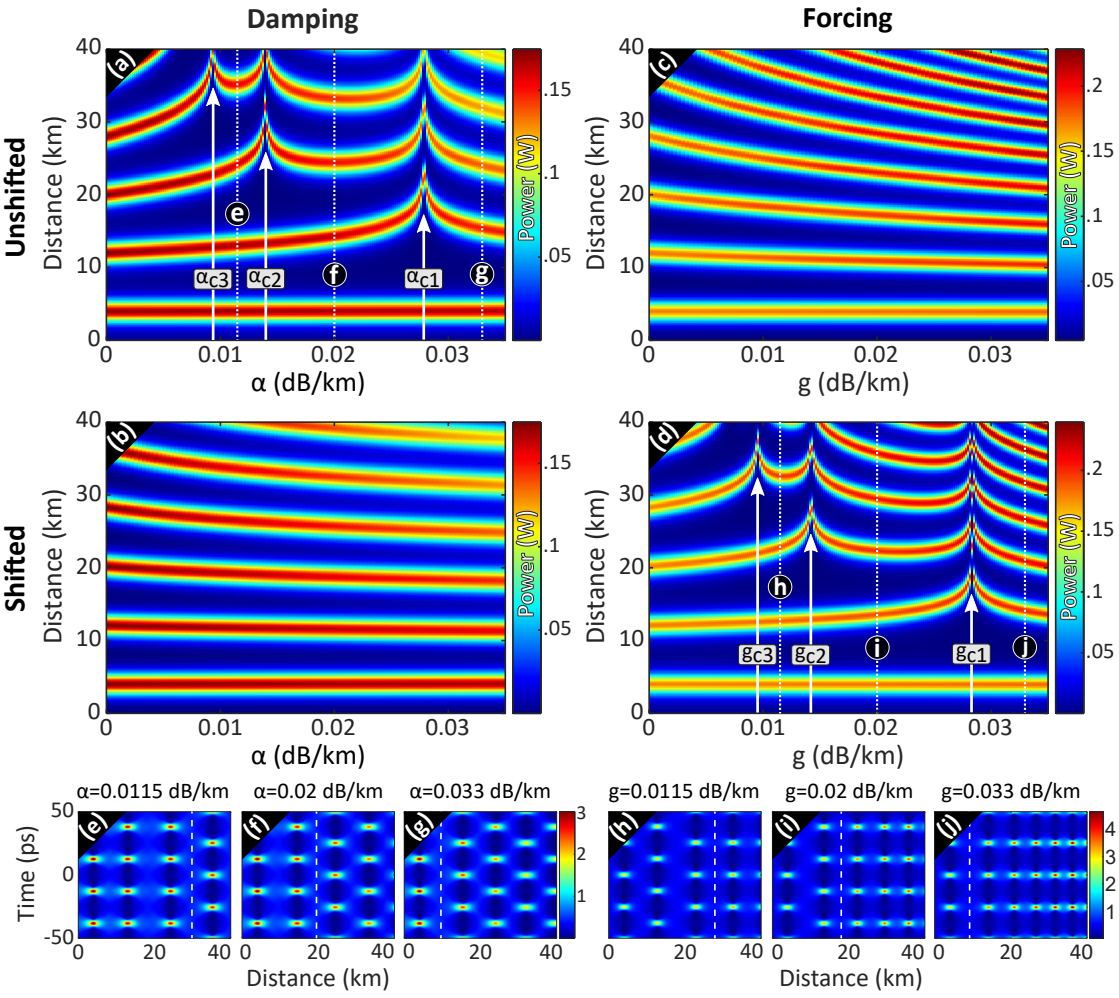

Figure 6.1: False-color plot of the signal power P_s evolutions along the fiber length as a function of weak damping α from (a) an unshifted orbit and (b) a shifted orbit excitations, of weak forcing g from (c) an unshifted orbit and (d) a shifted orbit excitations. (e), (f), (g) Space-time power diagrams from (a) for $\alpha = \{0.0115, 0.02, 0.033\}$ dB/km. (h), (i), (j) Space-time power diagrams from (d) for $g = \{0.0115, 0.02, 0.033\}$ dB/km. Parameters: $\beta_2 = -21$ ps^{2}km^{-1}, $\gamma = 1.3$ W^{-1}km^{-1}, $P_p(z=0) = 500$ mW, $P_s(z=0) = P_i(z=0) = 5$ mW and $f_m = 39.6$ GHz. Unshifted recurrences excitation are performed with $\Delta\Phi(z=0) = 0$ while shifted with $\Delta\Phi(z=0) = -\frac{\pi}{2}$.

then before the end of the n^{th} recurrence (approximated locations in dashed white lines). Indeed, in the case of damping or forcing, the system is not integrable anymore and the recurrences deviate from the doubly-periodic solutions of the NLSE. The separatrix, which exhibits an AB dynamics and delimits both FPUT types, can then be crossed during the propagation, at the origin of multiple symmetry breakings. To describe

such complex dynamics and predict the appearance of the critical points of separatrix crossing, it is helpful to use theoretical models to get a broader view of the process.

6.1.2 Description from the three-waves model

In [50], we introduced the Hamiltonian formulation of the truncated 3WM model in case of damping, derived by Stefano Trillo, which can also be generalized to the forcing. This non-conservative system can rigorously be described with a Hamiltonian which depends on the distance variable z (in opposition to an autonomous Hamiltonian for a conservative system). The critical attenuation values α_{cn} of symmetry breaking can be calculated thanks the Hamiltonian conservation and are then solutions of the following equation:

$$H_0 = \frac{\alpha_{cn}\omega_m^2}{2}\int_0^{nz_{per}} exp(\alpha_{cn}z)\eta(z)dz \tag{6.2}$$

where $H_0 = \eta_0(1-\eta_0)cos(2\Delta\Phi_0) + (1-\frac{\omega_m^2}{2})\eta_0 - \frac{3}{4}\eta_0^2$ is the initial 3WM Hamiltonian [42]. ω_m is the normalized modulation frequency such as $\omega_m = \frac{2\Omega_m}{\Omega_c}$, z_{per} is the longitudinal period without damping/forcing, η is the modulation power fraction such as $\eta = 2\eta_s$, $\Delta\Phi_0 = \Delta\Phi(z=0)$ and $\eta_0 = \eta(z=0)$. The α_{cn} values obtained from this Hamiltonian approach of the 3WM model are plotted as a function of the initial relative phase and the signal to pump ratio for $n = \{1,2,3\}$ in Fig. 6.2. We notice that α_{cn} follows a cosine

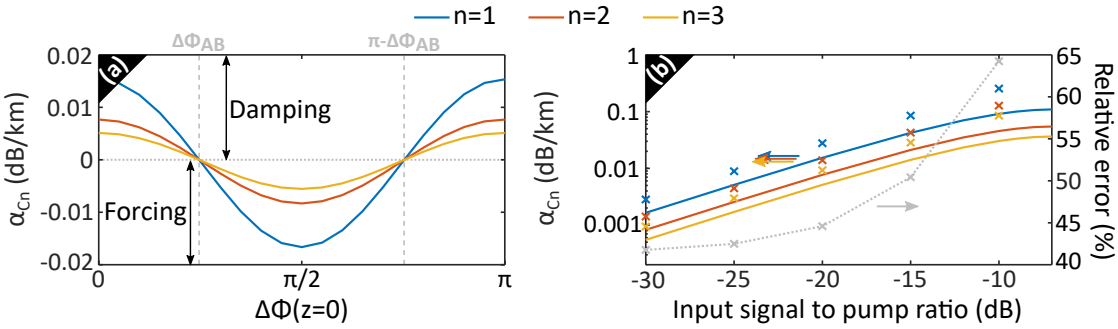

Figure 6.2: Evolution of α_{cn} from the 3WM model Hamiltonian for $n = \{1,2,3\}$ as a function of (a) the initial relative phase with $\frac{P_s(z=0)}{P_p(z=0)} = -20$ dB, and (b) the input signal to pump ratio with $\Delta\Phi(z=0) = 0$. In addition to the 3WM model (solid lines), α_{cn} are calculated from damping NLSE numerics and displayed in (b) (crosses), with the corresponding relative error (grey crosses and dotted line). The other parameters are the same as in Fig. 6.1.

wave as a function of $\Delta\Phi(z=0)$ in Fig. 6.2. (a). The phase values in $[0;\Delta\Phi_{AB}]$ and $[\pi-\Delta\Phi_{AB};\pi]$ are prone to separatrix crossing in case of damping as they initially excite

unshifted orbits, while the values in $[\Delta\Phi_{AB}; \pi - \Delta\Phi_{AB}]$ are prone to separatrix crossing in case of forcing due to the initial shifted orbits excitation (Fig. 6.1). In this case $\Delta\Phi_{AB}$ is very close to $\frac{\pi}{4}$ as the initial modulation amplitude is low. We also notice that the closer we are from the AB limit case, the smaller is the perturbation required to cross the separatrix, as logically expected. In addition to the 3WM model (solid lines), we also plotted the critical attenuation values obtained from the integration of the NLSE from Eq. 6.1 (crosses) and the relative error (grey crosses and dotted line) in Fig. 6.2. (b). The separatrix crossing values increase with the input modulation amplitude as low input signal to pump ratios are closer to the separatrix and require then weaker perturbations to cross it. The relative error between the 3WM model and the full-spectrum NLSE (calculated as the absolute error divided by the full-spectrum NLSE value) increases with the modulation amplitude but also remains non negligible at low initial signal to pump ratios (around 42% at −30 dB). The 3WM model and its Hamiltonian approach give an interesting qualitative tool to apprehend and understand the separatrix crossing and the symmetry breaking from forcing and damping in the FPUT recurrences. However, it remains insufficient to give quantitative predictions as it underestimates the critical points values.

6.1.3 Description from the finite-gap theory

The influence of damping and forcing on FPUT recurrences is assessed through a more accurate approach in [167], the perturbative finite-gap theory of the NLSE. Such approach is valid for small input modulation amplitudes and weak attenuation/amplification values. As an example, the SMF-28 attenuation value of 0.2 dB/km leads to a normalized loss of 0.071 ($\ll 1$). Then, the condition of weak damping/forcing will always be fulfilled in experiments. From this theory is derived a simple formula for the critical attenuation values (details can be found in [167]):

$$\alpha_{cn} = \frac{\eta_0 p_0 e_+ e_-}{ng} \tag{6.3}$$

where p_0 and η_0 are the input pump and modulation power fractions respectively, e_+ and e_- are the growing and decaying eigenvectors of MI, as defined in [50, 115, 167] and g is the normalized MI gain at the frequency ω_m such as $g = \omega_m\sqrt{4p_0 - \omega_m^2}$. Similarly to Fig. 6.2, we display the evolution of the critical loss/gain values as a function of the initial relative phase and the initial modulation amplitude in Fig. 6.3. We notice in Fig. 6.3 that it follows the same cosine trend in $\Delta\Phi(z = 0)$ as for the 3WM model.

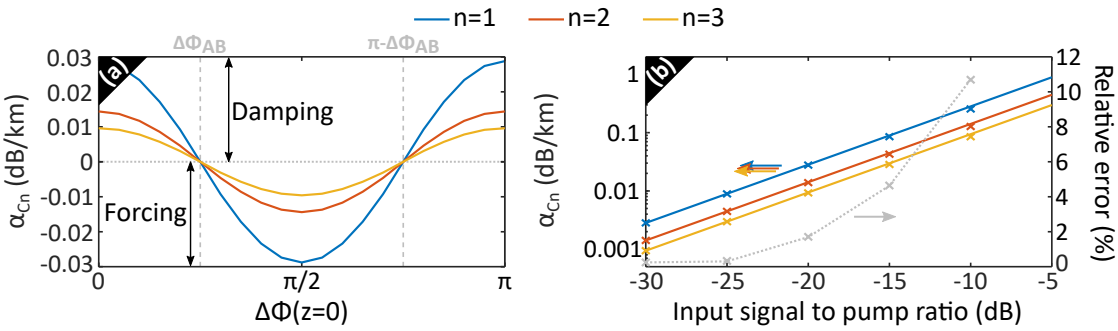

Figure 6.3: Evolution of α_{cn} from the finite-gap theory for $n = \{1, 2, 3\}$ as a function of (a) the initial relative phase with $\frac{P_s(z=0)}{P_p(z=0)} = -20$ dB, and (b) the input signal to pump ratio with $\Delta\Phi(z = 0) = 0$. In addition to the finite gap approach (solid lines), α_{cn} are calculated from damping NLSE numerics and displayed in (b) (crosses), with the corresponding relative error (grey crosses and dotted line). The other parameters are the same as in Fig. 6.1.

The main difference is the values of separatrix crossings, as the finite-gap predicts 70% more damping/forcing to reach the critical points. As for the 3WM model case, we simultaneously plot the critical attenuation values from the finite-gap theory (solid lines) and from numerics of the damping NLSE (crosses), as well as the relative error (grey crosses and dotted line). We notice that the agreement is way better than in the previous case. The finite-gap approach is especially very accurate at low modulation amplitudes with an error lower than 5% up to −15 dB. Indeed, it makes sense as this theory is valid for small initial sidebands and as higher modulation amplitudes result in higher critical attenuation values (the weak damping/forcing approximation would be questionable there). The perturbative finite-gap theory offers then remarkable quantitative estimations of α_{cn} for sufficiently weak input modulation sidebands while it slightly overestimates them at higher initial modulation.

6.2 Experimental demonstration

6.2.1 Tuning of the loss and gain

To study experimentally the separatrix crossings induced by a weak damping and forcing in the FPUT recurrences framework, the key feature is the tuning of the effective loss and gain experienced by the signal during the propagation in the fiber. For this purpose, we use the backward Raman pumping scheme, presented earlier in Chapter 3. In Chapters 4 and 5 and in [42, 44–48], it was used in an optimal operating regime to compensate the

attenuation and get an almost fully transparent fiber. In the following experiments, the Raman pump power is tuned below the optimum to obtain a variation of the effective loss, and above this optimum to get a variation of the effective gain. If we note P_R^{Opt} the Raman pump power required to optimize the loss compensation along a specific fiber span, the attenuation can be tuned from the intrinsic fiber loss value (0.2 dB/km in our case) with $P_R = 0$ mW to $\alpha_{eff} = 0$ dB/km with $P_R = P_R^{Opt}$. The amplification is tuned with $P_R > P_R^{Opt}$. To determine the effective loss or gain value associated to a specific pump power value, we record the OTDR traces from weak pulses propagation with multiple Raman pump power values. By weak we mean that the signal power is low enough that the nonlinear effects are negligible. The pulses are weaker than 50 mW, which corresponds to a nonlinear length of more than 15 km. They propagate in around 20 km long fiber spans, which is slightly more than one L_{NL}. Therefore, we can consider that the approximation is valid. Few examples of OTDR traces are plotted in Fig. 6.4. (a) and (b) for damping and forcing respectively. In what follows, we distinguish the effective loss and gain estimations as both experiments were performed on different times and with two different fiber span lengths, 20.15 and 16.73 km respectively. Indeed, we reduced the fiber length in the case of weak forcing, as the gain factor increased the nonlinearity up to the recurrences break-up and the noise-driven thermalization at the fiber end (as observed in Chapter 5). For $P_R = 0$ mW, the Raman pump is switched off and the corresponding trace (solid blue line) reveals an exponential decay, as expected from the linear losses effect. Note that the OTDR traces cover twice the fiber length as the signal first travels forward and the Rayleigh backscattering travels then backward before being recorded at the fiber input. The evolution is fitted with an exponential curve (dashed blue line) from which we retrieve an intrinsic attenuation value $\alpha = 0.208$ dB/km, in very good agreement with the datasheet value of 0.2 dB/km [130]. For $P_R = 270$ mW (solid green line), the loss compensation is almost perfect i.e. $P_R \simeq P_R^{Opt}$ as a quasi flat OTDR trace is recorded. These measurements are repeated for multiple Raman pump power values in $[0;300]$ mW (a slight overcompensation is observed close to 300 mW) and the results are summarized in Fig. 6.4. (c). We notice that the effective loss values α_{eff} are linearly tuned with the Raman pump power. In case of forcing, the OTDR trace reveals an exponential growth, as for example with $P_R = 410$ mW (solid yellow line) in Fig. 6.4. (b). By varying the Raman pump power from 200 mW (slight damping below 240 mW) to 410 mW, we confirm the linear control of the effective gain g_{eff} in the forcing regime (Fig. 6.4. (d)). We notice that the optimal Raman pump power P_R^{Opt} is higher in the damping case (around 290 mW) than in the forcing case (around 240 mW), which is due to the fiber span lengths difference. Indeed a longer fiber (20.15

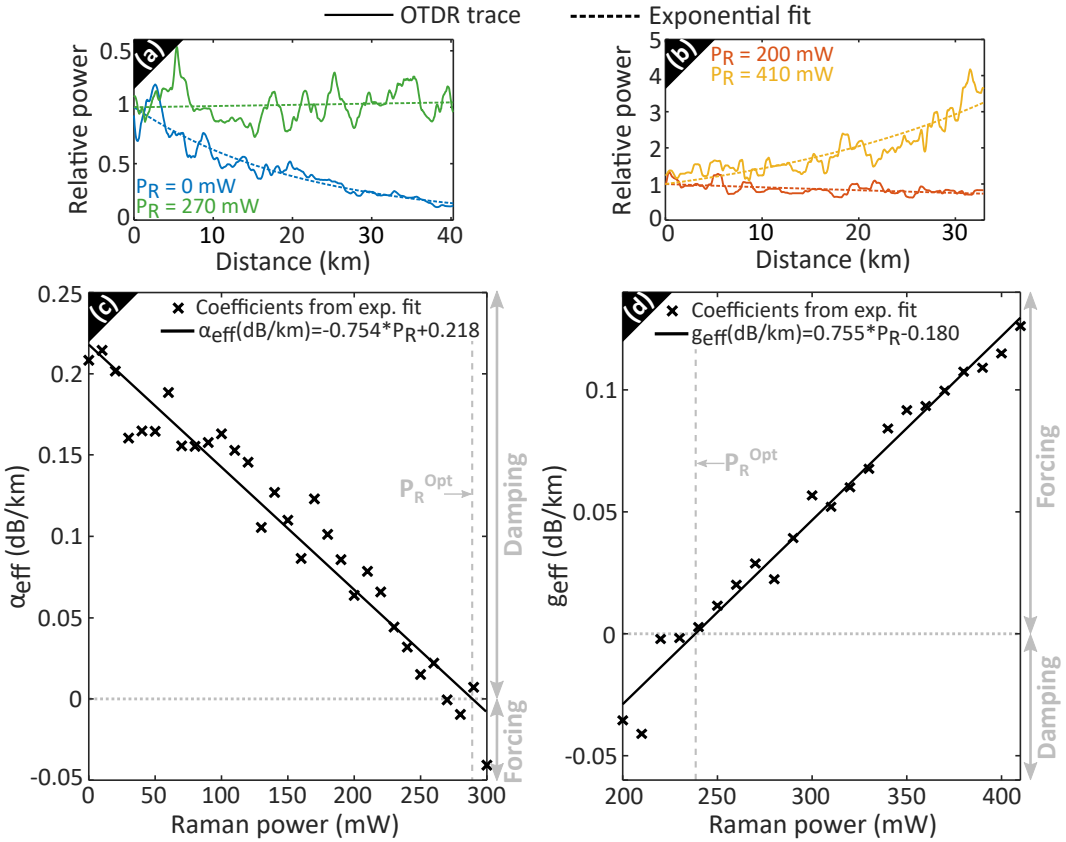

Figure 6.4: Relative evolutions of the backscattered signal power with (a) $P_R = 0$ mW (solid blue line), $P_R = 270$ mW, (b) $P_R = 200$ mW and $P_R = 410$ mW. Evolution of (c) the effective loss and (d) the effective gain as a function of the Raman pump power P_R.

km) requires more Raman pump power to get an optimal loss compensation than a shorter one (16.73 km). The linear fits from Fig. 6.4. (c) and (d) are used to calibrate α_{eff} and g_{eff} in the following experiments with respect to the Raman pump power value.

6.2.2 Weak damping results

To observe a separatrix crossing induced by the damping, the system has to be initially excited by an unshifted orbit (in the conservative case). The initial relative phase is then set to $\Delta\Phi(z = 0) = 0$. The propagation is performed in a 20.15 km long SMF-28 fiber, with $\beta_2 = -19$ ps^{2}km^{-1} and $\gamma = 1.3$ W^{-1}km^{-1}. The pump power being set to the input value $P_p(z = 0) = 480$ mW, we modulate with a frequency $f_m = 38.2$ GHz, close to the perfect phase-matching frequency of $f_0 = 41$ GHz. The maximum attenuation value being limited by the intrinsic fiber linear losses, we designed the experiment

so that the first critical attenuation point α_{c1} appears below 0.2 dB/km. It can easily be done by reducing the input modulation power, as we saw in Fig. 6.3. Moreover, to also record the second critical attenuation point α_{c2}, we needed to record at least three growth and decay cycles within the fiber length (the higher is the modulation amplitude, the shorter is the spatial period). We chose then the input signal to pump ratio as a trade-off value of $\frac{P_s(z=0)}{P_p(z=0)} = -13$ dB i.e $P_s(z=0) = P_i(z=0) = 24$ mW. We display the evolution of the signal power $P_s(z)$ (as in Fig. 6.1) and the relative phase $\Delta\Phi(z)$ as a function of the effective attenuation (obtained from the Raman pump value according to Fig. 6.4. (c)) in Fig. 6.5. (a) and (b). In the ③ labeled region (Fig. 6.5. (a-b)), for α_{eff} between 0 dB/km and $\alpha_{eff,c2}$, the system is close to the optimal compensation of the losses. From the power evolution, we observe up to four complete recurrences, similarly to the results in Chapter 5 (five cycles were reported there due to a higher modulation amplitude). From the phase evolution (Fig. 6.5. (b)), $\Delta\Phi$ remains bounded in $[-\frac{\pi}{2}; \frac{\pi}{2}]$, oscillating around the input phase value. It is in very good agreement with the numerical predictions shown in Fig. 6.5. (c) and (d), obtained from the numerical integration of Eq. 6.1. For a specific value of attenuation in region ③, $\alpha_{eff} = 0.007$ dB/km ($P_R = 280$ mW), we reported the evolution in the phase-plane in Fig. 6.5. (e). The experimental data are plotted in solid lines while numerical data in dotted lines. The trajectory in the phase portrait remains in the right half-plane which confirms the phase bounding and reveals that all the recurrences are unshifted. We also displayed the space-time power profile from numerics in Fig. 6.5. (f) which corroborates that the consecutive compression points appear in phase. We don't observe any spatial shift of the first conversion peak with the evolution of α_{eff} as it is always reached at $z = 2.4$ km, in perfect accordance with numerics. While the dynamic of the first FPUT cycle is not affected by the fiber attenuation no matter its value, the following cycles are strongly impacted depending on the losses. By increasing the damping up to $\alpha_{eff,c2}$, the second, third and fourth conversion peaks appear progressively at longer propagation distance. The third one is even located close to the fiber end when $\alpha_{eff} = \alpha_{eff,c2}$ and decreases by further increasing the losses in region ②. The relative phase in Fig. 6.5. (b) even reveals a π-shift of the third conversion peak with respect to the first two for $\alpha_{eff} > \alpha_{eff,c2}$. It means that the third recurrence is phase-shifted from the unshifted first two cycles. The separatrix has been crossed during the second FPUT cycle as the third one is excited from a double loop orbit. We displayed the phase-plane evolution in Fig. 6.5. (g) for a specific attenuation value in region ② $\alpha_{eff} = 0.090$ dB/km ($P_R = 170$ mW). The trajectory evolves in the right half-plane for the first two cycles but is shifted in the opposite half-plane for the third one, completing a double loop orbit. It highlights

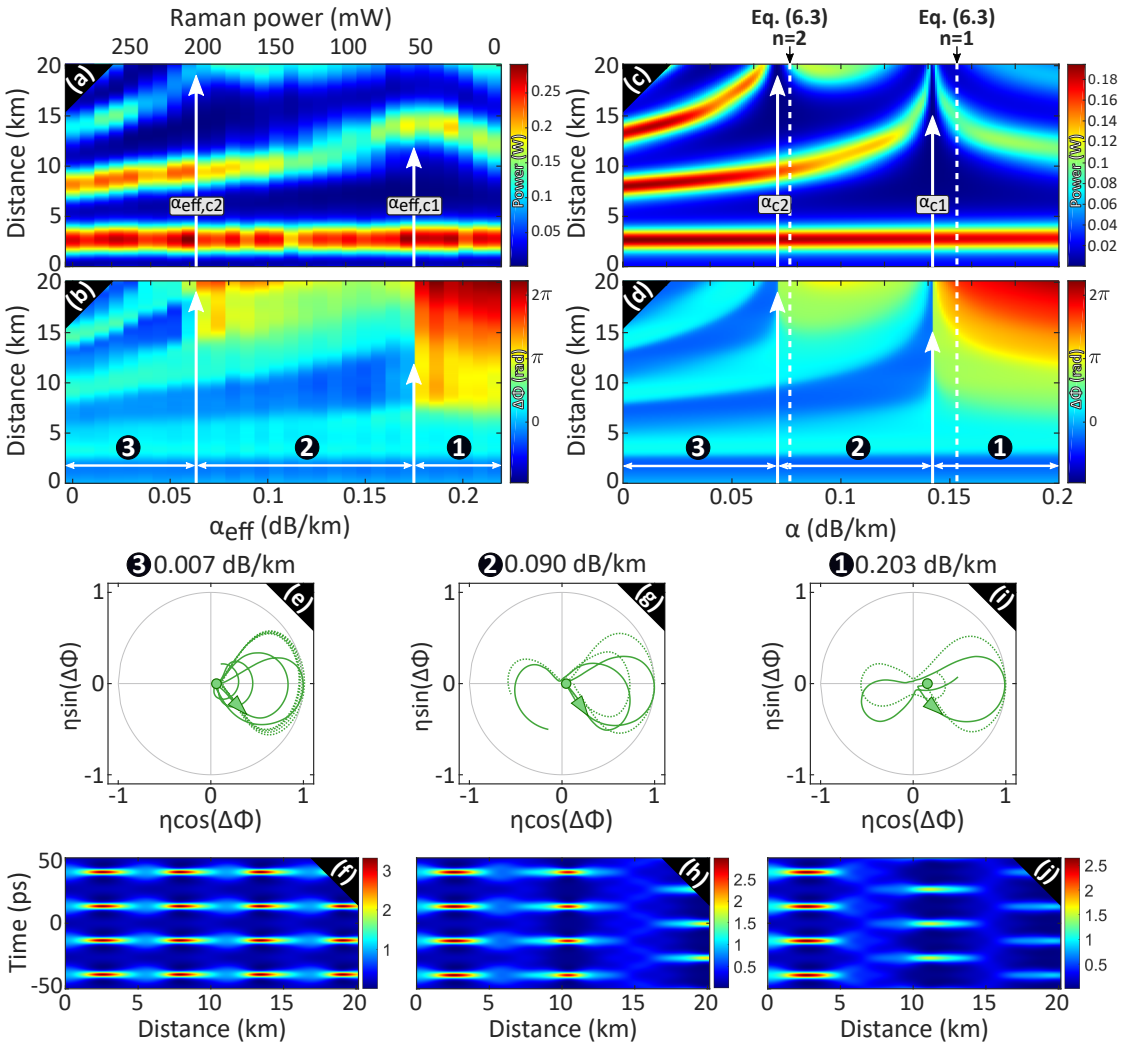

Figure 6.5: False color plots of (a), (c) the signal power evolutions and (b), (d) the relative phase along the fiber distance as a function of the effective attenuation. Left panel: experimental data; right panel: numerical data. (e), (g), (i) Trajectories in the phase-plane $(\eta cos(\Delta\Phi), \eta sin(\Delta\Phi))$ for α_{eff} = 0.007, 0.090 and 0.203 dB/km respectively. Experimental data are in solid lines and numerical ones in dotted lines. (f), (h), (j) Numerical space-time power diagrams.

the separatix crossing and the symmetry breaking of the third maximum compression point, as confirmed by the numerical spatio-temporal power evolution of the power in Fig. 6.5. (h). The global agreement between experiments and numerics is also very good in region ②. The system follows the same dynamic by increasing the damping up to $\alpha_{eff} = \alpha_{eff,c1}$. Close to this critical attenuation point, the second conversion

peak shifts even more to longer distances (the third one doesn't even appear anymore before the fiber end). However, beyond $\alpha_{eff,c1}$, the trend is inverted and the second and third conversion peaks appear closer and closer by increasing α_{eff}. The phase evolution in Fig. 6.5. (b) reveals a π-shift of the second and third cycles induced by the transition from region ② to ①. It is highlighted by the phase portrait in Fig. 6.5. (i) where the trajectory exhibits a double loop orbit, oscillating from one half-plane to the other between two consecutive FPUT cycles. Two consecutive compression points are then always shifted by half a temporal period, as confirmed by the space-time profile in Fig. 6.5. (j). The separatrix has been crossed during the first recurrence cycle, leading to a double loop orbit excitation of the consecutive growth and decay cycles. The experimental data are still concording to the numerical ones in region ①. Looking specifically at the critical attenuation values, we find $\alpha_{eff,c2} = 0.063$ dB/km ($P_R = 205$ mW) and $\alpha_{eff,c1} = 0.176$ dB/km ($P_R = 55$ mW) to be compared with the numerical values $\alpha_{c2} = 0.071$ dB/km and $\alpha_{c1} = 0.142$ dB/km. The overall agreement is good even if a non negligible gap is observed. As α_{cn} theoretically evolves according to a $\frac{1}{n}$ function (predicted by Eq. 6.3), we would expect $\alpha_{eff,c2}$ to be around 0.088 dB/km from the value of α_{c1}. Such a discrepancy can be attributed to the fluctuations of the effective attenuation α_{eff} from the ideal intrinsic attenuation α, as we operate within an active system. Moreover, the system initially excites a solution close to an B-type doubly-periodic solution of the NLSE, as $\Delta\Phi(z = 0) = 0$ (see Chapter 4), which turned out to be less stable to the input three waves truncation (see Chapter 4 for more details). We also superposed the critical loss values from the finite-gap theory in Eq. 6.3 (dashed white lines). Then, we calculated $\alpha_{c1} = 0.154$ dB/km and $\alpha_{c2} = 0.077$ dB/km, leading to a 8.5% error with the NLSE numerics. The experimental study was also limited to the observation of only the two first critical attenuation points. Indeed the observation of the higher order transition points would require to record a higher number of recurrences, and so to increase the fiber span length. A fine tuning of lower effective attenuation values (higher is the order n, smaller is α_{cn}), especially with much longer fibers, would involve a more efficient loss compensation scheme. Such improvements can be possible by the time shaping of the Raman pump, which would allow in theory to obtain any loss profile. This is studied in details in Appendix C. At the time of this manuscript printing, the corresponding results are published as a preprint [50] and are under consideration for publication.

6.2.3 Weak forcing results

Now that the effect of damping have been investigated, let us observe its counterpart in the forcing regime. In case of a weak gain, the separatrix is crossed only with an initial excitation of a shifted orbit (in the conservative case). As we amplify the system beyond the optimal compensation of the losses, we decrease the nonlinear length compared to the integrable case. It promotes then the noise floor amplification from MI and the noise-induced thermalization (as detailed in Chapter 5). To prevent such a detrimental effect, we use a shorter SMF-28 fiber span of 16.73 km and we limit the Raman pump to suitable power values P_R. As the fiber length have been reduced, we also increase the modulation amplitude. It allows both to get a sufficient number of FPUT cycles (at least three to be able to also observe g_{c2}) within the fiber span and to get a higher sidebands to noise ratio. Indeed, we remember from Chapter 4 that a high signal to pump ratio is not detrimental to excite a perfectly doubly-periodic A-type solution of the NLSE. The signal to pump ratio is then set to $\frac{P_s(z=0)}{P_p(z=0)} = -9.5$ dB and P_R maximum value to 410 mW, which allows to get an effective gain g_{eff} up to 0.13 dB/km. The initial relative phase we usually set to excite a shifted orbit is $\Delta\Phi(z=0) = -\frac{\pi}{2}$. However, for such an input phase, we expect from numerics that $g_{c1} = 0.268$ dB/km, which is beyond the achievable effective gain values. To get smaller critical points values, we need to choose $\Delta\Phi(z=0)$ to be closer to the separatrix, so that it requires a weaker perturbation to cross it (as predicted by the 3WM model in Fig. 6.2. (a) and the finite-gap theory in Fig. 6.3. (a)). We set then the initial relative phase to $\Delta\Phi(z=0) = 0.28\pi$. From the input pump power $P_p(z=0) = 470$ mW and the fiber parameters ($\beta_2 = -21$ ps^{2}km^{-1}, $\gamma = 1.3$ W^{-1}km^{-1}), we calculate the perfect phase-matching frequency at $f_0 = 38.4$ GHz. We set the modulation frequency very close to that value, at $f_m = 38.2$ GHz. We made similar recordings to the damping case, but with a Raman pump power P_R ranging from 200 to 410 mW (the corresponding g_{eff} according to Fig. 6.4 varies from −0.029 to 0.13 dB/km). We display the evolution of the signal power $P_s(z)$ and the relative phase $\Delta\Phi(z)$ as a function of the effective gain in Fig. 6.6. (a) and (b) respectively. In region ③, the system is close to the optimal compensation of the losses, with either a slight attenuation (down to $g_{eff} = -0.029$ dB/km) or a slight amplification (up to $g_{eff} = g_{eff,c2} = 0.043$ dB/km). We observe three complete FPUT recurrences looking at the power evolution (Fig. 6.6. (a)) but also a π phase shift between each consecutive cycles looking at the phase evolution (Fig. 6.6. (b)). This behavior is confirmed by the trajectory in the phase-plane in Fig. 6.6. (e) obtained for a specific effective gain $g_{eff} = -0.021$ dB/km ($P_R = 210$ mW). It oscillates from one half-plane to the other between two consecutive growth and decay cycles,

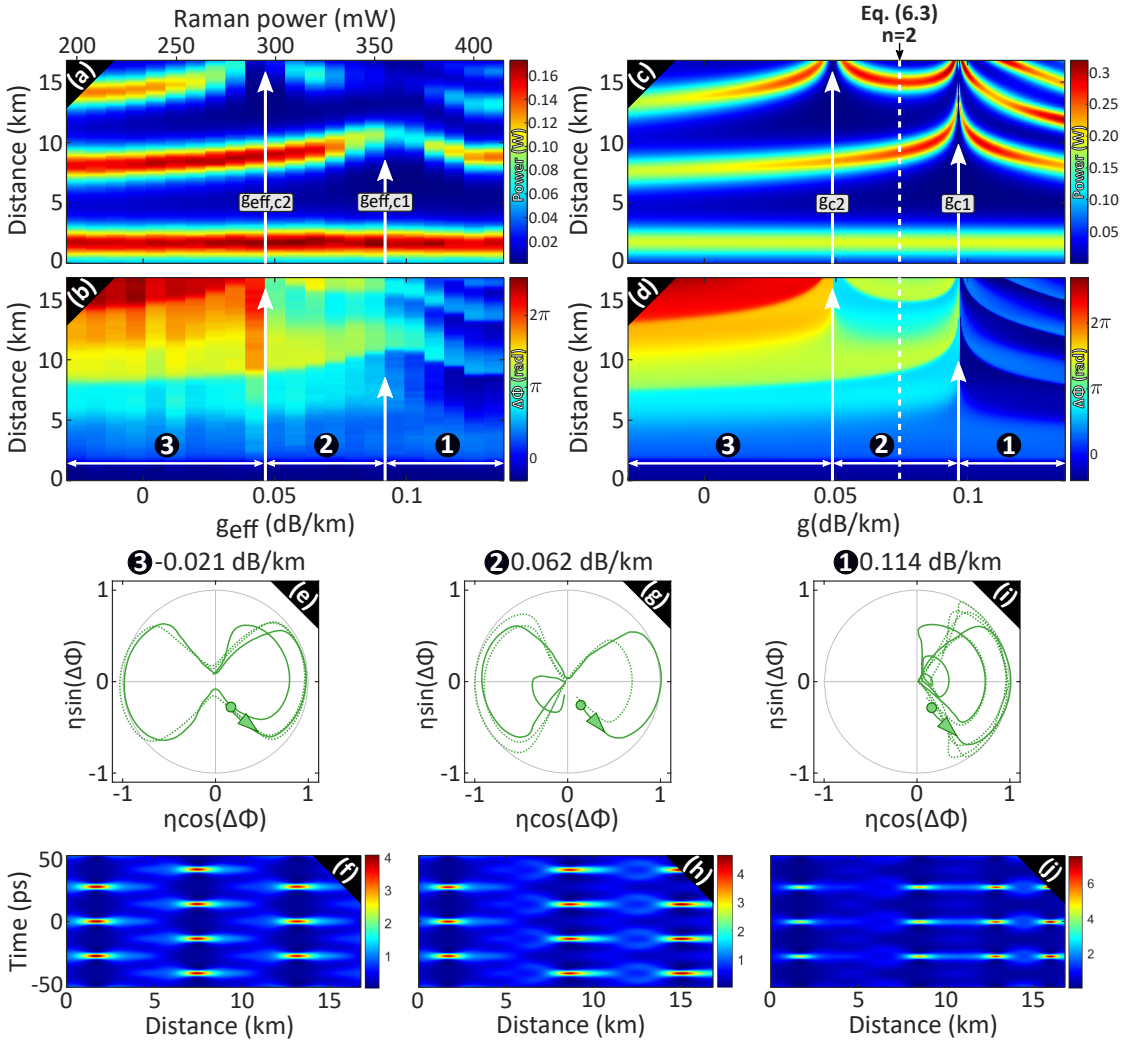

Figure 6.6: Same as in Fig. 6.5 but in case of weak forcing with an initial shifted double loop orbit excitation. The specific values of effective gain g_{eff} are (e-f) −0.021 dB/km, (g-h) 0.062 dB/km and (i-j) 0.114 dB/km.

as previously seen for shifted recurrences in Chapters 4 and 5. It signifies that two consecutive maximum compression points are shifted from half a temporal period, as it is revealed by the space-time power evolution obtained from numerics in Fig. 6.6. (f). This dynamic is not surprising because it behaves exactly the same as a shifted orbit excitation in an integrable system. These experimental results can be compared to the numerical results in Fig. 6.6. (c) and (d). I draw your attention on the fact that these numerical data were obtained with a different initial relative phase value than the experimental one. Indeed, the numerical results with $\Delta\Phi(z=0) = 0.28\pi$ don't predict

any critical transition point within [0; 0.13] dB/km. Then, we performed numerics with the input phase value which fits the best with the experiments ($\Delta\Phi(z = 0) = 0.335\pi$). Such a discrepancy will be discussed later in the section. Despite the initial conditions difference, we remark a very good agreement between experiments and numerics in region ①. By increasing the effective gain up to $g_{eff,c2} = 0.043$ dB/km ($P_R = 295$ mW), we notice that the third FPUT cycle period increases so that the corresponding conversion peak doesn't appear within the fiber length close to $g_{eff,c2}$. Beyond this critical gain point, in region ②, we record three conversion peaks again. However, the phase evolution reveals that there is no π phase shift between the second and third FPUT cycles anymore. It is confirmed by the phase-plane representation in Fig. 6.6. (g) with $g_{eff} = 0.062$ dB/km ($P_R = 320$ mW). While the first cycle follows a trajectory in the right half-plane, the second and third ones in the opposite half-plane. The separatrix has been crossed during the second FPUT cycle as the third one is excited by an unshifted single loop orbit. The numerical space-time power diagram in Fig. 6.6. (h) corroborates the conclusions from the experimental data. The first two maximum compression points are shifted from half a temporal period while the third one is in phase with the second. Below $g_{eff,c1} = 0.088$ dB/km ($P_R = 355$ mW), the second cycle period also increases and the corresponding conversion peak spatially shifts at higher fiber distances. However, beyond $g_{eff,c1}$, the trend inverts and the number of conversion peaks recorded within the fiber length increases up to 4 at $g_{eff} = 0.13$ dB/km in region ①. In this region, the phase remains bounded in $[-\frac{\pi}{2}; \frac{\pi}{2}]$, similarly to what has been observed in conservative systems from an unshifted single loop orbit excitation. It is revealed by the trajectory in the phase-plane in Fig. 6.6. (i) for $g_{eff} = 0.114$ dB/km, where all the cycles remain located in the right half-plane, in phase with each other. The numerical spatio-temporal evolution of the power highlights this behavior, with perfectly in phase four compression points. In this case the separatrix has been crossed during the first growth and decay cycle, leading to an unshifted orbit excitation from the second one. The overall agreement between experiments and numerics remains good in region ① and ②, except for the higher order conversion peaks ($n = 3, 4$) for which the recorded signal power is much lower than the one expected from the simulations. This can be attributed to the blurring effect (as detailed in Chapter 3) but especially to noise-induced MI. Indeed, we notice a decrease of the signal power maxima, similarly to what we observed in the noise-driven thermalization experiments in Chapter 5. Regarding the critical gain values, we find $g_{eff,c1} = 0.088$ dB/km ($P_R = 355$ mW) and $g_{eff,c2} = 0.43$ dB/km ($P_R = 295$ mW), which follows quasi perfectly the $\frac{1}{n}$ evolution function (predicted by Eq. 6.3). This can be explained by the fact that the system is initially excited by solutions close to the A-type

doubly-periodic solutions of the NLSE, which turn out to be more stable and robust to the input three waves truncation. For the numerical data, we get $g_{c1} = 0.091$ dB/km and $g_{c2} = 0.045$ dB/km but for $\Delta\Phi(z = 0) = 0.335\pi$. Indeed for exactly the same phase value than in experiments ($\Delta\Phi(z = 0) = 0.28\pi$), the numerical critical transition values are $g_{c1} = -0.008$ dB/km and $g_{c2} = -0.004$ dB/km. It corresponds to a system with an initially unshifted orbit excitation ($\Delta\Phi(z = 0) < \Delta\Phi_{AB}$) where the separatrix crossing occurs in case of weak damping. We suggest that such a discrepancy can simply be due to an imperfect control of the initial relative phase with the Waveshaper. Indeed, while a small shift of the initial relative phase is not detrimental far from the AB phase ($\Delta\Phi(z = 0) = \{0, \frac{\pi}{2}, \pi, ...\}$ for example), it can have a very strong impact on the dynamic close to it. As for the damping case, the observation of higher order g_{cn} would require to increase the number of recurrences recorded (by increasing the fiber length) and to improve the gain profile shaping through the Raman pump.

Chapter conclusions

In this chapter, we reported in a first section the theoretical models explaining the separatrix crossing induced by weak damping and forcing effects and predicting the transition critical points associated to the symmetry breakings. We showed that the 3WM model through the Hamiltonian formalism, derived by Stefano Trillo, offers a very good qualitative approach, while the perturbative finite-gap theory gives excellent quantitative predictions of the phenomenon. In a second section, we developed the experimental demonstration of forcing and damping effects on the FPUT recurrences process. We detailed the method of loss and gain tuning through the control of the backward Raman pump power and the experimental results for both the damping and forcing. In both cases, we highlighted two critical transition points from a separatrix crossing and revealed the symmetry breakings associated to it. The experimental and numerical results turn out to be in pretty good agreement and the analytical models predict accurately the observations, especially with the perturbative finite-gap theory.

Chapter 7

Modulation instability and FPUT recurrences in topographic fibers

Outline of the current chapter

7.1 Modulation instability in dispersion oscillating fibers **102**
7.1.1 Introduction to fiber diameter modulation in nonlinear optics 102
7.1.2 Linear regime of MI in DOFs 103
7.1.3 Nonlinear regime of MI in DOFs 106
Concept of frequency gain shift in DOF 107
FPUT recurrences in DOF 108
7.2 Demonstration of the nonlinear MI stage in DOFs **109**
7.2.1 Fiber characterization 109
7.2.2 Experimental setup for the gain shift observation 110
7.2.3 Experimental results of gain shift 112
7.2.4 Towards FPUT observation in DOFs 113
Chapter conclusions **115**

The experiments of the previous chapters have been performed with uniform fibers, exciting coherently the MI gain bands appearing in the anomalous dispersion regime. However, an additional degree of freedom in the system can allow to make unstable frequency bands that are predicted to be stable in the standard uniform configuration. Thus, from periodic variations of the fiber GVD, induced by the modulating of the fiber

diameter, parametric gain bands originate even in the normal GVD regime [97]. In this chapter, we will investigate MI and FPUT recurrences associated to the GVD modulation in dispersion oscillating fibers (DOFs). Especially, we will demonstrate the shift of the optimal gain outside of the parametric gain band in the weakly nonlinear MI regime. In a first section, we will introduce the analytical background associated to MI in DOFs through both the linear and the nonlinear MI regimes. In a second section, MI in DOFs will be investigated experimentally in a custom drawn fiber. We will especially highlight an instability band which differs from the linear parametric band in the highly nonlinear regime of MI, revealing a frequency shift of the maximum parametric gain.

7.1 Modulation instability in dispersion oscillating fibers

7.1.1 Introduction to fiber diameter modulation in nonlinear optics

On one hand, the idea to modulate the fiber dispersion along the propagation is not new. Indeed, it was proposed in [168] to decrease the GVD along the fiber length to compensate for the solitons broadening induced by the losses. It was experimentally validated few years later in [169–171]. This idea was later taken up in the context of supercontinuum generation. A tapered PCF was then fabricated to extend the broadening limit to the ultra-violet region [172]. On the other hand, the telecommunications networks are naturally periodically modulated from the multiple amplification stages. It paved the way to investigate the nonlinear effects occurring in long periodicity systems (of the order of kilometers). While, soliton distortion compensation was also demonstrated by means of dispersion managed transmission lines [173, 174], it was predicted the existence of network periodicity dependent MI in [175] through regularly spaced amplifiers and in [176] through GVD periodic changes. The periodicity of the system induces a quasi-phase matching (QPM) relation at the origin of additional parametric gain bands. While MI only exists in the anomalous dispersion regime for uniform fibers, this additional degree of freedom allows MI to also occur in the normal dispersion regime. It was first observed from a power periodicity in a recirculating loop in [177] and from birefringence periodicity in fibers in [178, 179]. In our laboratory, it was also investigated through GVD sine modulated PCFs in [96, 180], referred in the following as DOFs and illustrated in Fig. 7.1, or through a passive fiber cavity made of two different GVD fiber pieces in [181].

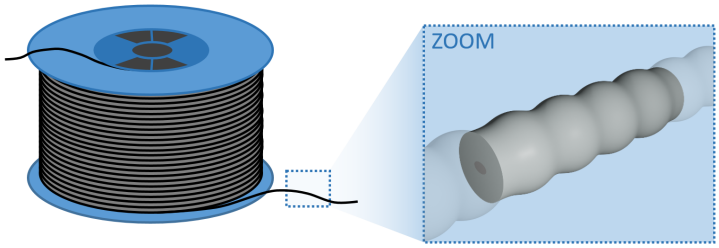

Figure 7.1: Schematic of a DOF span.

7.1.2 Linear regime of MI in DOFs

In this part, we remind the main concepts of MI process in a DOF [97], similarly to what we presented in uniform fibers. We consider the NLSE from Eq. 1.10 but with a variable GVD profile along the fiber length such as:

$$\beta_2(z) = \beta_{2,avg} + \beta_{2,mod}(z) \tag{7.1}$$

where $\beta_{2,avg}$ is the average GVD value and $\beta_{2,mod}(z)$ is the modulation around the average value. In all that follows, we will consider a sinusoidal dispersion profile, such as:

$$\beta_{2,mod}(z) = \beta_{2,amp} sin\left(\frac{2\pi}{Z}z + \phi_0\right) \tag{7.2}$$

where $\beta_{2,amp}$ is the amplitude of the GVD modulation, Z is the oscillation period and ϕ_0 is the initial phase shift of the fiber modulation. We assume that the nonlinear coefficient γ remains constant with the oscillations of the fiber diameter. It is fair according to experiments realized in weak dispersion regimes, with a DOF exhibiting 10% of diameter fluctuations, where the GVD variations completely dominated the nonlinear coefficient ones [97]. We can then derive the QPM relation:

$$\beta_{2,avg}\Omega^2 + 2\gamma P_0 = \frac{2m\pi}{Z} \tag{7.3}$$

where P_0 is the power of the CW background, Ω is the perturbation frequency and m is an integer. Then, contrary to uniform fibers where only two lobes are unstable, there are a priori an infinite number of parametric MI bands in DOFs. The MI gain spectra for uniform and topographic fibers, in normal and anomalous average dispersion regimes are displayed in Fig. 7.2. The numerical simulations are performed using the segmentation method, as described in [97] and inspired from [182]. We report the fiber dispersion profiles in Fig. 7.2. (a) and the corresponding spectra are plotted in Fig. 7.2.

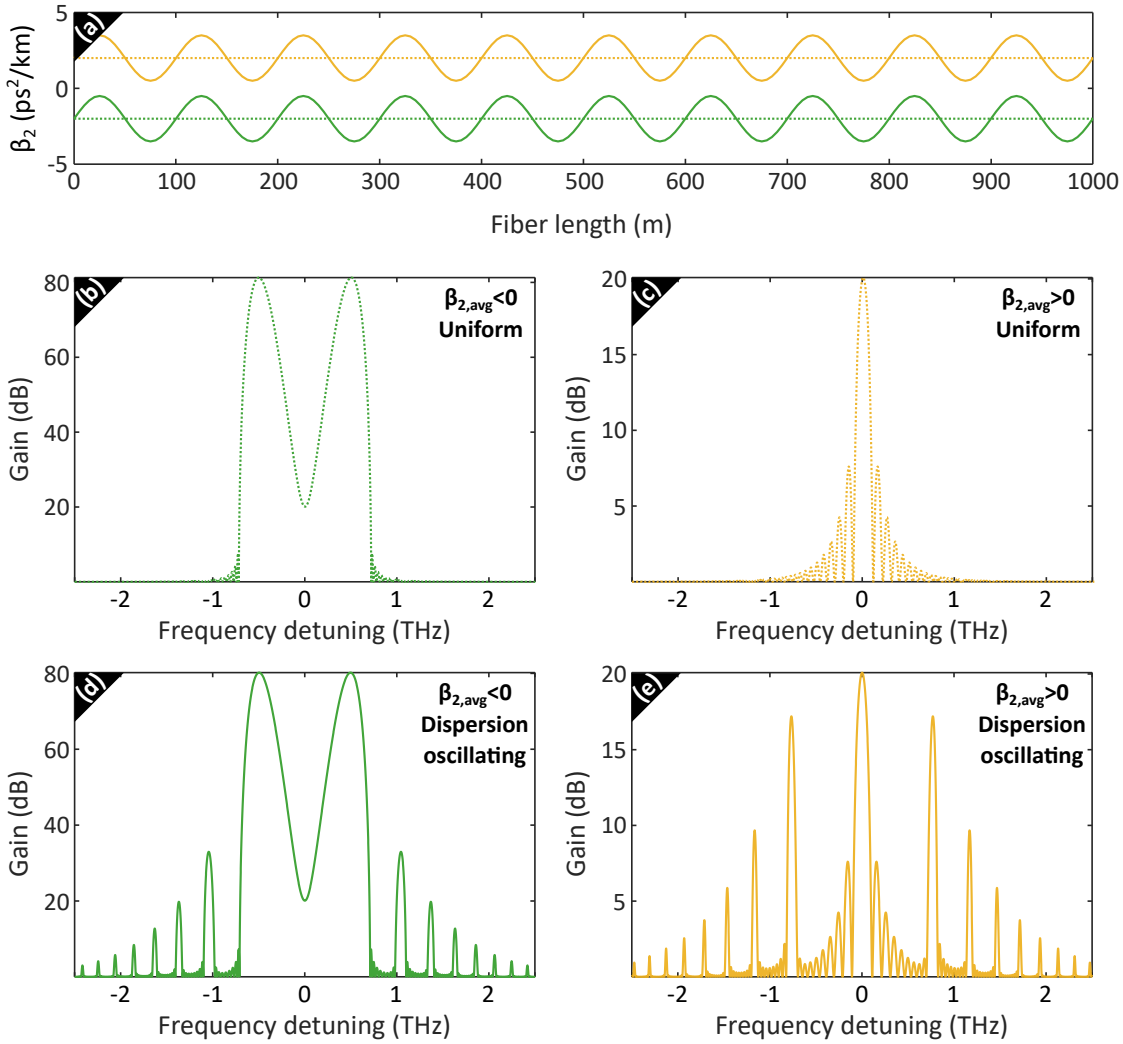

Figure 7.2: (a) Longitudinal evolution of the GVD. Fiber output spectra for (a) a uniform fiber in the anomalous GVD regime, (b) a DOF in the anomalous regime, (c) a uniform fiber in the normal regime and (d) a DOF in the normal regime. Parameters: $\beta_{2,avg} = \pm 2$ ps^2/km, $\beta_{2,amp} = 0$ or 1.5 ps^2/km, $\gamma = 5$ W^{-1}km^{-1}, $P_0 = 2$ W, $L = 1$ km, $Z = 100$ m. The spectra colors and line styles correspond to the GVD profiles in (a).

(b-e). The upper ones, in Fig. 7.2. (b) and (c), correspond to MI within an uniform fiber for $\beta_2 = \beta_{2,avg} = -2$ (anomalous regime) and 2 ps^{2}km^{-1} (normal regime) respectively. In this case, the unstable frequency is made of two symmetric sidelobes with respect to the pump frequency for the anomalous dispersion regime while there isn't any MI in the normal regime. On the lower panel, in Fig. 7.2. (d) and (e), we display the spectra with the same $\beta_{2,avg}$ as in the previous case but with a sine GVD modulation, with a

1.5 ps^2km^{-1} of amplitude modulation ($\beta_{2,amp}$) on 100 m periods (Z). In this case, we see additional side lobes compared to the uniform case. In the anomalous dispersion regime, these bands are added to the conventional MI ones (for $m = 0$ in Eq. 7.3) while in the normal regime, only these parametric bands remain (for $m \neq 0$ in Eq. 7.3). Looking at the relative evolution of the parametric gain bands, we notice that the gain drastically decreases with the order of the band m. The evolution of the spectrum in Fig. 7.3. (e) is studied by varying the GVD modulation parameters, $\beta_{2,avg}$, $\beta_{2,amp}$ and the modulation period Z, in Fig. 7.3. (a), (b) and (c) respectively. In Fig. 7.3. (a), the average GVD

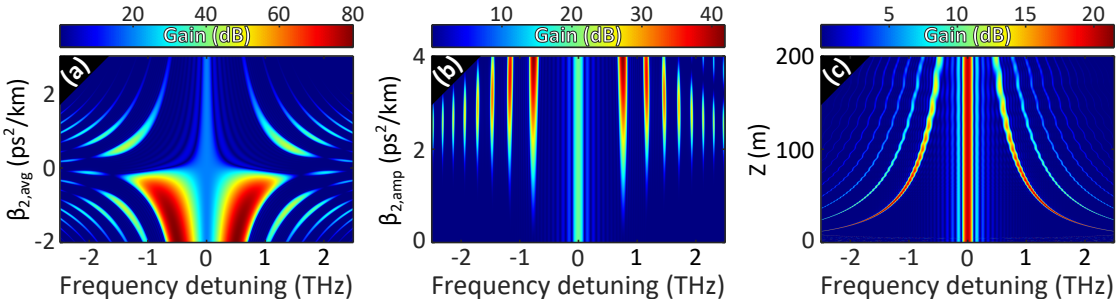

Figure 7.3: Evolutions of the fiber output spectrum as a function of (a) the average GVD, (b) the GVD modulation amplitude and (c) the modulation period. The parameters of the reference configuration are $\beta_{2,avg} = 2$ ps^2/km, $\beta_{2,amp} = 1.5$ ps^2/km, $\gamma = 5$ $W^{-1}km^{-1}$, $P_0 = 2$ W, $L = 1$ km, $Z = 100$ m.

varies from $\beta_{2,avg} = -2$ (anomalous) to 3 ps^2km^{-1} but keeping $\beta_{2,amp}$ and Z constant to 1.5 ps^2km^{-1} and 100 m respectively. We notice that it strongly modifies the MI bands frequencies, as expected from the QPM relation in Eq. 7.3, but also the associated gains. Note that in the anomalous dispersion regime, the amplitude of the parametric gain corresponding to a perfect phase-matching ($m = 0$) is always higher than the one from a QPM ($m \neq 0$). In Fig. 7.3. (b), the GVD modulation amplitude varies from $\beta_{2,amp} = 0$ to 4 ps^2km^{-1} and we keep the other parameters fixed to $\beta_{2,avg} = 2$ ps^2km^{-1} and $Z = 100$ m. The bands remain centered around the same phase-matching frequencies whatever the value of $\beta_{2,amp}$ is. It is expected from Eq. 7.3, as the GVD modulation amplitude doesn't intervene in the phase-matching. By increasing $\beta_{2,amp}$, the gain of all the MI bands also increases, up to $\beta_{2,amp} = 2.5$ ps^2km^{-1} where a more complex evolution of the gain bands is observed. For high values of modulation amplitude, the system becomes more complicated. Its behavior is investigated in [183], but this is out of the scope of the present study for which moderate $\beta_{2,amp}$ will be considered. In Fig. 7.3. (c), we vary the modulation period from $Z = 0$ to 200 m while keeping $\beta_{2,avg} = 2$ ps^2km^{-1} and $\beta_{2,amp} = 1.5$ ps^2km^{-1}. We notice that longer Z is, closer to the pump frequency are the

MI bands (as expected from Eq. 7.3) and smaller are their relative gain values. We also observe oscillations of the gain by increasing the modulation period. Indeed, the fiber length isn't necessarily a multiple of Z and the gain is modulated along the fiber length (see Fig. 7.4 for instance and [97] for more details), the output gain from the parametric process oscillates then according to Z. Of course, the GVD profile of the fiber doesn't have to be necessarily modulated by a sine (which is the easiest for the drawing process from a single preform) but it can be modulated with other periodic shapes, triangular or square for example. It doesn't modify the position of the side lobes but affects the parametric gain values [97].

7.1.3 Nonlinear regime of MI in DOFs

In this section, we will illustrate the main characteristics of the nonlinear regime of MI in DOFs through simple numerical simulations. Similarly to what we did in the previous chapters, it is possible to modulate the optical plane wave with a weak sine wave whose frequency is phase matched to the first-order ($m = 1$) parametric gain bands. We display an example of the initial excitation spectrum in Fig. 7.4. (a). The QPM equation in

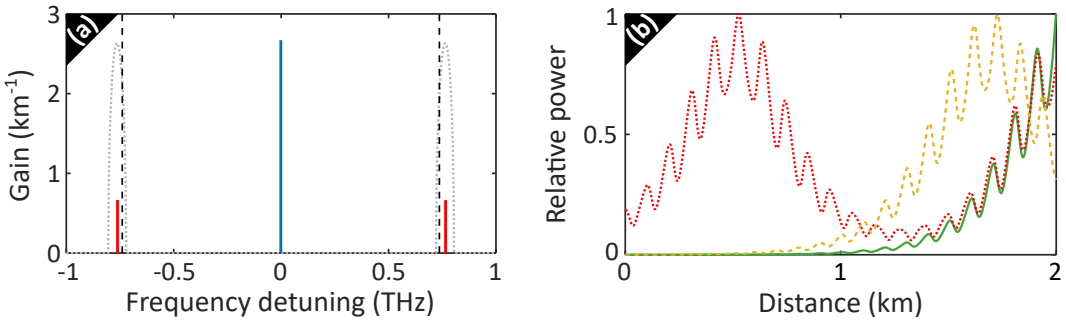

Figure 7.4: (a) Input spectrum with the pump (blue line), the signal/idler pair (red lines), the first band of parametric gain (dotted grey line) and the QPM frequency (dashed black line). (b) Evolutions of the signal power along the fiber length for $\frac{P_s(z=0)}{P_p(z=0)} = -50$ dB (solid green line), -40 dB (dashed orange line) and -13 dB (dotted red line). Parameters: $\beta_{2,avg} = \pm 2$ ps^2/km, $\beta_{2,amp} = 1.5$ ps^2/km, $\gamma = 5$ W^{-1}km^{-1}, $P_p(z = 0) = 2$ W, $L = 2$ km, $Z = 100$ m.

Eq. 7.3 predicts a solution at $f = 737$ GHz, in good agreement with the theory from the Floquet analysis (bands in dotted grey lines). If the wave modulation amplitude is weak enough, the amplification of the perturbation remains in the linear regime. In Fig. 7.4. (b), we report the relative power evolution along the distance of a sideband initially 50 dB below the pump (solid green line). The power follows an exponential curve, as

the pump saturation remains negligible, on which DOF characteristic oscillations are superimposed. The system remains in the linear MI stage, which can be accurately described using the segmentation method (used in the previous section) or the Floquet analysis as in [176]. If we increase the perturbation amplitude such as $\frac{P_s(z=0)}{P_p(z=0)} = -40$ dB (dashed orange line in Fig. 7.4. (b)), the pump saturation is no longer negligible. The sideband power starts to decrease from $z = 1.7$ km meaning that the energy transfers are reversed, as for FPUT in uniform fibers. The system follows a weakly nonlinear stage of parametric amplification. When the modulation amplitude is increased even more, up to $\frac{P_s(z=0)}{P_p(z=0)} = -13$ dB (dotted red line in Fig. 7.4. (b)), the perturbation amplification exhibits a periodic fashion of growth and decay cycles. The system evolves according to a highly nonlinear MI stage and reveals a FPUT recurrences like behavior.

Concept of frequency gain shift in DOF

The nonlinear stage of parametric amplification requires a much more complex theoretical approach to be predicted. An analytical method was proposed in [184] by means of mode truncations and averaging methods, in collaboration with S. Trillo. It revealed that, in the weakly nonlinear MI regime (higher perturbation amplitudes), a new instability band appears with a maximum gain which can even be located outside of the predicted linear parametric gain band. This feature is highlighted with a numerical study, whose results are displayed in Fig. 7.5. The left panel corresponds to a very small perturbation, with a power 50 dB below the pump. The spectrum of the initial excitation is illustrated in Fig. 7.5. (a) and the fiber output gain (solid green line) in Fig. 7.5. (c). In this case, the gain curve follows exactly the one calculated by the segmentation method (dashed black line) and fitting the maximum gain predictions of the Floquet analysis (dotted grey line). It confirms what was concluded for Fig. 7.4, the system is perfectly described by the linear MI stage. The numerical results for a much higher perturbation power, 13 dB below the pump, are displayed in the right panel. In this case, the fiber output gain in Fig. 7.5. (d) is frequency shifted from the linear stage predictions. Indeed, the maximum gain is around $f_m = 820$ GHz, while it is located at $f_m = 770$ GHz according to the segmentation method (dashed black line). It is even located beyond the cutoff frequency $f_c = 805$ GHz predicted by the Floquet analysis. This gain is characteristic of a system evolving in a weakly nonlinear MI regime. We also notice that the maximum gain value is much lower than in the linear stage, as a consequence of the pump saturation. A very similar feature was observed with MI from birefringent fibers in [95]. Indeed, they also revealed a new instability band in the large-signal regime compared to the usual

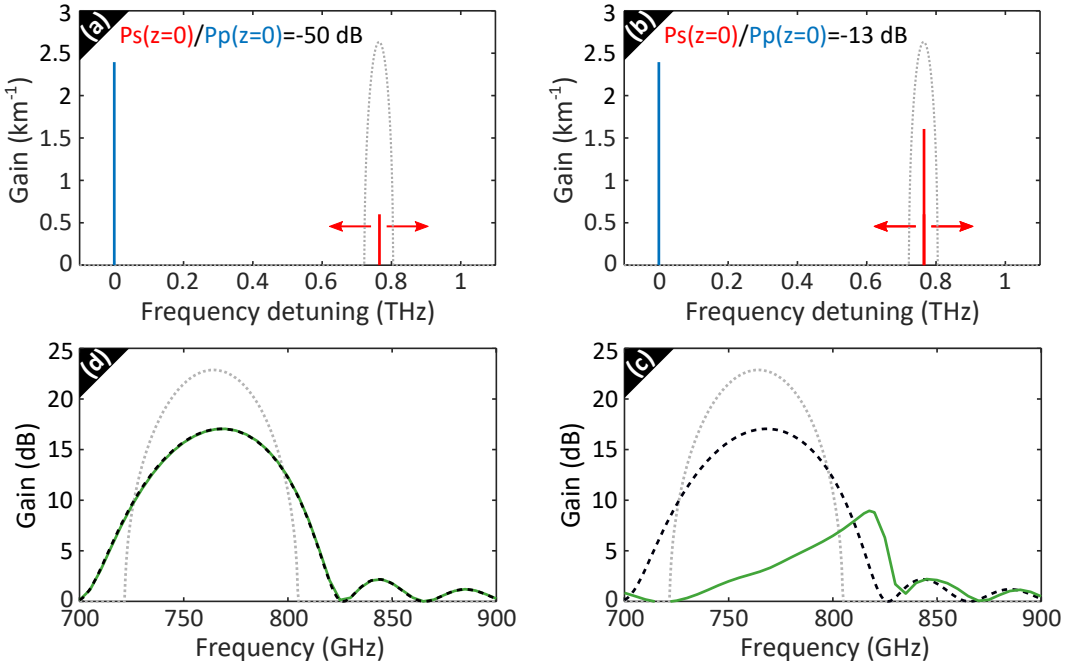

Figure 7.5: (a-b) Input spectrum with the pump (blue line), the signal (red line) and the first band of parametric gain (dotted grey line). (c-d) Evolution of the fiber output gain (solid green line) as a function of the modulation frequency. The gain bands from the segmentation method (dashed black line) and the Floquet analysis (dotted grey line) are superimposed. Left panel: $\frac{P_s(z=0)}{P_p(z=0)} = -50$ dB. Right panel: $\frac{P_s(z=0)}{P_p(z=0)} = -13$ dB. Parameters: $\beta_{2,avg} = \pm 2$ ps^2/km, $\beta_{2,amp} = 1.5$ ps^2/km, $\gamma = 5$ W^{-1}km^{-1}, $P_p(z=0) = 2$ W, $L = 1$ km, $Z = 100$ m.

linear MI band in a birefringent medium [94, 185].

FPUT recurrences in DOF

In the highly nonlinear MI stage, reached with either a sufficient fiber length or a high amplitude perturbation, they also predict in [184] the emergence of a FPUT like dynamics. A numerical example of the nonlinear MI stage dynamics in a DOF with a normal average GVD is displayed in Fig. 7.6. Compared to Fig. 7.5, we observe the dynamic on a much longer fiber. The configuration is also almost identical to the one in Fig. 7.4, except that the modulation frequency is set to $f_m = 802$ GHz because of the gain shift to benefit from a conversion efficiency maximum. In Fig. 7.6. (a), the longitudinal power evolutions of the pump (blue line) and the signal (red line) reveal a similar dynamic to the one encountered in uniform fibers with a growth and decay

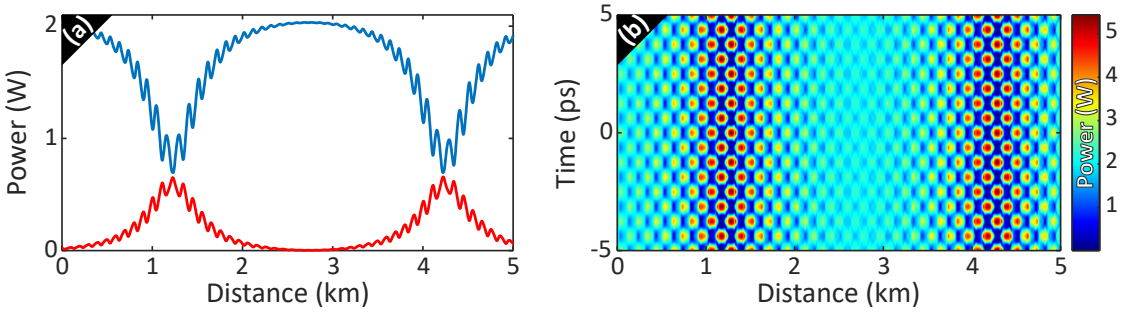

Figure 7.6: Coherently-driven MI in DOFs. (a) Power evolution of the pump (solid blue line) and signal (solid red line) along the fiber length. (b) Power space-time profile. Parameters: $\beta_{2,avg} = \pm 2$ ps^2/km, $\beta_{2,amp} = 1.5$ ps^2/km, $\gamma = 5$ W^{-1}km^{-1}, $L = 1$ km, $Z = 100$ m, $P_p(z=0) = 2$ W, $\frac{P_{s,i}(z=0)}{P_p(z=0)} = -20$ dB, $f_m = 802$ GHz and $\Delta\Phi(z=0) = \frac{\pi}{2}$.

periodicity of almost 3 km. However, in addition to the long scale periodicity, a short scale periodicity of 100 m is superimposed which corresponds perfectly to the GVD modulation period. In the time domain, in Fig. 7.6. (b), this short space scale periodicity leads to a π-shift at each GVD period and to a chess board like pattern (which is not related to the initial relative phase value).

7.2 Demonstration of the nonlinear MI stage in DOFs

7.2.1 Fiber characterization

As explained previously, the sine modulation of the GVD profile is obtained by shaping correspondingly the fiber diameter. The drawing of the DOF is realized by the FiberTech Lille platform of the PhLAM by following specific setpoints. We designed from numerics a fiber which should meet several criteria. It should enable to observe the gain shift and the FPUT recurrences described before. Then, the entire fiber should be long enough to excite the highly nonlinear MI regime but short enough so that the fiber attenuation is not detrimental. The diameter modulation should also be long enough to manage to record the slight oscillations induced by the DOF geometry. Finally, the first-order parametric bands should be located no further than a few hundred of GHz from the pump, to allow an easier coherent excitation. After several drawing tries, we obtained a fiber with suitable parameters. It is made of a PM preform which is drawn with a sine diameter varying from 113 μm to 123 μm, as shown from the measurements in Fig. 7.7. (a), into a $L = 1.72$ km long DOF with a $Z = 200$ m oscillation period. From the OTDR trace in Fig. 7.7. (b), we measure the fiber attenuation α(@1550 nm) = 1.2

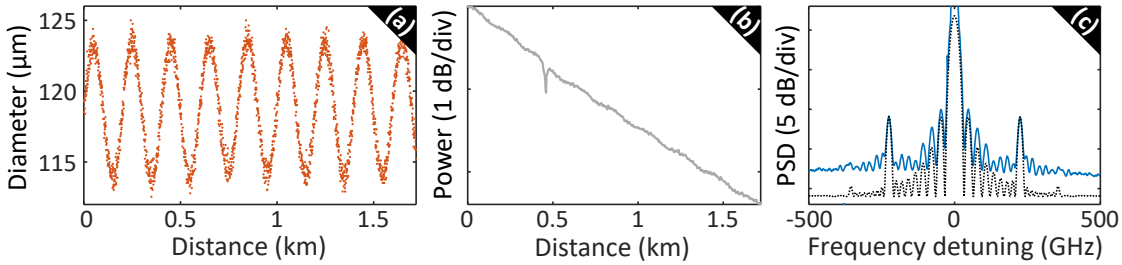

Figure 7.7: (a) Measured data of the fiber diameter. (b) OTDR trace. (c) Recorded fiber output spontaneous spectra (solid blue line) with the Raman pump switch on. The numerical gain spectrum from the segmentation method is also superimposed (dotted black line).

dB/km. We also notice a drawing defect around 450 m, but we neglected its impact in the future experiments. To determine the average and the amplitude dispersion of the DOF, we performed a simple spontaneous MI experiment. By numerically calculating the parametric instability gain spectrum from the segmentation method, we adjust the parameters as the average dispersion to $\beta_{2,avg} = 9.5$ ps^2/km, the amplitude dispersion to $\beta_{2,amp} = 3.1$ ps^2/km and the nonlinear length to $L_{NL} = 119$ m ($\gamma P_0 = 8.4$ km^{-1}) to maximize the agreement with experiments. It is also possible to retrieve $\beta_{2,avg}$ value using the QPM relation in Eq. 7.3. Due to the linear attenuation and so the non constant pump power, we are not able to calculate it with only the frequency of the first-order parametric band. However, by measuring the second order parametric band frequency, we can combine the QPM relations for $m = 1$ and $m = 2$. In this way, we recover the average GVD value without any γP_0 dependence, which is consistent with the first value. We also estimate the efficiency of the Raman compensation scheme in this configuration with the spectrum in Fig. 7.7. (c). By applying the maximum power of the Raman pump ($P_R = 600$ mW), we are able to reduce the linear attenuation to an effective value of α_{eff}(@1550 nm) = 0.25 dB/km. We numerically checked that a higher Raman pump power would enable an almost perfect compensation of the losses, but we didn't have such a laser at the laboratory. This DOF will be used for the experimental work presented in the following and the estimated parameters will help to simulate precisely the system and to perform a numerical comparison.

7.2.2 Experimental setup for the gain shift observation

In this experiment, we study the evolution of the gain shift induced by the increase of the signal amplitude, described in Fig. 7.5. To this end, we implemented a setup to measure the parameteric gain with a pump-probe experiment. It is schematically

detailed in Fig. 7.8. The CW main laser is similarly shaped to the experimental setup

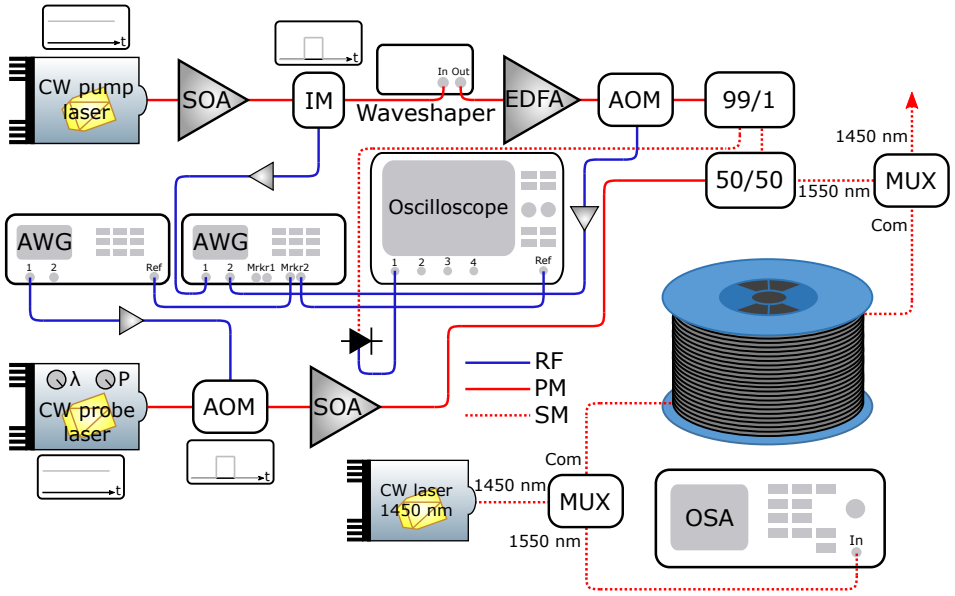

Figure 7.8: Sketch of the experimental setup.

described in Chapter 3, except that the phase modulation stage is removed. Indeed, the electro-optic bandwith is limited to 40 GHz with these Lithium Niobate phase modulators and doesn't allow to probe MI bands with hundreds of GHz to few THz detuning from the pump. A secondary CW tunable and power adjustable laser [Keysight 81640A] is then used as the probe. It is time shaped using the additional shaping stage, previously introduced in Chapter 3 as (14), using an AO modulator triggered from a synchronized AWG. It is also amplified with a SOA before being combined with the pump laser through a 50/50 coupler. The pulse train is then injected inside the DOF. As we have seen previously, the fiber linear attenuation is not negligible despite the short total fiber length as we measured it at α(@1550 nm) = 1.2 dB/km (OTDR measurement in Fig. 7.7). In addition to a weaker total gain due to progressive attenuation of the pump, we expect, as predicted by simulations, the blurring of the parametric gain bands. Indeed, as the phase-matching condition depends directly on the power (Eq. 7.3), an attenuation of the power leads to the shift of the gain maximum frequency and the broadening of the gain band. To limit this effect which can be detrimental for clear observations, we keep implemented the Raman pump (more details in Chapter 3) to best compensate for the fiber losses. By increasing the Raman power to the maximum that the pump can deliver, we are able to reduce largely the losses suffered by the signal during the propagation. Indeed, we estimate the effective attenuation of the fiber in

this case to α_{eff}(@1550 nm) = 0.25 dB/km, reducing the total losses experienced during the propagation from 2.15 dB to 0.43 dB and shifting the first-order parametric bands closer to the pump by around 9 GHz. At the fiber end, the spectrum and especially the probe laser relative amplitude are recorded with an OSA to calculate the on/off gain. Such recordings are automated with the variation of both the probe laser wavelength to sweep it well over the parametric gain spectral span, and the probe laser power. The automation is essential for these experiments as it frees the experimenters from the repetitiveness of the recordings and drastically speeds up the acquisitions to limit the impact of polarization and power instabilities. Moreover, the resulting 2D plots give an overview of the process in a $(f_m, P_s(z = 0))$ plane providing a detailed observation of the system dynamic.

7.2.3 Experimental results of gain shift

The gain experienced by the probe from the parametric resonance is measured over all the first sidelobe ($m = 1$), from 200 to 260 GHz, and for signal to pump ratios varying from −38 to −10 dB. The gain is calculated between the power of the probe experiencing MI gain (on) and the power of the probe outside any parametric gain band (off). We ensure that the non-phase matched FWM with the reference probe (off) is negligible enough to consider the calculated gain as the on/off gain. The results are summed up in the 2D plot in Fig. 7.9. (a). At low power ratios (up to −25 dB), there isn't any shift of the gain band as it remains centered around $f_0 = 227$ GHz. It is well predicted by the linear MI regime, as confirmed by the segmentation method gain band FWHM (dotted white lines) and cutoff frequencies, the 0 dB gain frequencies in Fig. 7.5 (dashed white lines). At higher power ratios, we see a spectral shift of the gain maximum, which is even outside of the predicted band FWHM from −18 dB and even beyond the upper cutoff frequency from −13 dB. Such features are highlighted by plotting the gain curves for specific values of signal to pump ratio, for −35 dB (blue line), −14.9 dB (orange line) and −10 dB (yellow line), in Fig. 7.9. (c). We report a 25.8 GHz shift for a power ratio of −10 dB. These experimental results are compared to data from the numerical integration of the NLSE in Fig. 7.9. (b) and (d). The agreement between experiments and numerics is very good as the numerical gain follows the exact same evolution with the signal to pump ratio as in experiments. A small gap is observed by looking at the threshold value for the gain band shift, but the concordance remains very convincing. To get a deeper insight of the process, we report in Fig. 7.10 the evolution of few specific data as a function of the power ratios: the frequency detuning of the gain maximum,

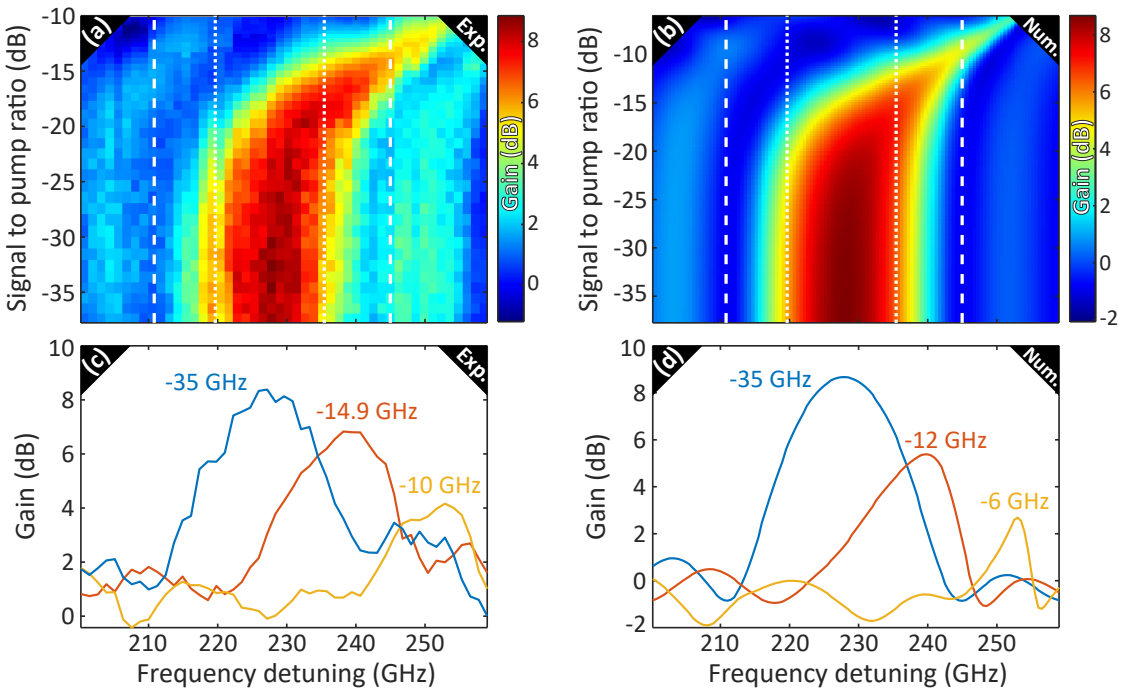

Figure 7.9: (a-b) Evolution of the gain experienced by the probe from the parametric process as a function of the pump-probe frequency detuning and the power ratio. (c-d) Evolutions of the gain for specific values of signal to pump power ratios. Left panel: experimental data. Right panel: data from NLSE numerical integration. The vertical dotted and dashed lines account for the FWHM and the cutoff frequencies of the gain band respectively, predicted by the segmentation method.

the corresponding gain and the maximum conversion efficiency. We notice a very good overall agreement between the experimental (crosses) and the numerical data (dotted lines).

7.2.4 Towards FPUT observation in DOFs

By increasing the nonlinearity into the highly nonlinear MI regime, it should be interesting to observe for the first time FPUT recurrences in a normal dispersion regime, as presented in Fig. 7.6. However, such investigations require specific evolutions of the experimental setup, which could not be implemented during this thesis work due to a lack of time. Nevertheless, we introduce them to pave the way of future experiments. The parametric gain bands of the actual DOF are located 230 GHz away from the pump. However, as the bandwidth of the electro-optic modulators doesn't exceed 40 GHz, the actual single phase modulator stage is insufficient to excite coherently the DOF

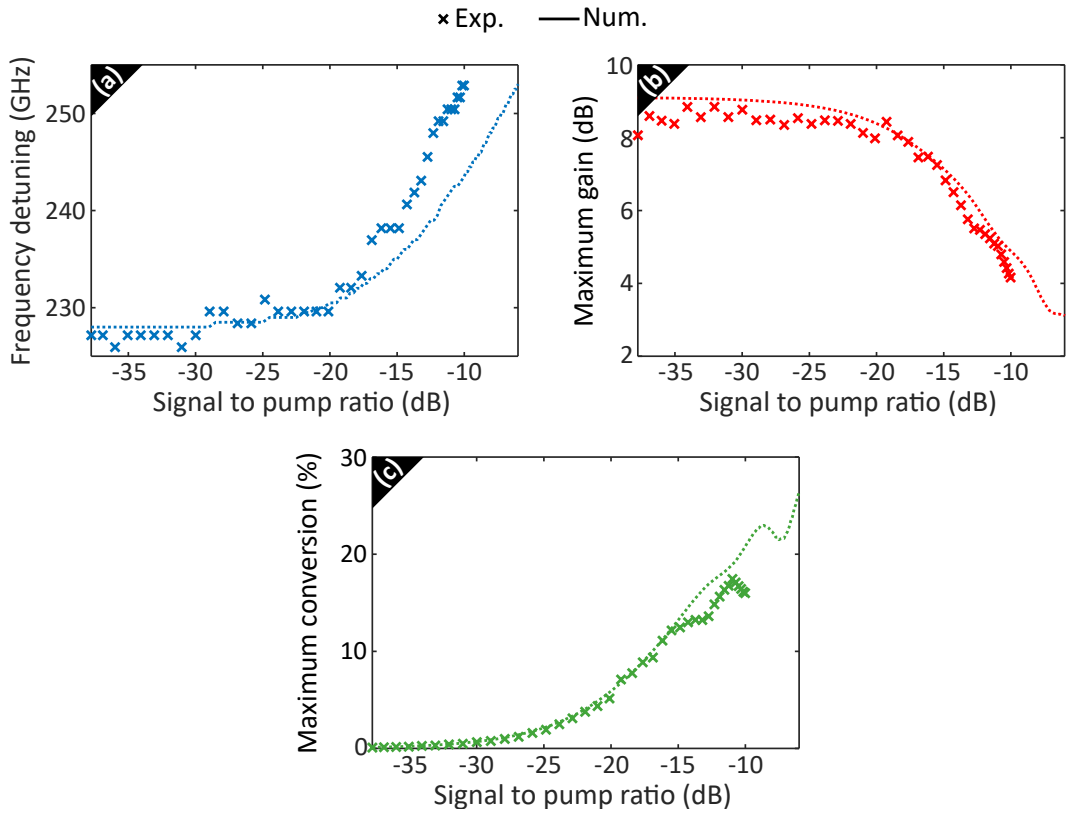

Figure 7.10: Evolutions of (a) the maximum gain frequency, (b) the maximum gain value and (c) the maximum conversion efficiency as a function of the signal to pump power ratio. Crosses: experimental data. Dotted lines: numerical data.

MI bands. The generation stage has to be revised to generate few hundreds of GHz wide frequency combs, with cascaded modulators as in the context of electro-optics frequency combs [186]. It would also involve to upgrade the local oscillator in parallel since it is solely broadened with a single intensity modulator. In addition, the actual DOF length of 1.72 km would limit the observation to a half recurrence or maybe one FPUT recurrence (depending on the initial conditions). A 4 or 5 km long fiber would be more optimal for FPUT investigations. Finally, it would require to improve the loss compensation scheme, especially with longer fiber spans, simply with a higher power Raman pump.

Chapter conclusions

In this chapter, we introduced the emergence of MI and FPUT recurrences in the normal GVD regime through topographic fibers. The main result reported is the observation of a frequency shift of the instability band in the weakly nonlinear MI regime. We first analytically presented the parametric instability process both in the linear (exponential growth) and in the nonlinear stages (gain shift and FPUT recurrences). Then, we presented and characterized the DOF drawn by FiberTech Lille, a 1720 m long fiber with a 200 m oscillation period, and we detailed the experimental setup. Finally, from the experimental studies in the weakly nonlinear MI regime, we highlighted the shift of the parametric amplification instability band, with a maximum gain even beyond the unstable band from the linear theoretical predictions.

Conclusion

In this thesis, we studied the nonlinear stage of modulation instability in optical fibers, which leads to a periodic breather dynamics known as Fermi-Past-Ulam-Tsingou recurrences. These recurrences were experimentally investigated in depth, up to their limits, either to demonstrate analytical solutions of the NLSE and specific features of MI or to study the evolution and stability under parameters variations. Thanks to a constantly evolving and improved experimental setup, we managed to perform non-invasive distributed measurements in both intensity and phase of the main spectral components in long fiber spans. It was made possible by a heterodyne optical time domain reflectometer, combined with an active loss compensation through a backward pumping Raman amplifier. It allowed us to obtain the nonlinear dynamic along the propagation distance very efficiently but also to tune easily the fiber input conditions of the nonlinear optical beam. The main results, obtained from this experimental setup and presented in this manuscript, are summarized hereunder:

- First, we validated experimentally analytical solutions derived from the NLSE and predicting the appearance of doubly periodic breathers structures. The optimization loss compensation scheme allowed to obtain a quasi-transparent optical fiber on many nonlinear lengths, which is essential to mimic an integrable system. We demonstrated the first-order doubly periodic solutions of the NLSE [51, 52], which are the only ones to predict the appearance of FPUT recurrences in focusing cubic media [46]. From these solutions was predicted an "extraordinary" MI gain i.e. the existence of gain beyond the conventional MI band [52] that we confirmed experimentally [47].

- We also pushed the setup to a maximum operating efficiency regarding the SNR and the loss compensation scheme to record the highest number of FPUT recurrences in fiber optics so far. We observed 4 recurrences from an outer orbit excitation and it increased up to almost 5 from an inner orbit excitation in a 18 km

long fiber [48]. Since the dynamic remained highly periodic and reversible in that case, we then forced the transition to the "thermalization state" by degrading the input signal [159]. By favoring the noise-driven MI growth at the expense of the seeded MI, we progressively revealed the transition to an irreversible thermalized regime which is accompanied by the recurrences break-up [49].

- Afterwards, we demonstrated the influence of a weak damping or forcing in the FPUT recurrences process. With a fine tuning of the backward Raman pump power, we were able to weakly under- or overcompensate for the fiber attenuation. In this way, we revealed loss and gain induced separatrix crossings and the corresponding multiple symmetry breakings [50], as predicted by the theoretical models (3WM model and perturbative finite-gap theory).

- Then, we investigated MI and FPUT recurrences in a fiber with a weakly oscillating dispersion in the normal regime, first from an analytical and numerical point of view. Then, we experimentally confirmed the analytical predictions of a new instability band in the weakly nonlinear MI regime [184]. Indeed, we revealed a shift of the parametric gain maximum, even outside of the predicted linear unstable band for sufficiently powerful perturbation amplitudes.

- Finally, we continued throughout the thesis to study the Raman loss compensation scheme and to investigate for a more efficient one. These results are reported in Appendices for the sake of clarity of the manuscript. We experimentally studied the backward Raman amplification of short pulses to reveal the pump saturation effects [53]. We also experimentally worked on time shaping of the Raman pump as a proof of concept towards actively compensated transparent optical fibers.

Of course, this work doesn't claim any kind of exhaustivity regarding the study of breathers and FPUT recurrences which could be possible with this experimental setup. On the contrary, this manuscript tends to open the way to further investigations and developments, some of them are presented thereafter:

- First, an interesting topic that could be addressed is the collision of breathers. It originates from the double seeding of the MI gain band i.e. with modulation frequencies $f_{m,1}$ and $f_{m,1}$ below the MI cutoff frequency f_C. It shouldn't be confused with the higher-order modulation instability, where one or several harmonics from the FWM between the pump and the seed are located within the MI gain band and studied in [147, 149, 150]. The collision of breathers has already been investigated

in the case specific case $f_{m,2} = 2f_{m,1}$ in [43, 132] and in the more general case in [121]. The latter is illustrated in Fig. 7.11 with space-time power diagrams from numerical simulations. The Fig. 7.11. (a) and (b) are obtained from the three

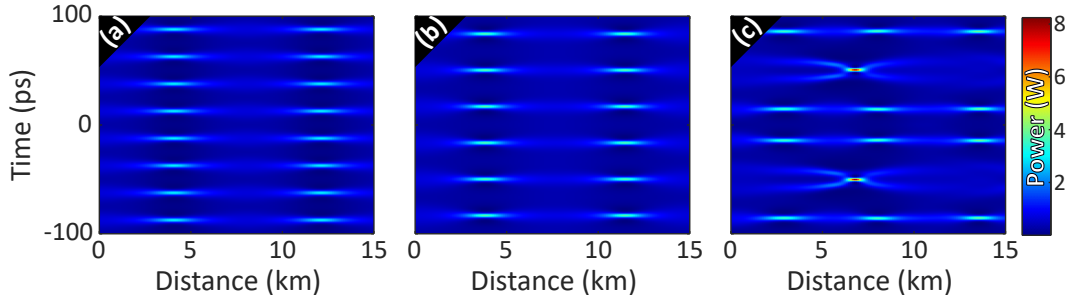

Figure 7.11: Numerical space-time power diagrams for a single seed (a) $f_m = 40$ GHz and (b) $f_m = 30$ GHz, for a double seed (c) $f_{m,1} = 30$ GHz and $f_{m,2} = 40$ GHz. Parameters: $\beta_2 = -21$ ps^{2}km^{-1}, $\gamma = 1.3$ W^{-1}km^{-1}, $P_p(z = 0) = 500$ mW, $P_s(z = 0) = 5$ mW.

classical waves input, with a modulation frequency of $f_m = 40$ GHz and $f_m = 30$ GHz respectively. The Fig. 7.11. (c) is obtained by combining the two previous modulation i.e. with $f_{m,1} = 30$ GHz and $f_{m,2} = 40$ GHz. We notice that around $T = \pm 50$ ps the breathers are getting closer until they collide at $Z = 7$ km. It results from these collisions, some very high intensity pulses. Indeed they reach peak powers of 8 W, to be compared with 3 W for regular breathers. One could then study the evolution of the collided breathers, regarding the peak power and the periodicity, as a function of either the frequency shift or the power imbalance between both modulations. It would require to experimentally implement a third or even a fourth detection channel to get the evolution of all the input five or even seven waves to obtain a high resolution insight of the temporal dynamic.

- Then, in the continuity of the work presented in Chapter 7, it should be interesting to investigate for FPUT excitation in DOF, as theoretically highlighted in [184] It could represent, to the best of our knowledge, the first observation of these recurrences in a normal dispersion regime. The Chapter 7 figure illustrating numerics of recurrences in DOF is displayed again in Fig. 7.12. As explained in 7, it would require to modify the generation stage to get a much wider frequency comb by means of modulators in series. It would also involve to draw longer DOF and to upgrade in parallel the local oscillator and the Raman pump.

- Finally, one might be interested to pursue and develop the Raman pulse time shaping to compensate even better for the fiber losses. Indeed, the first experimen-

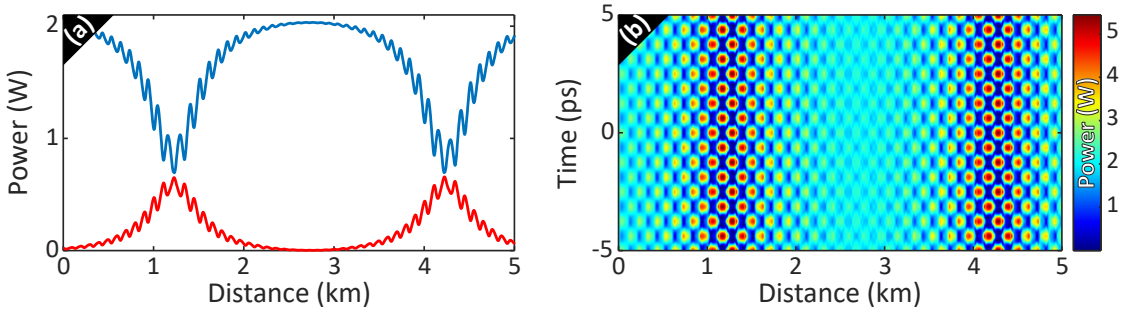

Figure 7.12: FPUT recurrences in DOF. (a) Power evolutions of the pump (solid blue line) and signal (solid red line) along the fiber length. (b) Power space-time profile. Parameters: $\beta_{2,avg} = \pm 2$ ps^2/km, $\beta_{2,amp} = 1.5$ ps^2/km, $\gamma = 5$ W^{-1}km^{-1}, $L = 1$ km, $Z = 100$ m, $P_p(z=0) = 2$ W, $P_s(z=0) = P_i(z=0) = 20$ mW, $f_m = 802$ GHz and $\Delta\Phi(z=0) = \frac{\pi}{2}$.

tal works on this topic, and presented in Appendix C, reveal promising results and then pave the way to reach fully transparent optical fibers. We display a numerical example of an optimized Raman pump pulse in Fig. 7.13. (a), leading to a transparent 50 km long fiber in Fig. 7.13. (b). To give an idea, it would allow

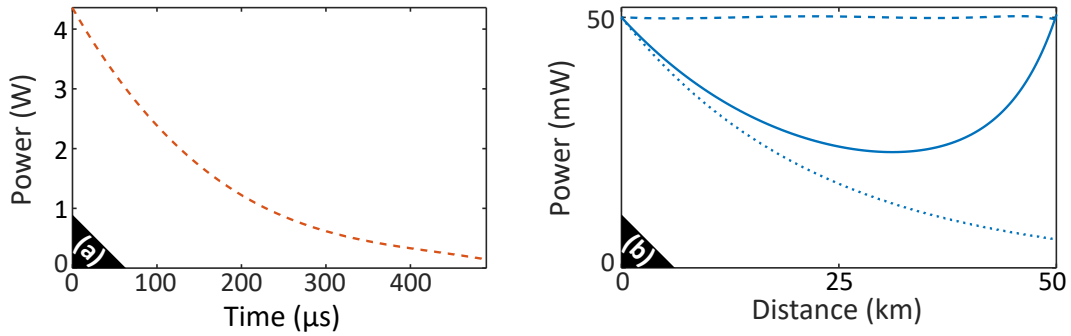

Figure 7.13: (a) Optimized Raman pulse shape. (b) Evolution of the power of the amplified signal with the pump shape in (a) (dashed line), a constant Raman pump power $P_R(z=L) = 610$ mW (solid line) and no Raman pump (dotted line).

to record from 10 to 12 FPUT recurrences and maybe to investigate on a larger scale periodicity with the super-recurrences. For a constant Raman pump power, we notice very significant losses in the fiber center part. Therefore, this ability to perfectly compensate for the losses on very long fibers opens up possibilities for fiber sensors for instance.

Appendix A

Analytical development of the first-order doubly periodic solutions of the NLSE

We report here the expressions of the first-order doubly periodic solutions of the NLSE. First derived in [51], they were developed again and their Fourier coefficients calculated in [52]. The expressions, which are detailed in the following, are extracted from [52]. The solutions of the dimensionless NLSE in Eq. 2.12 are in the form:

$$\Psi(\xi,\tau) = [Q(\xi,\tau) + i\delta(\xi)]e^{i\phi(\xi)} \tag{A.1}$$

where Q, δ and ϕ are real functions. The solutions are doubly periodic (periodic both in space ξ and time τ) and depend only on three parameters α_1, α_2 and α_3. They are classified in two types depending on the characteristics of the phase periodicity. For B-type solutions, the recurrences remain unshifted and the three parameters are real. For A-type solutions, the recurrences are π-shifted and α_1 is real while α_2 and α_3 are complex conjugates. The limit case between both types is the Akhmediev breather.

B-type solutions

The three parameters are real and $\alpha_3 > \alpha_2 > \alpha_1$. δ is defined as:

$$\delta(\xi) = \frac{\sqrt{\alpha_1\alpha_3}sn(\mu\xi,k)}{\sqrt{\alpha_3 - \alpha_1 cn^2(\mu\xi,k)}} \tag{A.2}$$

where the modulus of the Jacobian elliptical function is $m = k^2 = \frac{\alpha_1(\alpha_3-\alpha_2)}{\alpha_2(\alpha_3-\alpha_1)}$ and $\mu = 2\sqrt{\alpha_2(\alpha_3-\alpha_1}$. ϕ writes as:

$$\phi(\xi) = (\alpha_1+\alpha_2-\alpha_3)\xi + \frac{2\alpha_3}{\mu}\Pi(am(\mu\xi,k),n,k) \tag{A.3}$$

with $n = \frac{\alpha_1}{\alpha_1-\alpha_3}$, $\Pi(am(\mu\xi,k),n,k)$ is the incomplete elliptic integral of the first kind and $am(\mu\xi,k)$ the amplitude function [187]. And finally Q is defined as:

$$Q(\xi,\tau) = \frac{Q_D(Q_A-Q_C)+Q_A(Q_C-Q_D)sn^2(p\tau,k_q)}{(Q_A-Q_C)+(Q_C-Q_D)sn^2(p\tau,k_q)} \tag{A.4}$$

where the elliptic modulus is $m_q = k_q^2 = \frac{\alpha_2-\alpha_1}{\alpha_3-\alpha_1}$, $p = \sqrt{\alpha_3-\alpha_1}$ and Q_A, Q_B, Q_C and Q_D are:

$$Q_A = s\sqrt{\alpha_1-y}+\sqrt{\alpha_2-y}+\sqrt{\alpha_3-y} \tag{A.5}$$
$$Q_B = -s\sqrt{\alpha_1-y}-\sqrt{\alpha_2-y}+\sqrt{\alpha_3-y} \tag{A.6}$$
$$Q_C = -s\sqrt{\alpha_1-y}+\sqrt{\alpha_2-y}-\sqrt{\alpha_3-y} \tag{A.7}$$
$$Q_D = s\sqrt{\alpha_1-y}-\sqrt{\alpha_2-y}-\sqrt{\alpha_3-y} \tag{A.8}$$

with $y = \delta^2(z)$ and $s = sgn(cn(\mu\xi,k))$.

A-type solutions

α_3 is a positive real parameter while α_1 and α_2 are complex conjugates such as $\alpha_1 = \alpha_2^* = \rho + i\eta$ (ρ and η are real parameters). δ is defined as:

$$\delta(\xi) = \sqrt{\frac{\alpha_3}{2}(1-\nu)\frac{1+dn(\mu\xi,k}{1+\nu cn(\mu\xi,k)}}sn\left(\frac{\mu\xi}{2},k\right) \tag{A.9}$$

where $m = k^2 = \frac{1}{2}\left(1-\frac{\eta^2+\rho(\rho-\alpha_3)}{AB}\right)$, $\nu = \frac{A-B}{A+B}$, $\mu = 4\sqrt{AB}$, $A = \sqrt{(\alpha_3-\rho)^2+\eta^2}$ and $B = \sqrt{\rho^2+\eta^2}$. ϕ have the following expression:

$$\phi(\xi) = \left(2\rho+\frac{\alpha_3}{\nu}\right)\xi - \frac{\alpha_3}{\mu\nu}\left[\Pi(am(\mu\xi,k),n,k) - \nu\sigma\tan^{-1}\left(\frac{sn(\mu\xi,k)}{\sigma dn(\mu\xi,k)}\right)\right] \tag{A.10}$$

where $n = \frac{\nu^2}{\nu^2-1}$ and $\sigma = \sqrt{\frac{1-\nu^2}{k^2+(1-k^2)\nu^2}}$. The Q function writes as:

$$Q(\xi,\tau) = sb - c_+\frac{r+cn(p\tau,k_q)}{1+rcn(p\tau,k_q)} \tag{A.11}$$

with $s = sgn(cn(\frac{\mu\xi}{2}, k))$, $b = \sqrt{\alpha_3 - y}$, $r = \frac{M-N}{M+N}$, $p = \sqrt{MN}$, $M = \sqrt{(2sb + c_+)^2 + c_-^2}$, $N = \sqrt{(2sb - c_+)^2 + c_-^2}$, $c_\pm = \sqrt{2\left[\sqrt{(y-\rho)^2 + \eta^2} \pm (\rho - y)\right]}$ and $k_q = \sqrt{\frac{1}{2} + 2\frac{\rho - \alpha_3}{p^2}}$.

Appendix B

Short pulse Raman amplification

We initially wanted to verify that the gain experienced by our 50 ns pulses was constant on the all duration of the pulses. However we realized further experiments to investigate the pulse width dependence of a backward Raman pump saturation. The dynamics of both forward and backward pumping configurations are precisely described analytically in the CW regime [188]. In the pulsed case, solutions in the backward amplification regime are only found in a lossless system, either with a perturbative approach in [189] or analytically in [190]. In the latter, gigantic amplification of short pulses and pulse duration dependence of the gain are highlighted. Such a topic have experimentally been investigated concerning the pulses steepening in [191]. But no experimental study has revealed the pulse width dependence of the Raman amplification in an optical fiber system. The system of equations that rule the amplification by a counterpropagating Raman pump of a pulsed signal is:

$$\frac{\partial A_S}{\partial z} + \frac{1}{v_{g,S}}\frac{\partial A_S}{\partial t} = \frac{g_R}{2}|A_P|^2 A_S - \frac{\alpha_S}{2}A_S \tag{B.1}$$

$$-\frac{\partial A_P}{\partial z} + \frac{1}{v_{g,P}}\frac{\partial A_P}{\partial t} = \frac{\lambda_S}{\lambda_P}\frac{g_R}{2}|A_S|^2 A_P - \frac{\alpha_P}{2}A_P \tag{B.2}$$

We take benefit from the setup described in Chapter 3 to perform our experiments. The input signal is shaped into a train of square pulses with a peak power $P_S(z=0) = 25$ mW and with a tunable T_S duration. It is then injected in a 20.3 km long non-zero dispersion-shifted fiber, to get the 1550 nm signal in the normal dispersion regime and to prevent the appearance of modulation instability. The specifications of the fiber are $g_R = 0.49$ W^{-1}km^{-1}, $\alpha_S = \alpha(@1550\text{ nm}) = 0.2$ dB/km and $\alpha_P = \alpha(@1450\text{ nm}) = 0.28$ dB/km. The signal is amplified with the same backward pumping Raman scheme as the on described in Chapter 3. The pulses are recorded at the fiber end, with the Raman pump both on and off, with a photodiode and displayed on a oscilloscope. Then, we are able to measure the on-off energy gain at the fiber output from the recorded temporal traces. Such measurements are performed for several T_S values ranging from 10 ns to

4 μs to study the regime of the backward Raman pumping scheme as function of the signal pulse duration. We display this gain evolution in the upper panel of Fig. B.1 for three distinct initial pump power values $P_P(z = L)$, $P_{R,1} = 703$ mW (yellow crosses), $P_{R,2} = 801$ mW (orange crosses) and $P_{R,1=3} = 898$ mW (blue crosses). For each case, the

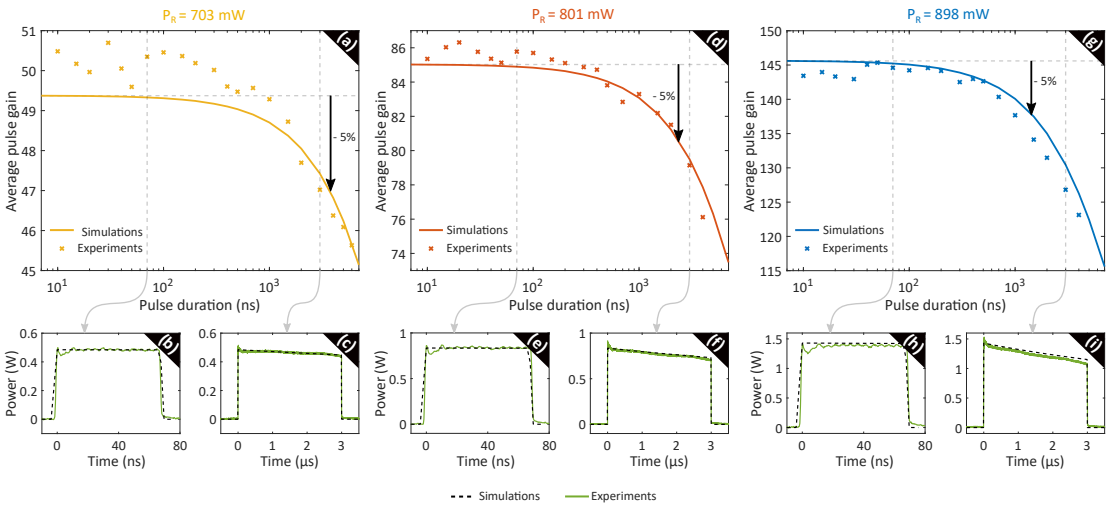

Figure B.1: On-off energy gain as function of the pulse duration for initial Raman pump powers of (a) $P_{R,1} = 703$ mW, (b) $P_{R,2} = 801$ mW and (c) $P_{R,3} = 898$ mW. Power time profiles of the amplified pulses for (b), (e), (h) $T_S = 50$ ns and (c), (f), (i) $T_S = 3$ μs.

gain remains almost constant for short pulses (< 100 ns), very close to values from the unsaturated CW theory. Indeed, the gain is around 50, 86 and 145 for the respective pump power values, to be compared with the theoretical values of 49.4, 85 and 145.7 from the theory ($G = exp(g_R P_R L_{eff})$ with $L_{eff} = \frac{1-exp(-\alpha_P L)}{\alpha_P}$ [73]). This comes from the negligible saturation of the Raman pump wave as the time overlap between the Stokes signal pulse and the pump is very small for very short pulses. It is verified by the power time profiles of the amplified pulses in Fig. B.1. (b), (e) and (h) for $T_S = 70$ ns (solid green lines). In each case, the pulses keep their square shape after amplification which means that the trailing edge have been amplified by the same unsaturated pump as the leading edge. This unsaturated regime allows then to overpass the CW regime amplification limit and to reach pulses with very high peak powers. For $P_{R,3} = 898$ mW, the pulses are amplified up to 1.4 W, beyond the pump value. For longer pulses, the gain drops as the pump saturation is not negligible anymore. Indeed, the time overlap between the Stokes signal pulse and the pump increases with the pulses width and enhances the local pump depletion. From the power time profiles of the $T_S = 3$ μs amplified pulses in Fig. B.1. (c), (f) and (i), we notice their distortion. Indeed, the trailing edges, amplified by a saturated pump, are less powerful than the leading edges, amplified by an unsaturated pump. This gain drop also depends on the initial Raman pump power and appears for shorter pulses when we increase its value. Indeed, we reach a 5% drop from the plateau value at 3850 ns, 2230 ns and 1320 ns for the respective pump power values. Numerical

simulations of Eqs. (B.1) and (B.2) are performed and compared with the experimental results (solid lines for the gain and black dashed lines for the pulse profiles). The overall agreement is excellent as very close on-off gain values are obtained as well as a very good accordance for the amplified pulse shapes. In the same way, the forward Raman pumping configuration is also investigated. The energy gain curve is displayed in Fig. B.2, for pulse durations ranging from 10 ns to 4 μs (purple crosses). The gain is

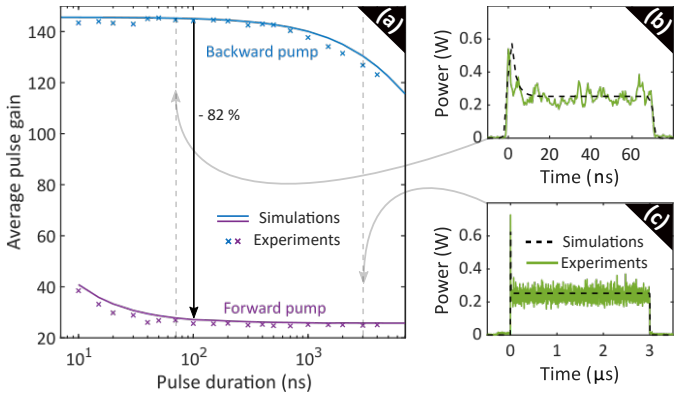

Figure B.2: (a) On-off energy gain as function of the pulse duration for backward (blue) and forward (purple) Raman pumping schemes. Power time profiles of the co-amplified pulses for (b) $T_S = 70$ ns and (c) $T_S = 3$ μs.

constant for $T_S \geq 50$ ns as the pump reaches the maximum saturation state. The walk-off is not significant over the pulse width and we can approximate the amplification process with the saturated CW theory. However for shorter pulses, the gain increases as the walk-off leads the pulse to be significantly shifted away of the depleted pump during the propagation. Looking at the amplified pulses power profiles in Fig. B.2. (b) and (c) for $T_S = 70$ ns and $T_S = 3$ μs respectively, we notice a few nanoseconds amplification peak at the leading edge which is characteristics from this walk-off. For comparison, the gain curve from the backward configuration is also plotted (blue crosses) and reveals that the forward one leads to much weaker gain values, by around 82% at $T_S = 100$ ns.

Appendix C

Raman pulse shaping, towards a perfect loss compensation

In all the experimental studies that has been performed in this thesis and described in this manuscript, we compensated for the linear losses suffered by the signal during its propagation in the fiber with a constant power backward pumping Raman amplifier scheme. Indeed, as it is illustrated in Fig. C.1. (a), a signal propagating in a 25 km long fiber with α(@1550 nm) = 0.2 dB/km suffers a power attenuation of 68% between the fiber input and output. By adding a 1450 nm backward Raman pump, with a constant power profile as seen in Fig. C.1. (b) (g_R = and α(@1450 nm) = 0.28 dB/km), the linear losses are largely compensated, as depicted by the power evolution of the amplified signal in Fig. C.1. (c). In that case, the power fluctuation doesn't exceed 20% (reached in the fiber center) of the initial value. This loss compensation turns out to be even more satisfying with shorter optical fibers and was sufficient for the experimental works of this thesis. However, with longer spans, it becomes very limited and less efficient, as demonstrated by the numerical plots in Fig. C.1. (d-f) with 100 km long fiber. The power evolution of the amplified signal reveals a drop of more than 90% of the initial power in the fiber center. The use of a bidirectional pumping scheme, both a backward pump and a forward pump [73], allows to reduce the amplitude of the power fluctuations but it faces the same limitations. To solve this issue, it would be necessary to modulate the gain experienced locally by the signal during its propagation. To do so, it requires to shape the backward Raman pump power, so the signal is amplified at each fiber location with a specific pump power. Such a scheme is implemented experimentally by using the additional pulse shaping (14) described in Chapter 3. An AO modulator shapes the Raman pump into a train of pulses which are twice wider than the fiber propagation time (so the signal always faces the Raman pump pulse as they counter-propagate). The pump pulses shape is controlled by the AWG which electrically triggers the AO modulator. It is necessary to precisely synchronize the signal and Raman pump pulses trains so the signal experiences the desired gain evolution. To verify the efficiency of

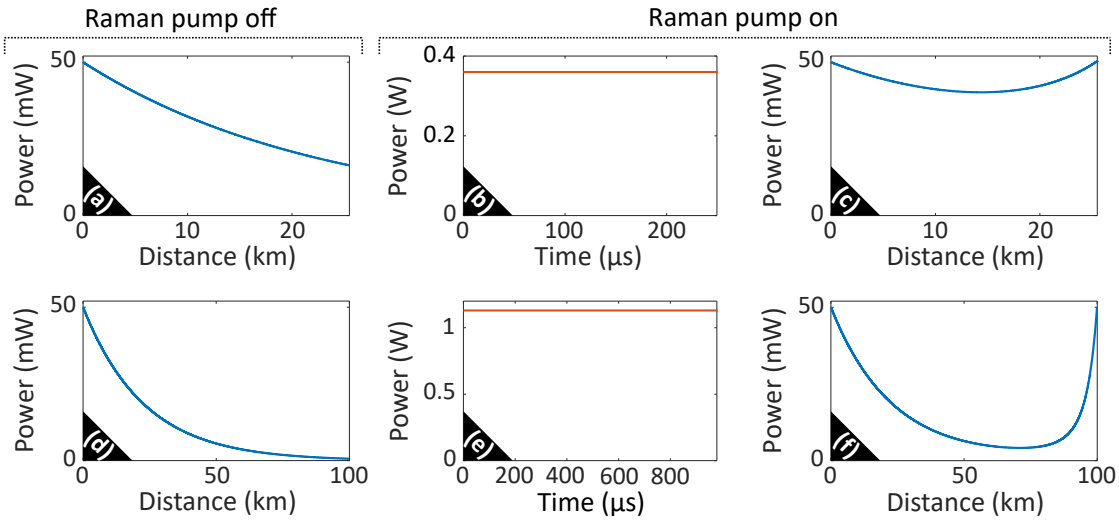

Figure C.1: (a)-(d) Numerical simulations of the power evolution of a signal with the Raman pump switched off. (b)-(e) Power profile of the constant Raman pump. (c)-(f) Numerical simulations of the power evolution of a signal with the corresponding constant Raman pump. (a-c) For a 25 km long fiber and (d-f) for a 100 km long fiber. Parameters: α(@1550 nm) = 0.2 dB/km, α(@1450 nm) = 0.28 dB/km and g_R = 0.24 $W^{-1}km^{-1}$.

the scheme, we record both the OTDR traces from the amplified signal and the Raman pump pulses profiles. However, the Rayleigh backscattered signal is also amplified by the Raman pump on its way back to the fiber input. The ODTR trace doesn't allow then to recover directly the evolution of the amplified signal along the fiber and it requires a post processing correction of the traces. The problem is illustrated with numerical simulations from a two steps Raman pump pulse displayed in Fig. C.2. (a). The relative

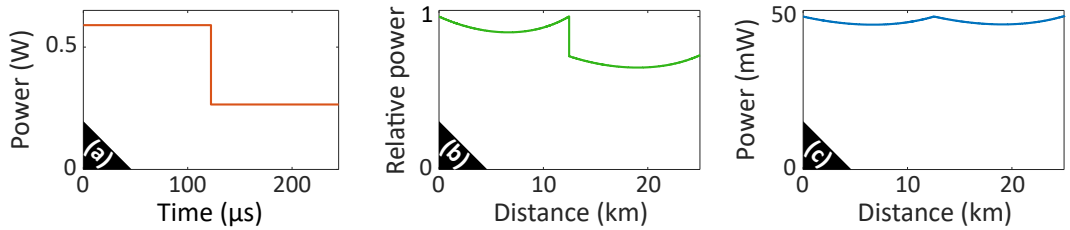

Figure C.2: Numerical data of (a) the Raman pump power profile, (b) the relative evolution of the backscattered Rayleigh signal power and (c) the evolution of the amplified signal power from the correction of (b).

power evolution of the Rayleigh backscattered signal is plotted in Fig. C.2. (b) and reveals a discontinuity at the center. Indeed, it is directly related to the discontinuity of the Raman steps pulse. In the fiber first half, the backscattered signal co-propagates with a much powerful Raman pump (and so a higher gain) than in the second half. The

correction of the OTDR traces is especially necessary because the Raman pump power is not constant anymore. After the post processing, we recover the power evolution of the amplified signal plotted in Fig. C.2. (c), which exhibits a continuous evolution now. Let's present a couple of experimental examples with different Raman pulse profiles. The first one is a Raman pulse made of two equal steps whose recorded profile is plotted in Fig. C.3. (a) (first step at 620 mW and second step at 190 mW). It amplifies a signal along

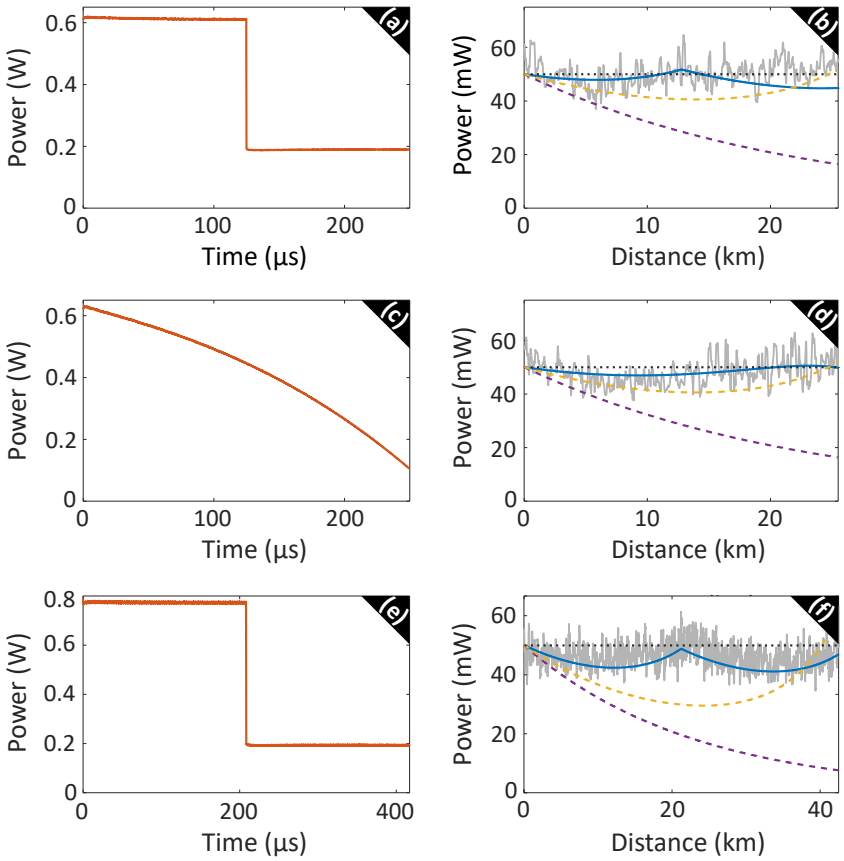

Figure C.3: (a)-(c)-(e) Experimental Raman pump pulse power profiles. (b)-(d)-(f) Corresponding power evolution of the amplified signal from experiments (grey solid line) and numerics (blue solid line). The dashed purple lines, the dashed yellow lines and the black dotted lines account for the Raman pump off, a constant Raman pump power and the propagation in a transparent fiber respectively.

a 25.5 km long fiber whose OTDR trace is recorded and plotted in Fig. C.3. (b) (grey solid line). For a comparison purpose, we also displayed the corresponding numerical evolution (blue solid line) which reveals a good agreement. The loss compensation is way better than with a constant power Raman pump (dashed yellow line). The second Raman pump pulse, which has an offsetted square root evolution, is recorded and plotted in Fig. C.3. (c) (the power decreases from 630 mW to 106 mW). The Rayleigh

backscattering of the amplified signal along the same 25.5 km long fiber is recorded and displayed in Fig. C.3. (d) (grey solid line). As in the previous case, we superposed the corresponding numerical simulation (blue solid line) in very good accordance with experiments. From this specific Raman pulse shape, we highlight a very good loss compensation with power fluctuations that doesn't exceed 6% of the initial value and which is much better than the one from a constant Raman pump power (dashed yellow line). The last example has a similar Raman pules shape to the first one and is plotted in Fig. C.3. (e) (first step at 620 mW and second step at 190 mW). It amplifies a signal along a 42.5 long fiber whose OTDR trace is recorded and plotted in Fig. C.3. (f) (grey solid line). The maximum fluctuations from the initial value are reduced from 41% (dashed yellow line) to 18% with this Raman profile. To go further and increase the efficiency of the loss compensation, we can find the optimal pulse profile, which allows to get a perfectly transparent fiber, by numerically solving the inverse problem and applying it experimentally.

Bibliography

[1] T. H. Maiman, "Optical and microwave-optical experiments in ruby", Physical Review Letters **4**, 564–566 (1960).

[2] C. V. Raman and K. S. Krishnan, "A new type of secondary radiation", Nature **121**, 501–502 (1928).

[3] P. A. Franken, A. E. Hill, C. W. Peters, and G. Weinreich, "Generation of optical harmonics", Physical Review Letters **7**, 118–119 (1961).

[4] W. Kaiser and C. G. B. Garrett, "Two-photon excitation in CaF_2:Eu^{2+}", Physical Review Letters **7**, 229–231 (1961).

[5] P. D. Maker, R. W. Terhune, and C. M. Savage, "Intensity-dependent changes in the refractive index of liquids", Physical Review Letters **12**, 507–509 (1964).

[6] R. Y. Chiao, C. H. Townes, and B. P. Stoicheff, "Stimulated Brillouin scattering and coherent generation of intense hypersonic waves", Physical Review Letters **12**, 592–595 (1964).

[7] R. L. Carman, R. Y. Chiao, and P. L. Kelley, "Observation of degenerate stimulated four-photon interaction and four-wave parametric amplification", Physical Review Letters **17**, 1281–1283 (1966).

[8] F. P. Kapron, D. B. Keck, and R. D. Maurer, "Radiation losses in glass optical waveguides", Applied Physics Letters **17**, 423–425 (1970).

[9] K. C. Kao and G. A. Hockham, "Dielectric-fibre surface waveguides for optical frequencies", Proceedings of the Institution of Electrical Engineers **113**, 1151–1158 (1966).

[10] E. Ippen and R. Stolen, "Stimulated Brillouin scattering in optical fibers", Applied Physics Letters **21**, 539–541 (1972).

[11] R. H. Stolen, E. P. Ippen, and A. R. Tynes, "Raman oscillation in glass optical waveguide", Applied Physics Letters **20**, 62–64 (1972).

[12] R. H. Stolen and A. Ashkin, "Optical Kerr effect in glass waveguide", Applied Physics Letters **22**, 294–296 (1973).

[13] R. Stolen, "Phase-matched-stimulated four-photon mixing in silica-fiber waveguides", IEEE Journal of Quantum Electronics **11**, 100–103 (1975).

[14] R. H. Stolen and C. Lin, "Self-phase-modulation in silica optical fibers", Physical Review A **17**, 1448–1453 (1978).

[15] K. Tai, A. Hasegawa, and A. Tomita, "Observation of modulational instability in optical fibers", Physical Review Letters **56**, 135–138 (1986).

[16] V. I. Bespalov and V. I. Talanov, "Filamentary structure of light beams in nonlinear liquids", Soviet Journal of Experimental and Theoretical Physics Letters **3**, 307 (1966).

[17] T. B. Benjamin and J. E. Feir, "The disintegration of wave trains on deep water part 1. Theory", Journal of Fluid Mechanics **27**, 417–430 (1967).

[18] V. Zakharov and L. Ostrovsky, "Modulation instability: the beginning", Physica D: Nonlinear Phenomena **238**, 540–548 (2009).

[19] K. E. Strecker, G. B. Partridge, A. G. Truscott, and R. G. Hulet, "Formation and propagation of matter-wave soliton trains", Nature **417**, 150–153 (2002).

[20] T. Taniuti and H. Washimi, "Self-trapping and instability of hydromagnetic waves along the magnetic field in a cold plasma", Physical Review Letters **21**, 209–212 (1968).

[21] N. Akhmediev, J. Soto-Crespo, and A. Ankiewicz, "Extreme waves that appear from nowhere: on the nature of rogue waves", Physics Letters A **373**, 2137–2145 (2009).

[22] M. Onorato, S. Residori, U. Bortolozzo, A. Montina, and F. Arecchi, "Rogue waves and their generating mechanisms in different physical contexts", Physics Reports **528**, 47–89 (2013).

[23] J. M. Dudley, F. Dias, M. Erkintalo, and G. Genty, "Instabilities, breathers and rogue waves in optics", Nature Photonics **8**, 755–764 (2014).

[24] N. Akhmediev, B. Kibler, F. Baronio, M. Belić, W.-P. Zhong, Y. Zhang, W. Chang, J. M. Soto-Crespo, P. Vouzas, P. Grelu, C. Lecaplain, K. Hammani, S. Rica, A. Picozzi, M. Tlidi, K. Panajotov, A. Mussot, A. Bendahmane, P. Szriftgiser, G. Genty, J. Dudley, A. Kudlinski, A. Demircan, U. Morgner, S. Amiraranashvili, C. Bree, G. Steinmeyer, C. Masoller, N. G. R. Broderick, A. F. J. Runge, M. Erkintalo, S. Residori, U. Bortolozzo, F. T. Arecchi, S. Wabnitz, C. G. Tiofack, S. Coulibaly, and M. Taki, "Roadmap on optical rogue waves and extreme events", Journal of Optics **18**, 063001 (2016).

[25] S. Chen, F. Baronio, J. M. Soto-Crespo, P. Grelu, and D. Mihalache, "Versatile rogue waves in scalar, vector, and multidimensional nonlinear systems", Journal of Physics A: Mathematical and Theoretical **50**, 463001 (2017).

[26] J. M. Dudley, G. Genty, A. Mussot, A. Chabchoub, and F. Dias, "Rogue waves and analogies in optics and oceanography", Nature Reviews Physics **1**, 675–689 (2019).

[27] J. M. Dudley, G. Genty, F. Dias, B. Kibler, and N. Akhmediev, "Modulation instability, Akhmediev breathers and continuous wave supercontinuum generation", Optics Express **17**, 21497 (2009).

[28] N. Akhmediev, A. Ankiewicz, J. Soto-Crespo, and J. M. Dudley, "Universal triangular spectra in parametrically-driven systems", Physics Letters A **375**, 775–779 (2011).

[29] E. Fermi, P. Pasta, S. Ulam, and M. Tsingou, *Studies of the nonlinear problems*, LA-1940 (1955).

[30] N. N. Akhmediev, "Déjà vu in optics", Nature **413**, 267–268 (2001).

[31] N. J. Zabusky and M. D. Kruskal, "Interaction of "solitons" in a collisionless plasma and the recurrence of initial states", Physical Review Letters **15**, 240–243 (1965).

[32] B. M. Lake, H. C. Yuen, H. Rungaldier, and W. E. Ferguson, "Nonlinear deep-water waves: theory and experiment. Part 2. Evolution of a continuous wave train", Journal of Fluid Mechanics **83**, 49–74 (1977).

[33] D. Jäger, "Soliton propagation along periodic-loaded transmission line", Applied Physics **16**, 35–38 (1978).

[34] G. Van Simaeys, P. Emplit, and M. Haelterman, "Experimental demonstration of the Fermi-Pasta-Ulam recurrence in a modulationally unstable optical wave", Physical Review Letters **87**, 033902 (2001).

[35] N. N. Akhmediev and V. I. Korneev, "Modulation instability and periodic solutions of the nonlinear Schrödinger equation", Theoretical and Mathematical Physics **69**, 1089–1093 (1986).

[36] B. Kibler, J. Fatome, C. Finot, G. Millot, F. Dias, G. Genty, N. Akhmediev, and J. M. Dudley, "The Peregrine soliton in nonlinear fibre optics", Nature Physics **6**, 790–795 (2010).

[37] K. Hammani, B. Wetzel, B. Kibler, J. Fatome, C. Finot, G. Millot, N. Akhmediev, and J. M. Dudley, "Spectral dynamics of modulation instability described using Akhmediev breather theory", Optics Letters **36**, 2140 (2011).

[38] B. Kibler, J. Fatome, C. Finot, G. Millot, G. Genty, B. Wetzel, N. Akhmediev, F. Dias, and J. M. Dudley, "Observation of Kuznetsov-Ma soliton dynamics in optical fibre", Scientific Reports **2**, 463 (2012).

[39] O. Kimmoun, H. C. Hsu, H. Branger, M. S. Li, Y. Y. Chen, C. Kharif, M. Onorato, E. J. R. Kelleher, B. Kibler, N. Akhmediev, and A. Chabchoub, "Modulation instability and phase-shifted Fermi-Pasta-Ulam recurrence", Scientific Reports **6**, 28516 (2016).

[40] A. Mussot, A. Kudlinski, M. Droques, P. Szriftgiser, and N. Akhmediev, "Fermi-Pasta-Ulam recurrence in nonlinear fiber optics: the role of reversible and irreversible losses", Physical Review X **4**, 011054 (2014).

[41] X. Hu, W. Chen, Y. Lu, Z. Yu, M. Chen, and Z. Meng, "Distributed measurement of Fermi–Pasta–Ulam recurrence in optical fibers", IEEE Photonics Technology Letters **30**, 47–50 (2018).

[42] A. Mussot, C. Naveau, M. Conforti, A. Kudlinski, F. Copie, P. Szriftgiser, and S. Trillo, "Fibre multi-wave mixing combs reveal the broken symmetry of Fermi–Pasta–Ulam recurrence", Nature Photonics **12**, 303–308 (2018).

[43] C. Naveau, "Modulation instability and Fermi-Pasta-Ulam-Tsingou recurrences in optical fibres", These de doctorat (Université de Lille (2018-2021), 2019).

[44] C. Naveau, P. Szriftgiser, A. Kudlinski, M. Conforti, S. Trillo, and A. Mussot, "Experimental characterization of recurrences and separatrix crossing in modulational instability", Optics Letters **44**, 5426 (2019).

[45] C. Naveau, P. Szriftgiser, A. Kudlinski, M. Conforti, S. Trillo, and A. Mussot, "Full-field characterization of breather dynamics over the whole length of an optical fiber", Optics Letters **44**, 763 (2019).

[46] G. Vanderhaegen, P. Szriftgiser, C. Naveau, A. Kudlinski, M. Conforti, S. Trillo, N. Akhmediev, and A. Mussot, "Observation of doubly periodic solutions of the nonlinear Schrödinger equation in optical fibers", Optics Letters **45**, 3757 (2020).

[47] G. Vanderhaegen, C. Naveau, P. Szriftgiser, A. Kudlinski, M. Conforti, A. Mussot, M. Onorato, S. Trillo, A. Chabchoub, and N. Akhmediev, ""Extraordinary" modulation instability in optics and hydrodynamics", Proceedings of the National Academy of Sciences **118** (2021).

[48] G. Vanderhaegen, P. Szriftgiser, A. Kudlinski, M. Conforti, S. Trillo, M. Droques, and A. Mussot, "Observation of four Fermi-Pasta-Ulam-Tsingou recurrences in an ultra-low-loss optical fiber", Optics Express **28**, 17773 (2020).

[49] G. Vanderhaegen, P. Szriftgiser, A. Kudlinski, M. Conforti, A. Armaroli, and A. Mussot, "Observation of the noise-driven thermalization of the Fermi-Pasta-Ulam-Tsingou recurrence in optical fibers", arXiv:2205.01349 [nlin, physics: physics] (2022).

[50] G. Vanderhaegen, P. Szriftgiser, A. Kudlinski, A. Armaroli, M. Conforti, A. Mussot, and S. Trillo, "Multiple symmetry breaking induced by weak damping in the Fermi-Pasta-Ulam-Tsingou recurrence process", arXiv:2206.00912 [nlin, physics:physics] (2022).

[51] N. N. Akhmediev, V. M. Eleonskii, and N. E. Kulagin, "Exact first-order solutions of the nonlinear Schrödinger equation", Theoretical and Mathematical Physics **72**, 809–818 (1987).

[52] M. Conforti, A. Mussot, A. Kudlinski, S. Trillo, and N. Akhmediev, "Doubly periodic solutions of the focusing nonlinear Schrödinger equation: recurrence, period doubling, and amplification outside the conventional modulation-instability band", Physical Review A **101**, 023843 (2020).

[53] G. Vanderhaegen, P. Szriftgiser, M. Conforti, A. Kudlinski, M. Droques, and A. Mussot, "Experimental investigation of short pulse Raman amplification with backward pumping", Optics Letters **46**, 5019 (2021).

[54] B. Lee, "Review of the present status of optical fiber sensors", Optical Fiber Technology, 23 (2003).

[55] E. F. Schubert, *Light-emitting diodes (second edition, 2006)* (E. Fred Schubert, 2006).

[56] G. A. Thomas, B. I. Shraiman, P. F. Glodis, and M. J. Stephen, "Towards the clarity limit in optical fibre", Nature **404**, 262–264 (2000).

[57] Y. Tamura, H. Sakuma, K. Morita, M. Suzuki, Y. Yamamoto, K. Shimada, Y. Honma, K. Sohma, T. Fujii, and T. Hasegawa, "The first 0.14-db/km loss optical fiber and its impact on submarine transmission", Journal of Lightwave Technology **36**, 44–49 (2018).

[58] G. Agrawal, *Nonlinear fiber optics* (Academic Press, 2012).

[59] L. Cohen, "Comparison of single-mode fiber dispersion measurement techniques", Journal of Lightwave Technology **3**, 958–966 (1985).

[60] L. Mollenauer, P. Mamyshev, and M. Neubelt, "Method for facile and accurate measurement of optical fiber dispersion maps", in Proceedings of optical fiber communication conference (1997), pp. 255–256.

[61] P. Russell, "Photonic crystal fibers", Science **299**, 358–362 (2003).

[62] J. C. Knight, "Photonic crystal fibres", Nature **424**, 847–851 (2003).

[63] L. Cohen, C. Lin, and W. French, "Tailoring zero chromatic dispersion into the 1.5–1.6 μm low-loss spectral region of single-mode fibres", Electronics Letters **15**, 334 (1979).

[64] V. A. Bhagavatula, M. S. Spotz, and W. F. Love, "Dispersion-shifted segmented-core single-mode fibers", Optics Letters **9**, 186 (1984).

[65] M. Asobe, "Nonlinear optical properties of chalcogenide glass fibers and their application to all-optical switching", Optical Fiber Technology **3**, 142–148 (1997).

[66] L. Shen, H. Ren, M. Huang, D. Wu, and A. C. Peacock, "A review of nonlinear applications in silicon optical fibers from telecom wavelengths into the mid-infrared spectral region", Optics Communications **463**, 125437 (2020).

[67] R. R. Alfano and S. L. Shapiro, "Observation of self-phase modulation and small-scale filaments in crystals and glasses", Physical Review Letters **24**, 592–594 (1970).

[68] Y. R. Shen and M. M. T. Loy, "Theoretical interpretation of small-scale filaments of light originating from moving focal spots", Physical Review A **3**, 2099–2105 (1971).

[69] R. W. Boyd, *Nonlinear optics* (Academic Press, 2020).

[70] R. H. Stolen and E. P. Ippen, "Raman gain in glass optical waveguides", Applied Physics Letters **22**, 276–278 (1973).

[71] R. H. Stolen, W. J. Tomlinson, H. A. Haus, and J. P. Gordon, "Raman response function of silica-core fibers", Journal of the Optical Society of America B **6**, 1159 (1989).

[72] J. Bromage, K. Rottwitt, and M. E. Lines, "A method to predict the Raman gain spectra of germanosilicate fibers with arbitrary index profiles", IEEE Photonics Technology Letters **14**, 24–26 (2002).

[73] C. Headley and G. Agrawal, *Raman amplification in fiber optical communication systems* (Academic Press, 2005).

[74] K. Blow and D. Wood, "Theoretical description of transient stimulated Raman scattering in optical fibers", IEEE Journal of Quantum Electronics **25**, 2665–2673 (1989).

[75] P. V. Mamyshev and S. V. Chernikov, "Ultrashort-pulse propagation in optical fibers", Optics Letters **15**, 1076–1078 (1990).

[76] P. L. François, "Nonlinear propagation of ultrashort pulses in optical fibers: total field formulation in the frequency domain", JOSA B **8**, 276–293 (1991).

[77] N. Lewis, *Computing on the mesa*, https://www.lanl.gov/discover/publications/national-security-science/2020-winter/computing-history.shtml.

[78] Apple, *Apple introduces iPhone 13 and iPhone 13 mini*, https://www.apple.com/newsroom/2021/09/apple-introduces-iphone-13-and-iphone-13-mini/.

[79] M. A. Porter, N. J. Zabusky, B. Hu, and D. K. Campbell, "Fermi, Pasta, Ulam and the birth of experimental mathematics: a numerical experiment that Enrico Fermi, John Pasta, and Stanislaw Ulam reported 54 years ago continues to inspire discovery", American Scientist **97**, 214–221 (2009).

[80] J. L. Tuck and M. T. Menzel, "The superperiod of the nonlinear weighted string (FPU) problem", Advances in Mathematics **9**, 399–407 (1972).

[81] S. D. Pace and D. K. Campbell, "Behavior and breakdown of higher-order Fermi-Pasta-Ulam-Tsingou recurrences", Chaos: An Interdisciplinary Journal of Nonlinear Science **29**, 023132 (2019).

[82] G. Benettin, H. Christodoulidi, and A. Ponno, "The Fermi-Pasta-Ulam problem and its underlying integrable dynamics", Journal of Statistical Physics **152**, 195–212 (2013).

[83] M. Onorato, L. Vozella, D. Proment, and Y. V. Lvov, "Route to thermalization in the α-Fermi–Pasta–Ulam system", Proceedings of the National Academy of Sciences **112**, 4208–4213 (2015).

[84] Y. V. Lvov and M. Onorato, "Double scaling in the relaxation time in the β-Fermi-Pasta-Ulam-Tsingou model", Physical Review Letters **120**, 144301 (2018).

[85] T. Dauxois and M. Peyrard, *Physics of solitons* (Cambridge University Press, Cambridge, UK ; New York, 2006).

[86] T. Dauxois, "Fermi, Pasta, Ulam, and a mysterious lady", Physics Today **61**, 55–57 (2008).

[87] T. Dauxois, "La (dis-)simulation FPU : une femme physicienne underground. Mary Tsingou et l'histoire de la première expérience numérique", Reflets de la physique, 26–30 (2020).

[88] L. F. Mollenauer, R. H. Stolen, and J. P. Gordon, "Experimental observation of picosecond pulse narrowing and solitons in optical fibers", Physical Review Letters **45**, 1095–1098 (1980).

[89] V. E. Zakharov and A. B. Shabat, "Exact theory of two-dimensional self-focusing and one-dimensional self-modulation of waves in nonlinear media", Soviet Journal of Experimental and Theoretical Physics **34**, 62 (1972).

[90] A. Hasegawa and F. Tappert, "Transmission of stationary nonlinear optical pulses in dispersive dielectric fibers. I. Anomalous dispersion", Applied Physics Letters **23**, 142–144 (1973).

[91] S. Pitois and G. Millot, "Experimental observation of a new modulational instability spectral window induced by fourth-order dispersion in a normally dispersive single-mode optical fiber", Optics Communications **226**, 415–422 (2003).

[92] J. D. Harvey, R. Leonhardt, S. Coen, G. K. L. Wong, J. Knight, W. J. Wadsworth, and P. S. J. Russell, "Scalar modulation instability in the normal dispersion regime by use of a photonic crystal fiber", Optics Letters **28**, 2225–2227 (2003).

[93] S. Coen and M. Haelterman, "Modulational instability induced by cavity boundary conditions in a normally dispersive optical fiber", Physical Review Letters **79**, 4139–4142 (1997).

[94] S. G. Murdoch, R. Leonhardt, and J. D. Harvey, "Polarization modulation instability in weakly birefringent fibers", Optics Letters **20**, 866 (1995).

[95] G. Millot, E. Seve, S. Wabnitz, and S. Trillo, "Observation of a novel large-signal four-photon instability in optical wave mixing", Physical Review Letters **80**, 504–507 (1998).

[96] M. Droques, A. Kudlinski, G. Bouwmans, G. Martinelli, and A. Mussot, "Experimental demonstration of modulation instability in an optical fiber with a periodic dispersion landscape", Optics Letters **37**, 4832 (2012).

[97] A. Mussot, M. Conforti, S. Trillo, F. Copie, and A. Kudlinski, "Modulation instability in dispersion oscillating fibers", Advances in Optics and Photonics **10**, 1 (2018).

[98] A. E. Kraych, D. Agafontsev, S. Randoux, and P. Suret, "Statistical properties of the nonlinear stage of modulation instability in fiber optics", Physical Review Letters **123**, 093902 (2019).

[99] A. M. Perego, F. Bessin, and A. Mussot, "Complexity of modulation instability", Physical Review Research **4**, L022057 (2022).

[100] S. Toenger, T. Godin, C. Billet, F. Dias, M. Erkintalo, G. Genty, and J. M. Dudley, "Emergent rogue wave structures and statistics in spontaneous modulation instability", Scientific Reports **5**, 10380 (2015).

[101] P. Suret, R. E. Koussaifi, A. Tikan, C. Evain, S. Randoux, C. Szwaj, and S. Bielawski, "Single-shot observation of optical rogue waves in integrable turbulence using time microscopy", Nature Communications **7**, 13136 (2016).

[102] M. Närhi, B. Wetzel, C. Billet, S. Toenger, T. Sylvestre, J.-M. Merolla, R. Morandotti, F. Dias, G. Genty, and J. M. Dudley, "Real-time measurements of spontaneous breathers and rogue wave events in optical fibre modulation instability", Nature Communications **7**, 13675 (2016).

[103] A. Gelash, D. Agafontsev, V. Zakharov, G. El, S. Randoux, and P. Suret, "Bound state soliton gas dynamics underlying the spontaneous modulational instability", Physical Review Letters **123**, 234102 (2019).

[104] C. Cambournac, H. Maillotte, E. Lantz, J. M. Dudley, and M. Chauvet, "Spatiotemporal behavior of periodic arrays of spatial solitons in a planar waveguide with relaxing Kerr nonlinearity", Journal of the Optical Society of America B **19**, 574 (2002).

[105] M. Wu and C. E. Patton, "Experimental observation of Fermi-Pasta-Ulam recurrence in a nonlinear feedback ring system", Physical Review Letters **98**, 047202 (2007).

[106] D. Pierangeli, M. Flammini, L. Zhang, G. Marcucci, A. J. Agranat, P. G. Grinevich, P. M. Santini, C. Conti, and E. DelRe, "Observation of Fermi-Pasta-Ulam-Tsingou recurrence and its exact dynamics", Physical Review X **8**, 041017 (2018).

[107] G. Van Simaeys, P. Emplit, and M. Haelterman, "Experimental study of the reversible behavior of modulational instability in optical fibers", Journal of the Optical Society of America B **19**, 477 (2002).

[108] A. Bendahmane, A. Mussot, A. Kudlinski, P. Szriftgiser, M. Conforti, S. Wabnitz, and S. Trillo, "Optimal frequency conversion in the nonlinear stage of modulation instability", Optics Express **23**, 30861 (2015).

[109] J.-W. Goossens, H. Hafermann, and Y. Jaouën, "Experimental realization of Fermi-Pasta-Ulam-Tsingou recurrence in a long-haul optical fiber transmission system", Scientific Reports **9**, 18467 (2019).

[110] Y.-C. Ma, "The perturbed plane-wave solutions of the cubic Schrödinger equation", Studies in Applied Mathematics **60**, 43–58 (1979).

[111] E. A. Kuznetsov, A. M. Rubenchik, and V. E. Zakharov, "Soliton stability in plasmas and hydrodynamics", Physics Reports **142**, 103–165 (1986).

[112] D. H. Peregrine, "Water waves, nonlinear Schrödinger equations and their solutions", The Journal of the Australian Mathematical Society. Series B. Applied Mathematics **25**, 16–43 (1983).

[113] N. Devine, A. Ankiewicz, G. Genty, J. Dudley, and N. Akhmediev, "Recurrence phase shift in Fermi–Pasta–Ulam nonlinear dynamics", Physics Letters A **375**, 4158–4161 (2011).

[114] M. Erkintalo, G. Genty, B. Wetzel, and J. Dudley, "Akhmediev breather evolution in optical fiber for realistic initial conditions", Physics Letters A **375**, 2029–2034 (2011).

[115] P. Grinevich and P. Santini, "The exact rogue wave recurrence in the NLS periodic setting via matched asymptotic expansions, for 1 and 2 unstable modes", Physics Letters A **382**, 973–979 (2018).

[116] S. Trillo and S. Wabnitz, "Dynamics of the nonlinear modulational instability in optical fibers", Optics Letters **16**, 986 (1991).

[117] G. Cappellini and S. Trillo, "Third-order three-wave mixing in single-mode fibers: exact solutions and spatial instability effects", Journal of the Optical Society of America B **8**, 824 (1991).

[118] A. Sheveleva, U. Andral, B. Kibler, P. Colman, J. M. Dudley, and C. Finot, "Idealized four-wave mixing dynamics in a nonlinear Schrödinger equation fiber system", Optica **9**, 656 (2022).

[119] H. T. Moon, "Homoclinic crossings and pattern selection", Physical Review Letters **64**, 412–414 (1990).

[120] D. Eeltink, A. Armaroli, C. Luneau, H. Branger, M. Brunetti, and J. Kasparian, "Separatrix crossing and symmetry breaking in NLSE-like systems due to forcing and damping", Nonlinear Dynamics **102**, 2385–2398 (2020).

[121] B. Frisquet, B. Kibler, and G. Millot, "Collision of Akhmediev breathers in nonlinear fiber optics", Physical Review X **3**, 041032 (2013).

[122] B. Frisquet, A. Chabchoub, J. Fatome, C. Finot, B. Kibler, and G. Millot, "Two-stage linear-nonlinear shaping of an optical frequency comb as rogue nonlinear-Schrödinger-equation-solution generator", Physical Review A **89**, 023821 (2014).

[123] P. Healey, "Fading in heterodyne otdr", Electronics Letters **20**, 30–32 (1984).

[124] G. Xu, K. Hammani, A. Chabchoub, J. M. Dudley, B. Kibler, and C. Finot, "Phase evolution of Peregrine-like breathers in optics and hydrodynamics", Physical Review E **99**, 012207 (2019).

[125] U. Andral, B. Kibler, J. M. Dudley, and C. Finot, "Akhmediev breather signatures from dispersive propagation of a periodically phase-modulated continuous wave", Wave Motion **95**, 102545 (2020).

[126] A. E. Kraych, P. Suret, G. El, and S. Randoux, "Nonlinear evolution of the locally induced modulational instability in fiber optics", Physical Review Letters **122**, 054101 (2019).

[127] L. Thévenaz, "Review and progress in distributed fiber sensing", in Optical fiber sensors (2006), paper thc1 (2006), ThC1.

[128] M. K. Barnoski and S. M. Jensen, "Fiber waveguides: a novel technique for investigating attenuation characteristics", Applied Optics **15**, 2112 (1976).

[129] M. Nakazawa, "Rayleigh backscattering theory for single-mode optical fibers", Journal of the Optical Society of America **73**, 1175 (1983).

[130] *Smf-28 ultra optical fiber*, PI-1424-AEN, Corning (2021).

[131] F. Friederich, G. Schuricht, A. Deninger, F. Lison, G. Spickermann, P. Haring Bolívar, and H. G. Roskos, "Phase-locking of the beat signal of two distributed-feedback diode lasers to oscillators working in the Mhz to Thz range", Optics Express **18**, 8621 (2010).

[132] C. Naveau, G. Vanderhaegen, P. Szriftgiser, G. Martinelli, M. Droques, A. Kudlinski, M. Conforti, S. Trillo, N. Akhmediev, and A. Mussot, "Heterodyne optical time domain reflectometer combined with active loss compensation: a practical tool for investigating Fermi Pasta Ulam recurrence process and breathers dynamics in optical fibers", Frontiers in Physics **9**, 25 (2021).

[133] H. Izumita, S.-i. Furukawa, Y. Koyamada, and I. Sankawa, "Fading noise reduction in coherent OTDR", IEEE Photonics Technology Letters **4**, 201–203 (1992).

[134] K. Shimizu, T. Horiguchi, and Y. Koyamada, "Characteristics and reduction of coherent fading noise in Rayleigh backscattering measurement for optical fibers and components", Journal of Lightwave Technology **10**, 982–987 (1992).

[135] Y. Wakisaka, D. Iida, H. Oshida, and N. Honda, "Fading suppression of ϕ-OTDR with the new signal processing methodology of complex vectors across time and frequency domains", Journal of Lightwave Technology **39**, 4279–4293 (2021).

[136] Z. Zhao, H. Wu, J. Hu, K. Zhu, Y. Dang, Y. Yan, M. Tang, and C. Lu, "Interference fading suppression in Φ-OTDR using space-division multiplexed probes", Optics Express **29**, 15452 (2021).

[137] P. Hansen and L. Eskildsen, "Remote amplification in repeaterless transmission systems", Optical Fiber Technology **3**, 221–237 (1997).

[138] C. Finot, G. Millot, C. Billet, and J. M. Dudley, "Experimental generation of parabolic pulses via Raman amplification in optical fiber", Optics Express **11**, 1547–1552 (2003).

[139] K. Hammani, C. Finot, J. M. Dudley, and G. Millot, "Optical rogue-wave-like extreme value fluctuations in fiber Raman amplifiers", Optics Express **16**, 16467–16474 (2008).

[140] G. Xu, M. Conforti, A. Kudlinski, A. Mussot, and S. Trillo, "Dispersive dam-break flow of a photon fluid", Physical Review Letters **118**, 254101 (2017).

[141] C. R. S. Fludger, V. Handerek, and R. J. Mears, "Pump to signal RIN transfer in Raman fiber amplifiers", Journal of Lightwave Technology **19**, 1140 (2001).

[142] B. Varlot, Y. Chembo, and C. Finot, "Akhmediev breathers as ultra-wideband pulses", Microwave and Optical Technology Letters **56**, 664–667 (2014).

[143] G. Yang, F. O. Wu, H. E. L. Aviles, and D. N. Christodoulides, "Optical amplification and transmission of attenuated multi-soliton based on spectral characteristics of Akhmediev breather", Optics Communications **473**, 125899 (2020).

[144] W. Chen, Z. Meng, H. J. Zhou, and H. Luo, "Spontaneous and induced modulation instability in the presence of broadband spectra caused by the amplified spontaneous emission", Laser Physics **22**, 1305–1309 (2012).

[145] D. J. Kedziora, A. Ankiewicz, and N. Akhmediev, "Circular rogue wave clusters", Physical Review E **84**, 056611 (2011).

[146] S. Wabnitz and N. Akhmediev, "Efficient modulation frequency doubling by induced modulation instability", Optics Communications **283**, 1152–1154 (2010).

[147] M. Erkintalo, K. Hammani, B. Kibler, C. Finot, N. Akhmediev, J. M. Dudley, and G. Genty, "Higher-order modulation instability in nonlinear fiber optics", Physical Review Letters **107**, 253901 (2011).

[148] K. Hammani, B. Kibler, C. Finot, P. Morin, J. Fatome, J. M. Dudley, and G. Millot, "Peregrine soliton generation and breakup in standard telecommunications fiber", Optics Letters **36**, 112 (2011).

[149] O. Kimmoun, H. C. Hsu, B. Kibler, and A. Chabchoub, "Nonconservative higher-order hydrodynamic modulation instability", Physical Review E **96**, 022219 (2017).

[150] F. Copie, P. Suret, and S. Randoux, "Spatiotemporal observation of higher-order modulation instability in a recirculating fiber loop", Optics Letters **47**, 3560–3563 (2022).

[151] S. Thornhill and D. ter Haar, "Langmuir turbulence and modulational instability", Physics Reports **43**, 43–99 (1978).

[152] B. Ghosh and S. Banerjee, "Modulation instability of ion-acoustic waves in plasma with nonthermal electrons", Journal of Astrophysics **2014**, 1–8 (2014).

[153] J. H. V. Nguyen, D. Luo, and R. G. Hulet, "Formation of matter-wave soliton trains by modulational instability", Science **356**, 422–426 (2017).

[154] P. J. Everitt, M. A. Sooriyabandara, M. Guasoni, P. B. Wigley, C. H. Wei, G. D. McDonald, K. S. Hardman, P. Manju, J. D. Close, C. C. N. Kuhn, S. S. Szigeti, Y. S. Kivshar, and N. P. Robins, "Observation of a modulational instability in Bose-Einstein condensates", Physical Review A **96**, 041601 (2017).

[155] X.-X. Li, R.-J. Cheng, A.-X. Zhang, and J.-K. Xue, "Modulational instability of Bose-Einstein condensates with helicoidal spin-orbit coupling", Physical Review E **100**, 032220 (2019).

[156] A. Armaroli and S. Trillo, "Collective modulation instability of multiple four-wave mixing", Optics Letters **36**, 1999 (2011).

[157] J. Fatome, C. Finot, A. Armaroli, and S. Trillo, "Observation of modulationally unstable multi-wave mixing", Optics Letters **38**, 181 (2013).

[158] M. Baillot, M. Gay, C. Peucheret, J. Michel, and T. Chartier, "Phase quadrature discrimination based on three-pump four-wave mixing in nonlinear optical fibers", Optics Express **24**, 26930 (2016).

[159] S. Wabnitz and B. Wetzel, "Instability and noise-induced thermalization of Fermi–Pasta–Ulam recurrence in the nonlinear Schrödinger equation", Physics Letters A **378**, 2750–2756 (2014).

[160] B. Kibler, "Rogue breather structures in nonlinear systems with an emphasis on optical fibers as testbeds", in *Shaping light in nonlinear optical fibers* (John Wiley Sons, Ltd, 2017), pp. 293–323.

[161] B. M. Herbst and M. J. Ablowitz, "Numerically induced chaos in the nonlinear Schrödinger equation", Physical Review Letters **62**, 2065–2068 (1989).

[162] D. R. Solli, C. Ropers, and B. Jalali, "Active control of rogue waves for stimulated supercontinuum generation", Physical Review Letters **101**, 233902 (2008).

[163] J. M. Dudley, G. Genty, and B. J. Eggleton, "Harnessing and control of optical rogue waves in supercontinuum generation", Optics Express **16**, 3644 (2008).

[164] C. E. Shannon, "A mathematical theory of communication", The Bell System Technical Journal **27**, 379–423 (1948).

[165] K. Inoue and T. Mukai, "Spectral hole in the amplified spontaneous emission spectrum of a fiber optical parametric amplifier", Optics Letters **26**, 869 (2001).

[166] A. Armaroli, D. Eeltink, M. Brunetti, and J. Kasparian, "Nonlinear stage of Benjamin-Feir instability in forced/damped deep-water waves", Physics of Fluids **30**, 017102 (2018).

[167] F. Coppini, P. G. Grinevich, and P. M. Santini, "Effect of a small loss or gain in the periodic nonlinear Schrödinger anomalous wave dynamics", Physical Review E **101**, 032204 (2020).

[168] K. Tajima, "Compensation of soliton broadening in nonlinear optical fibers with loss", Optics Letters **12**, 54 (1987).

[169] V. Bogatyrev, M. Bubnov, E. Dianov, A. Kurkov, P. Mamyshev, A. Prokhorov, S. Rumyantsev, V. Semenov, S. Semenov, A. Sysoliatin, S. Chernikov, A. Gur'yanov, G. Devyatykh, and S. Miroshnichenko, "A single-mode fiber with chromatic dispersion varying along the length", Journal of Lightwave Technology **9**, 561–566 (1991).

[170] P. Mamyshev, S. Chernikov, and E. Dianov, "Generation of fundamental soliton trains for high-bit-rate optical fiber communication lines", IEEE Journal of Quantum Electronics **27**, 2347–2355 (1991).

[171] S. V. Chernikov and P. V. Mamyshev, "Femtosecond soliton propagation in fibers with slowly decreasing dispersion", Journal of the Optical Society of America B **8**, 1633 (1991).

[172] A. Kudlinski, A. K. George, J. C. Knight, J. C. Travers, A. B. Rulkov, S. V. Popov, and J. R. Taylor, "Zero-dispersion wavelength decreasing photonic crystal fibers for ultraviolet-extended supercontinuum generation", Optics Express **14**, 5715 (2006).

[173] N. J. Smith, F. M. Knox, N. J. Doran, K. J. Blow, and I. Bennion, "Enhanced power solitons in optical fibres with periodic dispersion management", Electronics Letters **32**, 54–55 (1996).

[174] I. R. Gabitov and S. K. Turitsyn, "Averaged pulse dynamics in a cascaded transmission system with passive dispersion compensation", Optics Letters **21**, 327 (1996).

[175] F. Matera, A. Mecozzi, M. Romagnoli, and M. Settembre, "Sideband instability induced by periodic power variation in long-distance fiber links", Optics Letters **18**, 1499 (1993).

[176] N. J. Smith and N. J. Doran, "Modulational instabilities in fibers with periodic dispersion management", Optics Letters **21**, 570 (1996).

[177] K. Kikuchi, C. Lorattanasane, F. Futami, and S. Kaneko, "Observation of quasi-phase matched four-wave mixing assisted by periodic power variation in a long-distance optical amplifier chain", IEEE Photonics Technology Letters **7**, 1378–1380 (1995).

[178] S. G. Murdoch, M. D. Thomson, R. Leonhardt, and J. D. Harvey, "Quasi-phase-matched modulation instability in birefringent fibers", Optics Letters **22**, 682 (1997).

[179] S. G. Murdoch, R. Leonhardt, J. D. Harvey, and T. A. B. Kennedy, "Quasi-phase matching in an optical fiber with periodic birefringence", Journal of the Optical Society of America B **14**, 1816 (1997).

[180] M. Droques, A. Kudlinski, G. Bouwmans, G. Martinelli, and A. Mussot, "Dynamics of the modulation instability spectrum in optical fibers with oscillating dispersion", Physical Review A **87**, 013813 (2013).

[181] F. Copie, M. Conforti, A. Kudlinski, A. Mussot, and S. Trillo, "Competing Turing and Faraday instabilities in longitudinally modulated passive resonators", Physical Review Letters **116**, 143901 (2016).

[182] M. Marhic, F. Yang, M.-C. Ho, and L. Kazovsky, "High-nonlinearity fiber optical parametric amplifier with periodic dispersion compensation", Journal of Lightwave Technology **17**, 210–215 (1999).

[183] C. Finot, F. Feng, Y. Chembo, and S. Wabnitz, "Gain sideband splitting in dispersion oscillating fibers", Optical Fiber Technology **20**, 513–519 (2014).

[184] M. Conforti, A. Mussot, A. Kudlinski, S. Rota Nodari, G. Dujardin, S. De Biévre, A. Armaroli, and S. Trillo, "Heteroclinic structure of parametric resonance in the nonlinear Schrödinger equation", Physical Review Letters **117**, 013901 (2016).

[185] S. Wabnitz, "Modulational polarization instability of light in a nonlinear birefringent dispersive medium", Physical Review A **38**, 2018–2021 (1988).

[186] A. Parriaux, K. Hammani, and G. Millot, "Electro-optic frequency combs", Advances in Optics and Photonics **12**, 223 (2020).

[187] P. F. Byrd and M. D. Friedman, *Handbook of elliptic integrals for engineers and scientists* (Springer Berlin Heidelberg, Berlin, Heidelberg, 1971).

[188] M. Santagiustina, "Exact integral solution of saturation and depletion in forward and backward optical fiber Raman amplifiers", Optics Letters **32**, 3023 (2007).

[189] M. Maier, W. Kaiser, and J. A. Giordmaine, "Backward stimulated Raman scattering", Physical Review **177**, 580–599 (1969).

[190] V. V. Kozlov, S. V. Manakov, and S. Wabnitz, "Exact solution for the gigantic amplification of ultrashort pulses in counterpumped Raman amplifiers", Optics Letters **36**, 1632 (2011).

[191] C. Lin and R. H. Stolen, "New nanosecond continuum for excited-state spectroscopy", Applied Physics Letters **28**, 216–218 (1976).

Author's bibliography

Publications in peer-reviewed journals

- G. Vanderhaegen, P. Szriftgiser, C. Naveau, A. Kudlinski, M. Conforti, S. Trillo, N. Akhmediev, and A. Mussot, "Observation of doubly periodic solutions of the nonlinear Schrödinger equation in optical fibers", Optics Letters **45**, 3757–3760 (2020).

- G. Vanderhaegen, P. Szriftgiser, A. Kudlinski, M. Conforti, S. Trillo, M. Droques, and A. Mussot, "Observation of four Fermi-Pasta-Ulam-Tsingou recurrences in an ultra-low-loss optical fiber", Optics Express **28**, 17773–17781 (2020).

- G. Vanderhaegen, C. Naveau, P. Szriftgiser, A. Kudlinski, M. Conforti, A. Mussot, M. Onorato, S. Trillo, A. Chabchoub, and N. Akhmediev, ""Extraordinary" modulation instability in optics and hydrodynamics", Proceedings of the National Academy of Sciences **118** (2021).

- C. Naveau, G. Vanderhaegen, P. Szriftgiser, A. Kudlinski, M. Conforti, S. Trillo, N. Akhmediev, and A. Mussot, "Heterodyne optical time-domain reflectometer combined with active loss compensation: a practical tool for investigating Fermi Pasta Ulam recurrence process and breathers dynamics in optical fibers", Frontiers in Physics **9** (2021).

- G. Vanderhaegen, P. Szriftgiser, M. Conforti, A. Kudlinski, M. Droques, and A. Mussot, "Experimental investigation of short pulse Raman amplification with backward pumping", Optics Letters **46**, 5019–5022 (2021).

- G. Vanderhaegen, P. Szriftgiser, A. Kudlinski, M. Conforti, A. Armaroli, and A. Mussot, "Observation of the noise-driven thermalization of the Fermi-Pasta-Ulam-Tsingou recurrence in optical fibers," Physical Review A **106**, 033519 (2022).

- G. Vanderhaegen, P. Szriftgiser, A. Kudlinski, A. Armaroli, M. Conforti, A. Mussot, and S. Trillo, "Multiple symmetry breaking induced by weak damping in the Fermi-Pasta-Ulam-Tsingou recurrence process", arXiv:2206.00912 and submitted to Physical Review Letters (2022).

Posters in peer-reviewed national conferences

- **G. Vanderhaegen**, P. Szriftgiser, M. Conforti, A. Kudlinski, S. Trillo, and A. Mussot, "Observation de multiples brisures de symétrie des récurrences de Fermi-Pasta-Ulam-Tsingou : le rôle des pertes de la fibre optique", SFO Optique, Dijon, France (2021).

Posters in peer-reviewed international conferences

- **G. Vanderhaegen**, P. Szriftgiser, M. Conforti, A. Kudlinski, and A. Mussot, "Experimental investigation of the saturated regime of short pulse amplification in counter-pumped Raman amplifiers", CLEO/Europe-EQEC, Munich, Germany, Online (2021).

Orals in peer-reviewed international conferences

- **G. Vanderhaegen**, P. Szriftgiser, A. Kudlinski, M. Conforti, S. Trillo, and A. Mussot, "First experimental observation of four Fermi-Pasta-Ulam-Tsingou recurrences in an optical fiber", CLEO US, San Jose, United States, Online (2020).
- **G. Vanderhaegen**, P. Szriftgiser, A. Kudlinski, M. Conforti, S. Trillo, and A. Mussot, "Observation of the Fermi Pasta Ulam recurrence multiple symmetry breakings triggered by optical fiber losses", CLEO US, San Jose, United States, Online (2021).
- **G. Vanderhaegen**, P. Szriftgiser, M. Conforti, A. Kudlinski, S. Trillo, and A. Mussot, "Loss induced multiple symmetry breakings in the Fermi Pasta Ulam recurrence process", CLEO/Europe-EQEC, Munich, Germany, Online (2021).
- **G. Vanderhaegen**, P. Szriftgiser, M. Conforti, A. Kudlinski, Andrea Armaroli, and A. Mussot, "Experimental investigation of spontaneous and seeded modulation instability competition: route to the thermalization of the Fermi Pasta Ulam Tsingou recurrences", SPIE Photonics West LASE, San Francisco, United States (2022).

Invited orals in peer-reviewed international conferences

- **S. Trillo**, G. Vanderhaegen, C. Naveau, P. Szriftgiser, M. Conforti, A. Kudlinski, and A. Mussot, "Nonlinear stage of modulational instability: towards a global understanding", International Conference Laser Optics, St. Petersburg, Russia (2020).
- **A. Mussot**, M. Conforti, A. Kudlinski, C. Naveau, P. Szriftgiser, G. Vanderhaegen, and S. Trillo, "Fermi Pasta Ulam recurrences in optical fibers", OSA Conference on Nonlinear Optics, Hawaii, United Sates (2021). Not given due to COVID-19.

- **G. Vanderhaegen**, P. Szriftgiser, M. Conforti, A. Kudlinski, Andrea Armaroli, and A. Mussot, "Experimental investigation of the noise-driven thermalization of the Fermi-Pasta-Ulam-Tsingou recurrences process", Advanced Photonics Congress, Maastricht, Netherlands (2022).

Intensity and phase measurements along optical fibers to reveal the complex nonlinear dynamic of Fermi-Pasta-Ulam-Tsingou recurrences

Abstract

This thesis work deals with experimental investigations of the Fermi-Pasta-Ulam-Tsingou (FPUT) recurrences in optical fibers, which are induced by the nonlinear regime of modulation instability (MI). MI is one of the most universal phenomenon in nonlinear physics where a weak perturbation of a strong plane wave is exponentially amplified during its propagation in a nonlinear and dispersive medium. In case of a periodic modulation of the plane wave, a complex but coherent dynamics between the initial and the newly generated waves takes place. It reaches the saturation, then follows a decay stage and finally returns to its initial state. In this thesis, we were able to deeply characterize this dynamics by distributed measurements in amplitude and phase of the main spectral components thanks to a multi-heterodyne time domain reflectometry setup. By actively compensating for the fiber attenuation, we first managed to mimic an integrable system and to observe FPUT dynamics over long distances. It both allowed to confirm theoretical predictions of the NLSE and record up to 5 consecutive recurrences, as a seminal result for the following studies. Then, we investigated modulation instability and FPUT in non-integrable systems: from the noise instability as a detrimental effect leading to the recurrences break-up and an irreversibly thermalized system, from a weak damping or forcing contribution leading to separatrix crossings and multiple symmetry breakings of the process, and from the fiber shaping with an oscillating dispersion profile leading to MI even in the normal regime.

Keywords: nonlinear fiber optics, modulation instability, fermi-pasta-ulam-tsingou recurrences, breathers, nonlinear schrödinger equation

---

Mesures en intensité et en phase le long de fibres optiques pour révéler la dynamique non linéaire complexe des récurrences de Fermi-Pasta-Ulam-Tsingou

Résumé

Ces travaux de thèse portent sur des études expérimentales des récurrences de Fermi-Pasta-Ulam-Tsingou (FPUT) dans des fibres optiques, qui apparaissent en régime non linéaire de l'instabilité modulationnelle (IM). L'IM est l'un des phénomènes les plus universels en physique non linéaire dans lequel une faible perturbation d'une onde plane intense est amplifiée exponentiellement lors de sa propagation dans un milieu non linéaire et dispersif. Dans le cas d'une modulation périodique de l'onde plane, une dynamique complexe mais cohérente s'opère entre les ondes initialement excitées et celles nouvellement générées. Elle atteint ensuite la saturation, puis suit un cycle de décroissance et revient finalement à son état initial. Dans cette thèse, nous avons pu caractériser cette dynamique en profondeur par des mesures distribuées en amplitude et en phase des principales composantes spectrales grâce à un montage de détections hétérodynes couplé à un réflectomètre temporel. En compensant activement l'atténuation de la fibre, nous avons d'abord réussi à simuler un système intégrable et à observer la dynamique des récurrences de FPUT sur de longues distances. Cela nous a permis d'une part de confirmer des prédictions théoriques de l'équation de Schrödinger non linéaire et d'autre part d'enregistrer jusqu'à 5 récurrences d'affilée, comme résultat préliminaire aux études suivantes. Ensuite, nous avons examiné l'IM et les récurrences de FPUT dans des systèmes non intégrables : par l'instabilité du bruit en tant qu'effet nuisible conduisant à la brisure des récurrences et à un système irréversiblement thermalisé, par une faible atténuation ou amplification entrainant des passages de séparatrice et de multiples brisures de symétrie du processus, et par la mise en forme oscillante du profil de dispersion de la fibre amenant à de l'IM même en régime normal.

Mots clés : optique non linéaire fibrée, instabilité modulationelle, récurrences de fermi-pasta-ulam-tsingou, ondes de respiration, équation de schrödinger non linéaire

---

Laboratoire de Physique des Lasers, Atomes et Molécules (PhLAM)
Bâtiment P5 – Campus Cité Scientifique – 2 Avenue Jean Perrin – 59655 Villeneuve d'Ascq Cedex – France